Preliminary Design, Testing and Analysis of a Planar Gliding Discharge Reactor for Gas Conversion at Ambient Conditions

Omar Mostafa

Department of Mechanical Engineering

McGill University
Montreal

A thesis submitted to McGill University
in partial fulfilment of the requirements of the degree of

Master of Science

October 2024

I would like to dedicate this thesis to my parents who made me the person who I am today. I hope I can one day repay their debt and make them proud.

Declaration

I declare that the contents of this thesis are original, except where specific reference is made to the work of others. It has not been submitted in whole, or in part, for consideration for any other degree or qualification at this, or any other university. This dissertation is my own work, and contains nothing which is the outcome of work done in collaboration with others, except as specified in the text and Acknowledgements.

Omar Mostafa
Montreal
October 2024

Abstract

Climate change and global warming caused by the buildup of carbon dioxide and other greenhouse gases are becoming increasingly problematic global issues. Therefore, there is a pressing need to find alternative low-emission energy sources. There have been many breakthroughs in renewable energy production through solar and wind power in the effort to electrify society. However, some critical heavy industrial processes, like steel production, cannot be easily electrified. These processes will still require chemical fuels to reach extreme temperatures and pressures. This creates a need to develop zero-carbon or carbon-neutral fuels for these processes.

Zero-carbon or carbon neutral fuels include green hydrogen, green ammonia, hydrocarbons obtained through the conversion of carbon dioxide. These fuels need to be created through gas conversion processes that have low in carbon emissions and that are economically feasible, and energy efficient. Plasma gas conversion is one method gaining traction in this field. This research aims to study the use of non-thermal plasmas for gas conversion applications at near ambient temperature and pressure. The near-ambient conditions would eliminate the need for costly materials and resources.

This study explores the use of a planar gliding discharge reactor, which is not a well-studied method of producing NTPs. Therefore, this work will provide vital preliminary analysis of the workings of a planar gliding discharge reactor through the analysis of electrical data, thermal data, and CFD simulations. In this study, a modification to the typical electrode design of a planar gliding discharge reactor will be implemented to help increase its efficiency. Ultimately, this study paves the way

for future work to further study and refine the reactor and its process in the effort to aid the electrification of our society.

Abrégé

Le changement climatique et le réchauffement de la planète causés par l'accumulation de dioxyde de carbone et d'autres gaz à effet de serre deviennent de plus en plus problématiques au niveau mondial. Il est donc urgent de trouver des sources d'énergie alternatives à faibles émissions. De nombreuses percées ont été réalisées dans la production d'énergie renouvelable grâce à l'énergie solaire et éolienne, dans le but d'électrifier la société. Cependant, certains processus industriels lourds critiques, comme la production d'acier, ne peuvent pas être facilement électrifiés. Ces processus nécessiteront toujours des combustibles chimiques pour atteindre des températures et des pressions extrêmes. Il est donc nécessaire de développer des combustibles sans carbone ou neutres en carbone pour ces processus.

Les carburants sans carbone ou neutres en carbone comprennent l'hydrogène vert, l'ammoniac vert et les hydrocarbures obtenus par conversion du dioxyde de carbone. Ces combustibles doivent être créés par des procédés de conversion des gaz à faibles émissions de carbone, économiquement viables et efficaces sur le plan énergétique. La conversion des gaz par plasma est une méthode qui gagne du terrain dans ce domaine. Cette recherche vise à étudier l'utilisation de plasmas non thermiques (PNT) pour des applications de conversion de gaz à une température et une pression proches de celles de l'air ambiant. Les conditions quasi ambiantes élimineraient le besoin de matériaux et de ressources coûteux.

Cette étude explore l'utilisation d'un réacteur à décharge planaire, qui n'est pas une méthode de production de PNT bien étudiée. Par conséquent, ce travail fournira une analyse préliminaire essentielle du fonctionnement d'un réacteur à décharge planaire par le biais de l'analyse des données électriques, des données

thermiques et des simulations de Dynamique des Fluides Numérique (DFN). Dans cette étude, une modification de la conception typique des électrodes d'un réacteur à décharge planaire sera mise en œuvre afin d'en augmenter l'efficacité. Enfin, cette étude ouvre la voie à de futurs travaux visant à étudier et à affiner le réacteur et son processus dans le but de contribuer à l'électrification de notre société.

Acknowledgements

I would like to begin by thanking all my supervisors, past and present. To Professor Melanie Tetreault-Friend, thank you for taking a chance on me and introducing me to the world of research—I wouldn't be here without you. To Professor Jeffrey Bergthorson, thank you for taking me in and being there when I needed you. Finally, to Professor Sylvain Coulombe, I am eternally grateful for your guidance. Your work ethic, enthusiasm, and excitement in and out of the lab are truly admirable. I have certainly faced many obstacles along the way, but I was fortunate to have all of you there to support me.

Alongside me on this journey were my lab mates across different labs. I always felt supported and at home. A special thanks goes to Steven Walker—without you, I truly would not be writing this today. It was a pleasure having you as my lab buddy, working with you, and talking with you to de-stress between runs.

To my friends, you must be relieved this is finally done! No more listening to me ranting about it. Nonetheless, I thank you for all your support and the long nights working together. To Aziz, thank you for always being there when I needed a friend, whether to ride a Bixi by the Lachine Canal or just sit and watch Netflix. To Rinith, you were with me during my undergrad, and you were with me throughout graduate school; what more could a friend ask for! To all my other friends across Canada and around the world, our group chats and video calls kept me sane throughout this journey.

Finally, to my parents, siblings, and my partner—even though you were not here with me physically, I drew immense emotional strength from all of you. I was motivated by you and shaped by you. To my parents, Mostafa Elfar and Mona Akl,

words cannot begin to capture the love and appreciation I have for both of you. I surely would not be where I am today without you.

Contents

List of Figures

List of Tables

Nomenclature

Abbreviations

TP Thermal Plasma

NTP Non-Thermal Plasma

IPC In-Plasma Catalysis Process

PPC Post-Plasma Catalysis

DBD Dielectric Barrier Discharge

MW Microwave

GA Gliding Arc

GHGs Green House Gases

APGD Atmospheric Pressure Glow Discharge

AC Alternating Current

DC Direct Current

ppm Parts Per Million

RF Radio Frequency

GD Gliding Discharge

PGD Planar Gliding Discharge

TMs Transition Metals

BNNTs Boron Nitride Nanotubes

CNTs Carbon Nanotubes

CFD Computational Fluid Dynamics

CAD Computer Aided Design

IR Infrared

P&ID Piping and Instrumentation Diagram

PTFE Polytetrafluoroethylene

SLPM Standard Liter Per Minute

MFC Mass Flow Controller

UV Ultraviolet

FFT Fast Fourier Transform

Symbols

V_b	Breakdown Voltage	V
A	First Ionization Coefficient	$\mathrm{cm^{-1}\,Torr^{-1}}$
B	Second Ionization Coefficient	$\mathrm{V\,cm^{-1}\,Torr^{-1}}$
d	Electrode Spacing	m
P	Pressure	Pa
γ	Secondary Electron Emission Coefficient	–
E	Electric Field	V/m
eV	Electron Volt	$1\,60218 \times 10^{-19}\,\mathrm{J}$
k_b	Boltzmann Constant	$1\,381 \times 10^{-23}\,\mathrm{J/K}$
T	Temperature	K
T_e	Electron Temperature	K

T_g	Bulk Gas Temperature	K
T_i	Ion Temperature	K
T_n	Neutral Particle Temperature	K
atm	Atmospheric Pressure	101 325 kPa
E/N	Reduced Electric Field	$10^{-21}\,\mathrm{V}\cdot\mathrm{m}^2$
$\dot{Q}_{out}$	Heat Rate Out	W
P_{in}	Power In	W
L	Characteristic Length	m
ρ	Density	$\mathrm{kg/m}^3$
t	Time	s
$\vec{v}$	Velocity	m/s
∇	Gradient Operator	–
g	Acceleration due to Gravity	$\mathrm{m/s}^2$
μ	Viscosity	$\mathrm{N/s\,m}^2$
ΔU	Change in Internal Energy	J
Q	Heat In	J
W	Work Done	J
h	Enthalpy	J
ϕ	Source Term	–
k	Thermal Conductivity	$\mathrm{W/m}\cdot\mathrm{K}$
Re	Reynolds Number	–
v	Flow Velocity	m/s
L	Characteristic Length	m

μ	Dynamic Viscosity	$\mathrm{N \cdot s/m^2}$
I	Radiative Intensity	$\mathrm{W/m^2 \cdot sr}$
λ	Wavelength	m
c	Speed of Light	m/s
n	Refractive Index	–
h	Planck's Constant	$\mathrm{J \cdot s}$
V_{in}	Inlet Velocity	m/s
Q	Flow Rate	$\mathrm{m^3/s}$
v	Velocity	m/s
A	Cross-Sectional Area	$\mathrm{m^2}$
α	Absorptivity	–
Ra	Rayleigh Number	–
β	Coefficient of Thermal Expansion	$\mathrm{K^{-1}}$
T_∞	Ambient Temperature	K
T_s	Surface Temperature	K
L	Characteristic Length	m
ν	Kinematic Viscosity	$\mathrm{m^2/s}$
α	Thermal Diffusivity	$\mathrm{m^2/s}$
Pr	Prandtl Number	–
Nu	Nusselt Number	–

Chapter 1

Introduction

1.1 Background & Motivation

The rising average global temperature, usually referred to as global warming, is driven by the buildup of greenhouse gases in the atmosphere. These greenhouse gases encompass a wide range of gases that trap heat radiated by the earth by absorbing it and heating up the atmosphere. One of the most significant of those gases is carbon dioxide, or CO_2. Therefore, to combat global warming, the increased CO_2 emissions from human activities need to be reduced. These activities include, energy generation, cement production, and other heavy industrial processes. As CO_2 keeps accumulating in the atmosphere, a more long-term and extreme change in the earth's climate is underway. This phenomenon, usually referred to as climate change, includes a wide range of extreme weather conditions and natural disasters, from hurricanes to droughts. These weather conditions and natural disasters have already been on the rise recently and should only be expected to increase in frequency and magnitude af-

fecting an increasing percentage of the population and leading to potentially billions of dollars in damages worldwide.

For a long time, the research has focused on finding alternative means of producing energy or electricity with advances made in solar panels, wind turbines, and hydroelectric power. However, energy production is one variable in the equation. Many industrial processes, such as those to produce steel, cement, and fertilizers, release tons of CO_2 into the atmosphere annually. This is where electrification comes into play. Some industrial processes that produce large amounts of greenhouse gases could be modified to use electricity, which, if obtained from green renewable sources, would cut down on their emissions. However, not all industrial processes are compatible with electricity, for example, due to high temperature and pressure requirements. Therefore, more innovative solutions and methods need to be used for their electrification. One such solution is to replace the fossil fuels used in these processes with zero-carbon or carbon-neutral fuels. These fuels have a net zero carbon cycle, where no extra carbon is added to the atmosphere from burning them.

A multitude of methods of producing zero-carbon and carbon-neutral fuels have been or are actively being studied, but no major breakthroughs have been made. However, one method has been gaining significant attention lately from many research teams worldwide, that is gas conversion using plasma. Practically, plasma allows for the direct conversion of electrical energy into thermal and/or chemical energy. Allowing for green electricity to be used to produce zero-carbon or carbon-neutral fuels.

Plasma processing media can be differentiated based on bulk gas temperature and electron temperature: equilibrium plasmas, or thermal plasmas, and non-equilibrium

plasmas, or non-thermal plasmas. The first occurs when constituents are in thermal equilibrium, while the second arises when electrons are generally much hotter than the heavier species. In some situations and applications a non-thermal plasma can be better suited for gas conversion due to its minimal impact on the bulk gas temperature (i.e., more chemistry, less heating). This allows for the efficient operation of thermodynamically unfavorable and energy-intensive reactions. Moreover, it can facilitate chemical reactions under near ambient conditions, reducing the complexity and cost of the equipment and allowing for the decentralization of the production of fuels.

There are a number of ways or configurations to produce a non-thermal plasma in a controlled volume or in a reactor. However, one of those different methods or reactor configurations stands out from the rest: gliding discharge reactors. On paper, gliding discharge plasmas offer a theoretically higher gas conversion efficiency at ambient temperature and atmospheric pressure. However, due to a number of issues, this configuration is understudied, with very little work done on understanding the discharge, its characterization, or the optimization of the design. Thus, a study where a gliding discharge reactor is designed, optimized, studied, and characterized is needed. Ultimately, this study will enhance over the understanding of the operation of a gliding discharge reactor. This would allow for future studies to build upon and use the knowledge to design better and more efficient plasma reactors paving the way to a more efficient production of zero-carbon and carbon-neutral fuels. These fuels are vital for the electrification efforts of heavy industrial processes.

1.2 Thesis Objectives

This study aims to address a gap in the design, optimization, and characterization of planar gliding discharge reactors for gas conversion applications, specifically the production of zero-carbon and carbon-neutral fuels using electricity. Gliding discharges were chosen because they possess characteristics that make them more advantageous for gas conversion applications than other means or configurations of plasma reactors. This is due to them combining aspects of both equilibrium and non-equilibrium plasmas. A planar configuration of a gliding discharge reactor is an excellent place to start due to its simplicity and it's potential in allowing the use of the reactor walls to introduce a catalyst layer into the reactor. The main purpose of this study is to characterize the discharge as opposed to studying efficiency and conversion rates directly. Thus, an easily accessible, safe, and non-reactive gas like nitrogen would be ideal for the working gas. Eventually, more reactive gases and catalysts could be used in the reactor to study conversion rates and energy efficiencies. However, these are beyond the scope of this thesis. This thesis aims to address the following objectives: design, optimize, and characterize an atmospheric pressure planar gliding discharge reactor that can be used to study plasmas in gas conversion applications related to the electrification of industrial processes. The following additional conditions need to be satisfied:

1. Design an easily assembled and disassembled reactor.
2. Generate stable and repetitive discharges.
3. Design a reactor that allows for easy introduction of a catalyst layer.

1.3 Thesis Organization

This thesis is structured as follows: In Chapter 2, a comprehensive literature review of plasma for gas conversion, the use of boron nitride nanotubes as catalyst carriers, as well as the workings of computational fluid dynamics and thermal imaging, is presented. In Chapter 3, the processes of reactor design, optimization, and setup are presented. Chapter 4 presents and discusses the electrical data used for the preliminary characterization of the discharge. Chapter 5 presents and discusses the computational fluid dynamics and thermal data obtained. Finally, Chapter 6 makes some concluding remarks on the content of this thesis as well as suggestions for future work.

Chapter 2

Literature Review

2.1 Plasma for Gas Conversion

2.1.1 Introduction to Plasma

Plasma is considered the fourth state of matter and consists of an ionized gas. This state exists in nature, constituting 99% of all visible matter in the universe. Plasma is an extraordinary state of matter governed by complex physics, chemistry, and electrical phenomena. On Earth, man-made plasma can be generated for various applications, from industrial to biomedical purposes. These plasmas are created by applying high voltage difference across electrodes with a gas in between, creating a strong electric field. This field ionizes gas atoms by stripping electrons from them and accelerating these electrons to high speeds, increasing their kinetic energy. Subsequent collisions between these electrons and other gas particles excite, ionize, or dissociate them, resulting in a mixture of neutral particles, excited species, positively charged ions, and negatively charged electrons. Notably, the number of positive and negative

particles remains equal, rendering the plasma electrically neutral, commonly referred to as "quasi-neutral" [1].

The minimum electrical potential required to achieve ionization is known as the breakdown voltage V_b, which depends on the applied electric field, gas composition, and pressure. The breakdown voltage V_b can be calculated using the Townsend Breakdown equation [2], shown in Equation 2.1.

$$V_b = \frac{Bpd}{\ln\left(\frac{Apd}{\ln\left(1+\frac{1}{\gamma}\right)}\right)} \tag{2.1}$$

Here, p, d, and γ represent pressure in pascals, distance between electrodes in meters, and the secondary electron emission coefficient for the electrodes, respectively. Constants A and B are determined experimentally and are constants over a given range of E/p for a specific gas [2].

The variation of V_b with distance, gas composition, and pressure can be visualized using Paschen curves, as illustrated in Figure 2.1.

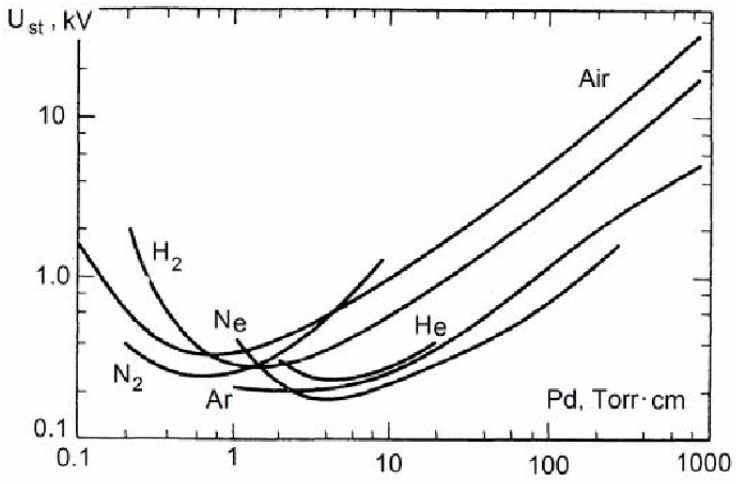

Figure. 2.1: Paschen Curve depicting V_b for different pd values in various gases, including air and nitrogen [3].

Plasma can be generated over a wide range of conditions including gas temperatures, pressures, electron temperatures, and electron densities. Generally, plasmas are classified into thermal (equilibrium) and non-thermal (non-equilibrium) types. Thermal plasmas (TPs) achieve local thermal equilibrium with high temperature and pressure, typically ranging from 10,000 to 50,000 K (1 to 5 eV) [4]. These plasmas convert electrical energy into heat energy, suitable for applications such as plasma cutting. They are characterized by high electron densities, necessitating significant currents that are required for thermalization into an arc.

Non-thermal plasmas (NTPs), on the other hand, maintain a significantly higher electron temperature T_e compared to ion temperature T_i and neutral particle temperature T_n, thus lacking local thermal equilibrium. This condition is typically achieved at low pressures where minimal energy input prevents thermalization. However, NTPs can be generated at atmospheric pressures and have become more common recently.

Figure 2.2 illustrates the relationship between T_e and gas temperature T_g as a function of pressure, highlighting the regions of thermal and non-thermal plasma.

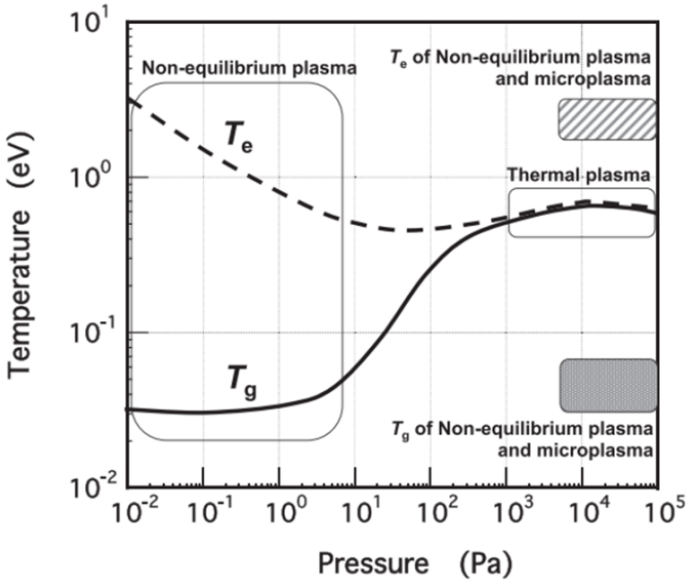

Figure. 2.2: Variation of T_e and T_g with pressure, distinguishing thermal and non-thermal plasma regions [5].

Warm plasmas, occupying intermediate regions between TPs and NTPs, combining properties from both such as a high electron density from TPs and low gas temperature from NTPs, offering versatility in its applications.

2.1.2 Plasma Facilitated Chemical Reactions

One of the properties of plasma that makes it attractive for gas conversion applications and chemical reactions is its high electron temperature T_e, a characteristic shared by all types of plasma. At these temperatures, electrons facilitate chemical reactions through bond dissociation, radical formation, ionization, and many other pathways. These pathways lead to the formation of reactive species, ions, additional electrons,

radicals, and metastable species within the plasma [1]. While most of these reactions could be achieved using thermal catalytic pathways, plasma catalysis may accelerate reactions approximately two to three times [2].

While applicable to most types of plasma, not all are well-suited for chemical reactions. Apart from the high energy requirements for generating TPs, they also necessitate rapid cooling or quenching of products. This step halts the decrease in conversion ratio due to recombination mechanisms and effectively freezes reactions [6]. Conversely, NTPs operate at lower gas temperatures and are better suited for thermodynamically unfavorable chemical reactions. They operate nearly at ambient temperatures while remaining chemically reactive, enabling even endothermic reactions or those with high reactant dissociation energies to proceed [2]. This selectivity makes NTPs more suitable for gas conversion applications. However, NTPs are typically produced in low-pressure environments, which reduces yield and increases equipment costs. Some of the challenges associated with both TPs and NTPs for chemical reactions can be mitigated by using warm plasmas. These plasmas can operate at ambient or atmospheric pressure while maintaining a lower bulk gas temperature, offering enhanced chemical selectivity compared with TPs and NTPs.

While cool and warm plasmas exhibit greater selectivity than hot plasmas, their effectiveness can be further enhanced by incorporating a catalyst. This catalyst leverages the abundance of reactive species and radicals generated by the plasma to direct reactions towards desired products. This process, known as plasma catalysis, has shown significant increases in conversion rates and efficiencies when a catalyst is introduced [7].

When combining a catalyst with a plasma source in plasma catalysis, two configurations are commonly utilized. Figure 2.3 depicts three possible plasma reactor setups. The first configuration is a simple plasma reactor without a physical catalyst. Introducing a catalyst allows for two additional configurations: an in-plasma catalysis (IPC) configuration, where the plasma interacts directly with the catalyst and its surface, and a post-plasma catalysis (PPC) configuration, where long-lasting excited species by the plasma subsequently interact with the catalyst [1].

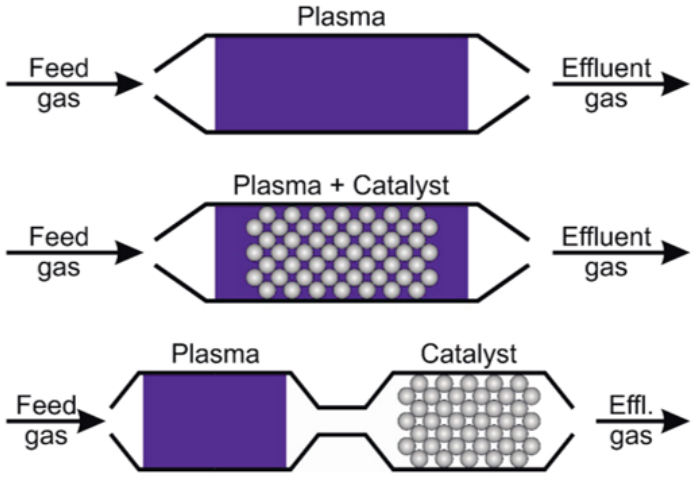

Figure. 2.3: Three possible configurations for plasma reactors, including the two configurations possible when combining plasma with a physical catalyst for plasma catalysis [1].

In an IPC configuration, the direct interaction between plasma and catalyst yields various synergistic effects beneficial for plasma catalysis, such as morphological changes in the catalyst, changes in oxidation states, altered reaction pathways, effects on catalytic poisoning, lowered activation barriers, enhanced adsorption of molecules by vibrationally excited species, collisions with inert gas particles or molecules, and photocatalysis activation through UV light emitted by the plasma [8], [9].

Unlike IPC configurations, PPC configurations exhibit fewer synergies due to the short lifespan of many reactive species and plasma intermediates, which limits their interaction with catalyst surfaces [7]. However, PPC facilitates scaling of the process in some cases because the plasma source and catalyst can be scaled up separately [7]. While IPC configurations are challenging to scale up as a single unit, scaling up the process through replication may be economically feasible [10].

2.1.3 Plasma Sources and Reactors for Plasma Catalysis

There are various methods used to produce non-thermal plasma (NTP) or warm plasma and configure plasma reactors. Table 2.1, adapted from [7], summarizes numerous NTP production methods and reactor setups.

Table 2.1: Different methods of producing NTP or warm plasma and various reactor configurations.

NTP Production Method	Reactor Setup
Dielectric Barrier Discharge (DBD)	Volume DBD: - Annular/packed bed - Plate to plate Surface DBD: - Annular with coil - Dielectric plate with mesh DBD hybrid setups: - Hybrid surface/packed bed - Corona setup
Corona Discharge	Cocurrent design: - Point to plane - Pin to plate - Needle to plate Crosscurrent designs: -Wire to plate - Multitoothed wheel
Gliding Arc	- Gliding arc - Rotating gliding arc - Reverse vortex gliding arc
Atmospheric pressure plasma jet	- AC driven - Pulsed DC driven - Microwave driven
Pulsed Microwave Discharge	- Waveguide-Based - Coaxial Cable - Resonant Cavity - Microstrip Line - Slotted Waveguide Array

Among the various configurations, gliding discharge reactors are particularly effective for generating warm plasma, combining NTP benefits of low bulk gas temperatures with the high pressure, current, and electron density characteristic of TPs.

Additionally, they exhibit better energy efficiency compared to DBD and corona plasma reactors, even when a catalyst is used in the latter configurations. Therefore, the addition of a catalyst to a gliding discharge reactor can further enhance its efficiency [11]–[13].

In this study, while no specific focus is placed on a single chemical reaction, significant attention is given to nitrogen fixation and carbon conversion reactions as part of efforts to electrify heavy industrial processes. Plasma reactors offer rapid start-up and shutdown capabilities, making them ideal for pairing with intermittent energy sources for converting N_2 and CO_2 into value-added products or chemical energy for storage. This capability aligns well with renewable energy sources such as solar or wind power, which are inherently intermittent. Thus, when surplus power is available, reactors can quickly convert electrical energy into useful chemical energy.

Nitrogen Fixation

In 2019, global ammonia production reached 235 million tonnes, making it the second most produced chemical after sulfur [14]. Ammonia is crucial for fertilizers, supporting approximately 50% of global food production [15]. The Haber-Bosch process, established over a century ago, dominates ammonia production:

$$N_2 + 3H_2 \longleftrightarrow 2NH_3 + 46.1\ kJ/mol^{-1} \tag{2.1}$$

This exothermic reaction releases around 46 kJ/mol-NH_3, making high pressure and low temperature ideal for equilibrium ammonia formation. However, at such conditions, the yield of ammonia is extremely low and not economically feasible.

Therefore, the gases need to be reacted at high temperatures and pressures. These conditions are still not ideal since they favour ammonia decomposition [16]. Optimal conditions are achieved at temperatures between 400 °C and 500 °C and pressures between 100 and 200 atm [15]. However, this process remains costly in terms of capital, operating expenses, and energy use. Approximately 20% of global ammonia synthesis energy is consumed by the Haber-Bosch process, with the remainder used for hydrogen production via steam methane reforming [14], [17]. Thus, greener ammonia production methods are essential, particularly given rising global demand due to the ever growing population and diverse potential applications for ammonia, as depicted in Figure 2.4.

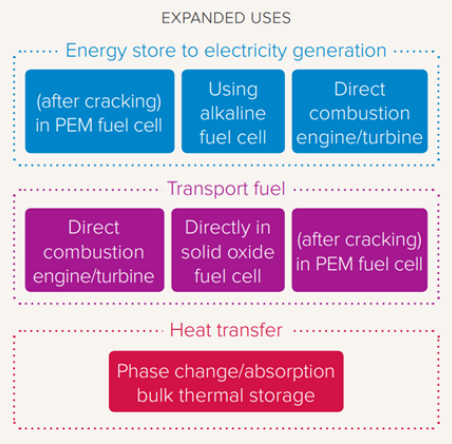

Figure. 2.4: Potential expanded uses of ammonia indicating increased future demand. Ammonia could serve as a fuel or heat transfer/storage medium [18].

Numerous ammonia synthesis methods have been studied, with plasma, particularly NTPs, showing promise due to its low theoretical energy requirement (Figure 2.5). Current NTP tests employ DBD discharge reactors with various metal and metal oxide catalysts. However, none have matched Haber-Bosch's 15% yield and

0.1 MJ/mol-NH_3 energy consumption, or 0.47 MJ/mol-NH_3 with intermittent energy sources. Currently, the best DBD reactors achieve only 9% yield at 1.5 MJ/mol-NH_3, far from the value expected with intermittent sources of around 0.47 MJ/mol-NH_3. This is due to an inefficiency in the mode by which a DBD reactor promotes the dissociation of N_2 and H_2 molecules onto a catalyst. Figure 2.6 highlights atmospheric pressure N_2 dissociation modes relative to reduced electric field (Td). Microwave and gliding discharges outperform DBD, with more efficient vibration-based N_2 dissociation [19].

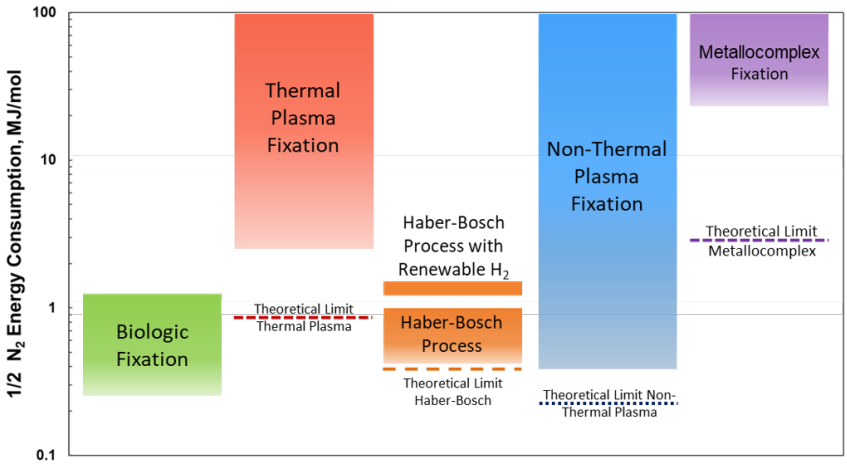

Figure. 2.5: Comparison of ammonia synthesis methods based on energy requirements. The theoretical limits depend on reaction pathways, energy sources and a range of other factors. Non-thermal plasmas (NTPs) exhibit the lowest theoretical energy requirement [20].

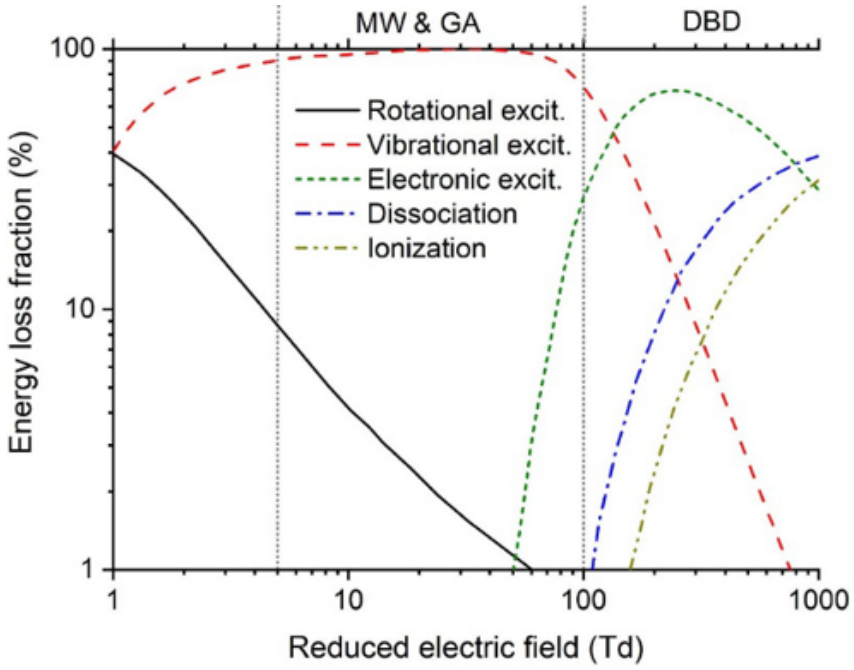

Figure. 2.6: Electron energy loss fraction in pure nitrogen gas versus reduced electric field (Td). Various NTP discharge types correspond to different reduced electric field ranges, with microwave and gliding discharges demonstrating more efficient molecular dissociation via vibration excitation [19].

Carbon Dioxide Conversion

Climate change, or the long-term change in average temperatures and weather patterns on Earth, is proving to be detrimental to human life with increasing droughts, floods, hurricanes, and wildfires. These natural disasters have been increasing in severity and frequency, with around 7,350 major disasters recorded worldwide between 2000 and 2019, marking a sharp increase compared to the twenty years prior. These disasters are estimated to have affected nearly 4 billion people, claiming the lives of over 1.2 million of them [21]. Climate change is caused by the increase in greenhouse gases (GHGs) dumped into the atmosphere by human activity. These gases are essential for Earth to remain habitable as they trap heat energy radiated

by the Earth. However, if the GHGs in the atmosphere exceed a certain limit, we get more warming than desired, or global warming, which is detrimental for life on Earth and is the driving force behind climate change.

Nowadays, many countries around the world are seeking ways to reduce their climate impact to ensure that the average global temperature does not increase by more than 2°C above industrial levels. One of the most significant culprits is CO_2, produced by our cars, planes, industrial processes, and fossil fuel burning for energy. To combat climate change, there are multiple routes that could be taken. One of these routes involves capturing atmospheric carbon or trapping carbon locally at the source. This captured or trapped carbon can then be treated not as waste, but as a carbon source that could be utilized for many different applications, including reduction into CO or hydrogenation into methane and other hydrocarbons. It is predicted that carbon conversion into value-added products will be crucial to electrification efforts [19].

However, CO_2 is an extremely chemically and thermodynamically stable molecule, requiring a significant amount of energy to break the C=O double bond [22]. Thus, any carbon conversion processes are extremely challenging. Several methods have been tested for carbon conversion applications, from photocatalytic and electrocatalytic processes to enzyme/biological conversion [22]. However, none have been viable due to high energy and capital demands. Herein lies the significance of non-thermal plasmas (NTPs), which allow us to chemically activate or dissociate CO_2 molecules at much lower temperatures than pure thermal pathways. With the addition of suitable catalysts, the reaction could be steered towards the desired products. The reduction reaction of CO_2 into CO using plasma catalysis has gained traction recently. Tests

with Dielectric Barrier Discharge (DBD) reactors showed a 40%-50% CO_2 conversion but with a relatively low energy efficiency of just 15%. On the other hand, tests with Microwave (MW) and Gliding Arc (GA) reactors showed a significant improvement in energy efficiency to around 50%-60%. However, this improvement came at the cost of yield, which dropped to around 20%. Therefore, breakthroughs in design, operating conditions, and catalyst choice need to be made before plasma catalysis becomes a viable option for CO_2 conversion [19].

As the test results discussed above show, MW and GA discharges are proving once again to be the more energy-efficient configurations for carbon conversion applications. This is because, similar to N_2 dissociation, CO_2 dissociation onto a catalyst surface is most efficient with vibrational excitation. Moreover, like N_2, the vibrational excitation mode of CO_2 dominates the reduced electric field operation range of MW and GA discharges, unlike the DBD region, which is dominated by ionization and electronic excitation. Figure 2.7 shows the different modes of CO_2 molecule dissociation onto a catalyst surface with the efficiency of electron energy transfer on the y-axis and the reduced electric field (Td) on the x-axis [19], [23].

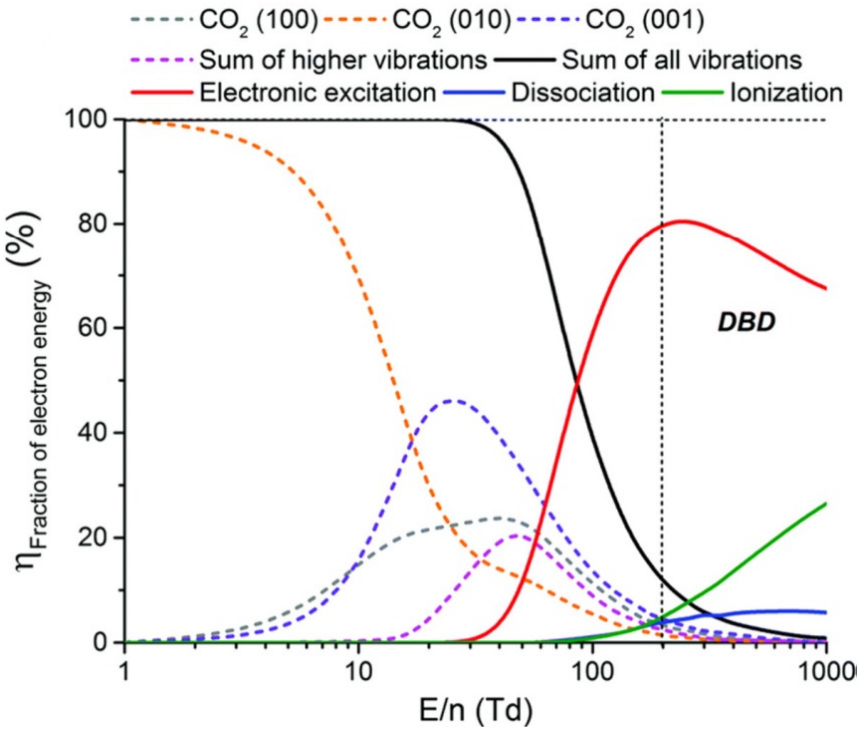

Figure. 2.7: Electron energy loss fraction in pure carbon dioxide gas versus reduced electric field (Td). Microwave and gliding discharges again demonstrate more efficient molecular dissociation via vibration excitation [23].

To better understand this difference in efficiency, we can examine the electron energies characteristic of DBDs versus those characteristic of MW and GAs. In DBDs, the activation and dissociation of CO_2 through ionization or electronic impact excitation are only possible with electrons having at least 7 eV of energy. However, this level of energy is significantly higher than the theoretically required energy to break the C=O bond (5.5 eV), resulting in wasted energy. On the other hand, MW and GAs have significantly lower electron energies in the range of $1-2$ eV. This allows them to facilitate dissociation through the more energy-efficient step-wise vibrational pathway with only 5.5 eV of energy expenditure. However, for MW discharges, a

reactor will need to be kept at very low pressures, increasing the complexity, cost, and overall energy consumption, leaving GA discharge reactors as the most promising avenue for further study and optimization [24].

For the remainder of this subsection, literature on nitrogen fixation and carbon conversion via plasma catalysis will be reviewed, summarized, and conclusions drawn. Studies encompass glow, dielectric barrier, gliding, radio frequency, and microwave discharges.

Glow Discharge

Glow discharge plasma is typically generated in a low-pressure environment ($1-10$ Torr) between two flat electrodes. A potential difference ranging from a few hundred volts to several thousand volts is applied across the inter-electrode gap to create an electric field in the chamber. This field accelerates a small number of randomly ionized gas particles (positively charged) toward the cathode and their electrons toward the anode. Due to the low pressure (low particle density), these charged particles have sufficient space (mean free path) to gain speed before colliding with other particles. Subsequently, these fast-moving particles ionize gas molecules. Excited atoms rapidly lose their energy by emitting photons of specific wavelengths, which gives rise to the characteristic "glow" of this discharge [25]. The exact operational mechanism of glow discharge will not be expanded on further here. However, Figure 2.8a depicts a typical image of a glow discharge, while Figure 2.8b presents a detailed diagram illustrating the different discharge regions [26].

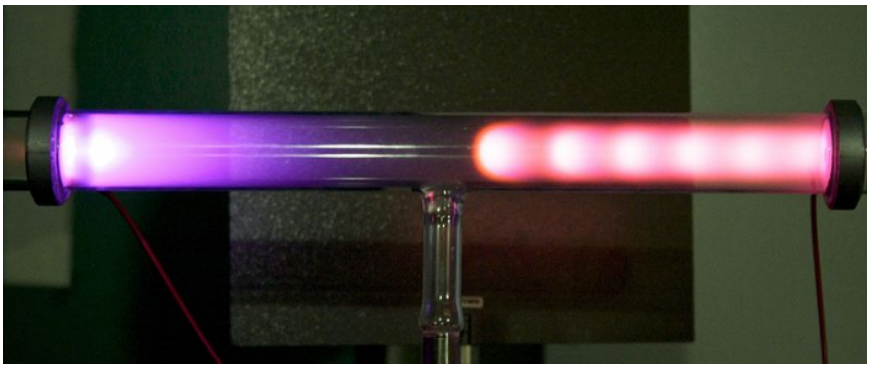

(a)

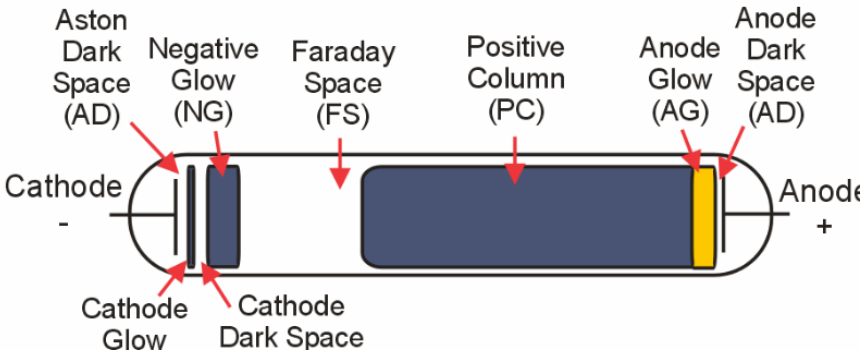

(b)

Figure. 2.8: (a) Typical image showing glow discharge generated in a low-pressure argon gas chamber [26]. (b) Diagram illustrating typical regions in glow discharge plasma [26].

Due to the typically required low operating pressure, glow discharges are not ideal for plasma catalysis due to high complexity, cost, and low yield. However, progress has been made in the development of Atmospheric Pressure Glow Discharges (APGD). Although the operating mechanism remains similar, a different configuration is necessary to generate a glow discharge at atmospheric pressure. In APGD, the flat cathode electrode is replaced with a sharp pin cathode. This modified electrode configuration concentrates the electric field, facilitating discharge formation with gas flowing axially around the pin. Figure 2.9 depicts an example of an APGD setup using hydrogen.

This new configuration shows promise for gas conversion as it retains NTP characteristics while operating at atmospheric pressure. The forthcoming literature review on glow discharge plasma catalysis will mainly focus on APGD [27].

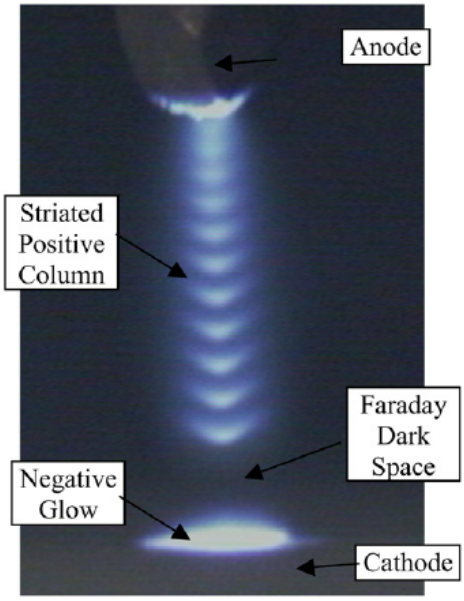

Figure. 2.9: Pin electrode configuration for generating glow discharge at atmospheric pressure using hydrogen gas. This setup exhibits similar characteristics and regions as previously described. [28]

As early as 1999, experiments employing APGD catalysis for CO_2 decomposition into CO and O_2 were conducted. Studies using various catalysts (Au, Rh, Pt, and Pd), an 8 kHz AC current, and a gas flow rate of 20 mL/min of 4% CO_2 in He achieved a maximum conversion of around 20% with a copper catalyst but with a modest efficiency of approximately 1.6%. Silver catalysts demonstrated the highest efficiency at around 9.3%, albeit with only a 7.3% conversion. Varying the CO_2 concentration in the feed gas marginally improved yield and efficiency. Currently, these figures do not demonstrate promising applications of APGD catalysis for CO_2

decomposition or reduction. However, potential future advancements may enhance the conversion and efficiency of this process [29].

APGDs have also been examined for CH_4 and CO_2 reforming into CO and H_2 (Reaction 2.2 below). The discharge was generated using an AC current and a sustained voltage of approximately 4500 V. This study reported a high conversion of around 83%, yet with a significantly low energy efficiency of only approximately 3%, again illustrating that APGDs are suboptimal for this application.

$$CH_4 + CO_2 \longleftrightarrow 2CO + 2H_2 \tag{2.2}$$

Several studies have explored glow discharge plasma catalysis for ammonia synthesis, although extensive recent research is lacking due to the prevalence of more promising NTP reactor configurations. Studies conducted using transition metals or their oxides as catalysts mostly reported modest ammonia yields of around 2% or 3% with very low energy efficiencies [30], [31]. One study using a silver catalyst achieved a yield of approximately 81%, though energy efficiency was not reported but presumed to be very low [32].

Dielectric Barrier Discharges

Dielectric barrier discharges (DBDs) represent one of the most extensively studied plasma discharge modes for applications such as ammonia synthesis and carbon dioxide conversion. This is primarily due to them operating at atmospheric pressure, facilitating industrial scalability [33]. DBDs can be generated in various reactor configurations, but their fundamental working principle remains consistent. We will

briefly examine the working principle and characteristics of the simplest configuration, known as planar DBDs (depicted in Figure 2.10). Like most plasma devices, a potential difference is applied across a pair of metal electrodes. However, in DBDs, these electrodes are separated by a resistive or insulating dielectric layer. This dielectric layer suppresses the discharge, preventing thermalization and arc formation, thereby maintaining a non-thermal plasma even at atmospheric pressure and low frequencies. The dielectric barrier helps maintain the NTP by preventing a continues conductive path between the electrodes and by accumulating charges that create an opposing electric field. However, as seen in Figures 2.6 and 2.7, DBDs are not the most efficient configuration for gas conversion due to their relatively high electron temperatures (T_e), which are sub-optimal for vibrational excitation. This limitation is reflected in the literature discussed below.

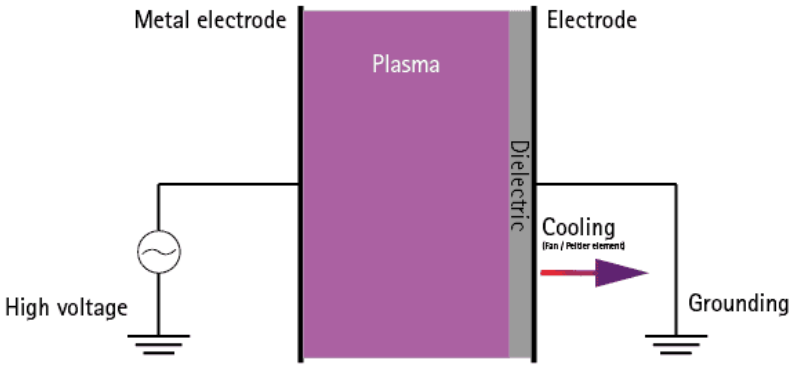

Figure. 2.10: Schematic diagram of a planar DBD plasma generating device powered by an AC current. The figure illustrates key components required for operating a DBD reactor [34].

In a study investigating a DBD reactor using a Mg/Al alloy oxide catalyst at a CO_2 flow rate of 0.044 L/min and a frequency of 9 kHz, a maximum CO_2 conversion into CO and O_2 of approximately 21% was reported [35]. However, the energy efficiency was only around 5.3% [35]. Another study achieved a slight improvement in conversion by diluting the inlet CO_2 flow with nitrogen, reporting a conversion of around 23% [36], but did not discuss energy efficiency. This omission is likely due to a similarly low figure as the previous study.

Paulussen *et al.* [37] examined the impact of flow rate, input power, and frequency on reducing pure CO_2 flow into CO and O_2. The highest conversion, approximately 30%, was observed at an input power of 200 W, a frequency of 60 kHz, and a flow rate of 0.05 L/min. This rate represents an improvement over similar studies reporting a maximum conversion in the low twenties or teens. The study also highlighted a significant dependency of conversion on inlet gas flow rate, with an increase from 0.05 L/min to 0.5 L/min decreasing the conversion from 30% to 3.56%. Notably, the study did not address energy efficiency, a critical issue for DBD reactors due to their mode of CO_2 dissociation.

For ammonia synthesis through nitrogen fixation, a study using an AC-powered DBD reactor at 3 kHz with hydrogen and nitrogen gases at flow rates ranging from 0.04 to 0.1 L/min investigated various N_2:H_2 ratios of 3:1, 1:1, and 1:3. At a 1:1 ratio and 0.08 L/min flow rate, the NH_3 concentration at the outlet was significantly lower with plasma alone (1800 ppm) compared to plasma with a $Co/MgAl_2O_4$ catalyst (7000 ppm), demonstrating the selectivity enhancement of plasma catalysis. However, unlike carbon conversion, ammonia conversion significantly improved with increasing flow rate up to 0.1 L/min. Energy efficiency was not discussed in the paper but was

provided in supplementary materials, with the maximum measured efficiency being approximately 1.19 g-NH_3/kWh. This figure is notably low compared to the 500 g-NH_3/kWh or 150−200 g-NH_3/kWh for the traditional Haber-Bosch and small-scale Haber-Bosch processes, respectively [38].

Across numerous studies investigating DBD plasma catalysis for ammonia synthesis, low energy efficiency remains a consistent trend. Mindong *et al.* [39] noted a 75% improvement in ammonia concentration using a catalyst compared to plasma alone, with a marginal energy efficiency increase to approximately 1.83 g-NH_3/kWh. Another study found that a porous catalyst support enhanced adsorption and energy efficiency to around 2.41 g-NH_3/kWh. However, the highest reported energy efficiency was achieved by Kim *et al.* [40], reporting an impressive 35.5 g-NH_3/kWh using pulsed plasma with a Ru-Mg/Al_2O_3 catalyst, albeit with a conversion of only around 2.55%.

As of the current literature, the best energy yields achieved are still over an order of magnitude lower than those of the traditional Haber-Bosch process, highlighting DBDs' current limitations for industrial electrification and the synthesis of zero-carbon and carbon-neutral fuels through gas conversion.

Radio Frequency or Microwave Discharges

The physics of radio frequency (RF) and microwave (MW) discharges can become complex and are not essential for this thesis. Therefore, only a brief description of their generation mechanisms and operating conditions will be provided. Interested readers are encouraged to explore further research.

RF and MW discharge plasma are generated using electromagnetic (EM) radiation in the RF and MW ranges, respectively. RF discharges commonly operate at 13.56 MHz, while MW discharges operate at 2.450 GHz. These frequencies are allocated worldwide for scientific, industrial, and medical applications. RF and MW discharges can be configured in various setups and generated under a range of pressures, from very low to atmospheric pressure. What distinguishes them from other plasma generation methods is their high-frequency driving signal. Unlike other plasma sources from the previous sections, which use AC signals typically at much lower frequencies (Hz or kHz), RF and MW discharges exploit the time-dependent nature of plasma development to restrict discharge formation, preventing electrons and charged particles from reacting fully to the applied field.

As seen in Figures 2.6 and 2.7, MW discharges exhibit reduced electric field values ideal for dissociating N_2 and CO_2 molecules through vibrational excitation, making them highly attractive for researchers studying nitrogen fixation and carbon conversion via plasma catalysis. For example, one study investigating MW discharges for CO_2 conversion reported a promising energy efficiency of approximately 90%, despite achieving only a 10% CO_2 conversion [41]. In contrast, another study achieved an 80% conversion but with a lower energy efficiency of about 6% [42]. This suggests a trade-off between efficiency and conversion, highlighting the need for balance in optimizing these systems. In a different study, such a balance was achieved with a 43% conversion and an efficiency of about 18%. Notably, most studies investigating MW discharges for carbon dioxide conversion used very low pressures around 1 Torr, which is sub-optimal [43]. Thus, further research is necessary to enhance and mature this technology before it becomes viable [44].

Despite expectations for high energy efficiency in RF and MW discharge reactors for ammonia synthesis due to their affinity for dissociating N_2 and CO_2 molecules through efficient vibrational excitation, literature figures remain modest. For most studies discussed below, energy efficiency is quantified by grams of NH_3 produced per kWh, which can then be compared to the traditional Haber-Bosch process: 500 g-NH_3/kWh or 150−200 g-NH_3/kWh for traditional Haber-Bosch and small-scale decentralized production, respectively [38].

Matsumoto's group [45], [46] utilized RF and MW discharges with Fe and Mo catalysts for ammonia synthesis. This study yielded a maximum energy efficiency of less than 0.01 g-NH_3/kWh, with a conversion of only 11.25%. Another group later tested metal-impregnated alumina support as catalysts, achieving an even lower conversion of 0.11% and an energy yield of 0.008 g-NH_3/kWh [47], [48]. The highest reported energy yield of approximately 0.31 g-NH_3/kWh came from a study by Carreon *et al.* [30]. This value, however, still does not compete with the Haber-Bosch process or even decentralized production.

Despite the lower energy yields in RF and MW discharge reactors for ammonia synthesis, these experiments provide valuable insights into this type of discharge. Although, in theory, RF or MW discharges should be efficient due to their affinity for dissociating N_2 and CO_2 molecules through the more efficient vibrational mode, this does not translate to a higher energy yield in practice. This discrepancy could be attributed to various reasons, including the low-pressure environments usually required for these discharges. Glow discharges (GDs) remain a viable candidate as they can operate at atmospheric pressure while remaining in the reduced electric field range optimal for vibrational excitation.

Gliding Discharges

Like MW discharges and as evident by Figures 2.6 and 2.7, Gliding Discharges (GD) are very efficient at dissociating both nitrogen and carbon dioxide molecules via vibrational excitation at atmospheric pressure. This means that they have the potential to be utilized in gas conversion applications, providing an improvement in energy efficiency over the previously discussed discharges. Additionally, unlike MW discharges, they are usually operated at atmospheric pressure, thus allowing them to be constructed with a lower capital investment due to a reduction in the design complexity. Moreover, since no additional energy is required to maintain low pressures, GDs could overall have better energy efficiencies even compared with MW discharges.

GDs can be generated in a number of different configurations, from 2D planar GDs to 3D rotating GDs. However, the working principle behind the different configurations is the same. Therefore, the simplest of the different configurations, the planar gliding discharge (PGD), will be discussed here. This configuration, which can be seen in Figure 2.11, works by applying a sufficiently high voltage and current across a pair of diverging electrodes. An arc is then struck at the shortest distance between the two electrodes. The working gas, which is injected behind or below the arc ignition point, then pushes the arc, forcing it to glide along the electrodes, lengthening it as it does so. The discharge lengthens until it reaches a certain "critical length" at which the discharge dissipates, prompting a new arc to be struck at the ignition point and starting the cycle over again. It should be noted that the critical length and thus, the volume covered by the GD between ignition and termination is a function of both the power supplied and the heat dissipated. The heat dissipated itself is a function of many factors, including the length of the discharge and the flow

rate of the gas. In fact, the flow rate has a huge impact on the reaction kinetics and behavior of the discharge [49].

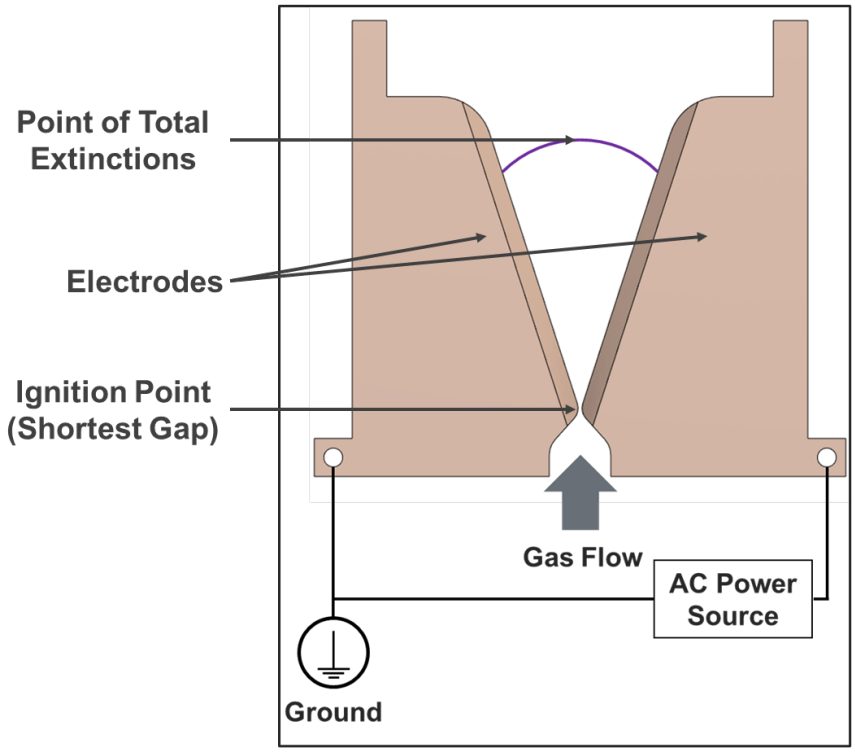

Figure. 2.11: A simplified schematic of a planar gliding discharge generation device operated by an AC current. The ignition point and extinction point are shown on the plot. The electrodes used are divergent to allow for the discharge to lengthen and cool as it glides.

PGDs can be operated using DC or AC currents. However, AC currents offer some advantages over DC currents in energy efficiency and equal electrode erosion. This is because, in a DC gliding discharge, a cathode hot-spot can form and hinder the gliding motion on the cathode, causing unequal wear between the two electrodes. Thus, AC currents might be a more optimal choice for gas conversion applications. Most of the tests summarized below use either an AC power supply or a pulsed power supply, with the latter usually showing improved energy efficiency [49].

Aside from their affinity for dissociating molecules through vibrational excitation, GDs are also able to combine properties of TPs and NTPs. Specifically, they can combine the large electron densities and high pressure of TPs with the more modest temperatures of NTPs. Thus, GDs are commonly referred to as "warm" plasma. This property is better demonstrated using Figure 2.12, seen below. At the start of the glide and in the region nearest to the ignition point, the discharge most closely resembles a thermal arc and behaves like a quasi-equilibrium plasma. As the arc lengthens, the heat dissipated from the arc ($\dot{Q}_{out}$) increases due to the increased surface area. This continues until the discharge reaches a length L, at which point the heat dissipated equals the power supplied to the plasma ($\dot{Q}_{out} = \mathrm{P}_{in}$). The discharge then transitions from a thermal arc into a cooler glow discharge mode sustaining a non-equilibrium plasma. This transition is likely due to the continuous increase in the electric field between the electrodes. This transition is brought about as the electrons continue to gain energy while the gas molecules in the plasma column are progressively cooled convectively as the discharge glides and lengthens. The discharge then continues as a non-equilibrium glow discharge until a length 3L, where the convective cooling is too large for the power source to support it, at which point it completely dissipates. This last region occurring between L and 3L is the most ideal for gas conversion, as was discussed before in the section delving into the advantages of non-equilibrium plasma. Therefore, maximizing this region would be advantageous for gas conversion applications. This could be achieved by adjusting flow rates and power parameters but could also be achieved by redesigning the reactor itself. However, after reviewing the literature, it was found that very little work is being done to optimize the design of GD reactors, especially PGD reactors. Additionally, the studies summarized

below were mainly concerned with studying the effect of different catalysts and power settings on the energy efficiency and conversion rate of PGD reactors in gas conversion applications. This is because, despite the simplicity of PGD designs and the ease of operating them, their non-stationary and non-uniform or non-repeatable nature makes them challenging for diagnostics and characterization [50]. Thus, gaps in the literature have been identified. There exists a need to optimize the design of PGD reactors while producing a more uniform and repeatable discharge for performing diagnostics.

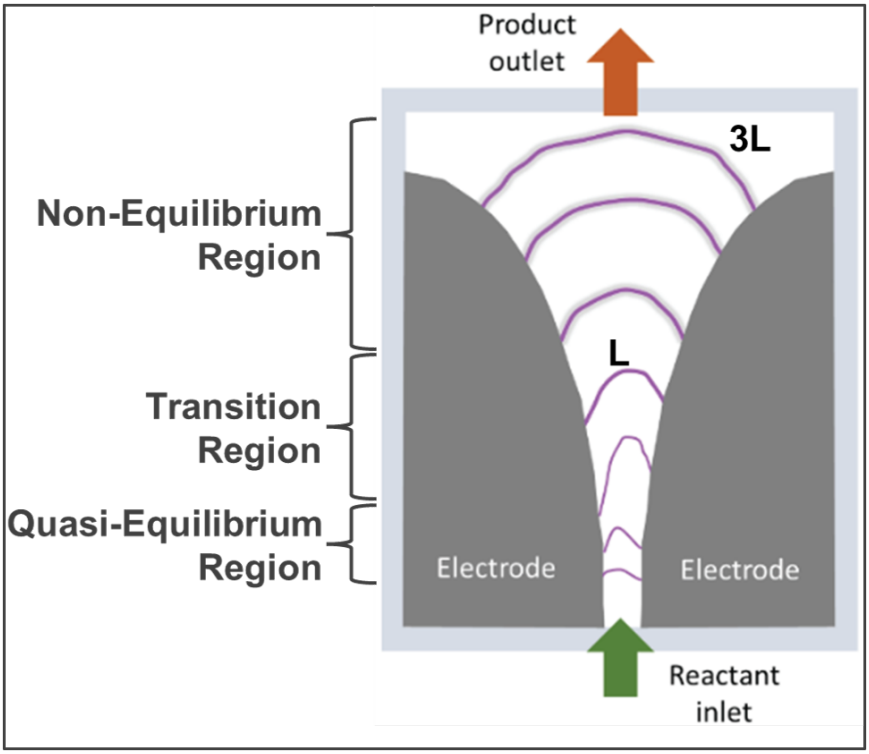

Figure. 2.12: The different regions of a planar gliding discharge demonstrating how it transitions from a thermal plasma to a non-thermal plasma. As the discharge lengthens and cools, it transitions from an equilibrium to a non-equilibrium plasma. The figure also shows the critical length L and the length at total extinction 3L. [51]

Even though GDs are hybrid plasma devices combining attributes of TP and NTP with better energy efficiency than other NTP generating devices and setups with catalysts, they are not widely studied for ammonia synthesis applications [52]. Most of the studies explore NO_x production, which could then be used to generate ammonia.

A study where a simple PGD reactor was used to study the effect of different factors on NO_x production using a pulsed power supply found that increasing the frequency, pulse width, and amplitude resulted in a higher concentration of NO_x in the exhaust gases. It was also found that the addition of oxygen to the air feed gas resulted in a further increase. However, the best energy efficiency reported was 4.8 MJ/mol, which is almost an order of magnitude larger than thermal catalysis processes. The researchers in the study suggest that improving the reactor geometry could possibly result in an improvement in the efficiency. The researchers also recognized a major issue with PGD reactors; the volume of gas between each two consecutive discharges never has a plasma ignited through them. This drawback could potentially be remedied by a number of methods, including inducing vortices to ensure reactive species spend a longer time inside the reactor, thus increasing their residence time [49].

The study also compared the average speed of discharge gliding or propagation to the average gas flow speed and found that they are almost equal to within a reasonable error, which is what is expected. However, it was seen that higher flow rates or gliding speeds resulted in a decrease in the overall volume treated or volume between discharge ignition and extinguishing. The faster flow rates force the discharge to elongate faster along the center compared to the sides, reaching 3L faster than at slower flow rates [49].

A different study for NO_x production using a PGD reactor found that higher frequencies were ideal. A high frequency of around 14 kHz was used to drive the discharge. This high frequency, like with other types of discharges, ensures the discharge does not thermalize and ensures strong non-equilibrium conditions in the region between L and 3L. Thus, providing rapid quenching of products which is optimal for NO_x production. In this study, the effect of different electrode materials and flow rates with air as the feed gas was studied, with the best energy efficiency of 2.8 MJ/mol of NO_x achieved at the highest flow rate of 6 L/min using molybdenum electrodes. However, the concentration of NO_x produced was less than half compared with slower flow rates. However, these slower flow rates consumed more energy per mol of NO_x produced; around 3.8 MJ/mol. It should be noted that these values are competitive compared with DBD, glow, and other NTP producing devices even without catalysts. Thus, combining it with a catalyst and further work to address the shortcomings of PGD reactors could yield huge improvements in both efficiency and conversion rate [49].

Unlike with nitrogen fixation applications, PGD reactors and other configurations of GD reactors have been widely studied for carbon conversion applications. One such study used a TiO_2 catalyst adhered to a flat tray to oppose the flow of the gas, hindering the gliding motion of the discharge and resulting in strong backflows and vortices. It was found that introducing the catalyst in this manner resulted in a 133% increase in the energy efficiency from 5.4 to 12.6%. The conversion of CO_2 to CO also saw an increase of around 138% from 4.6 to 10.8%. The researchers attribute some of the increase to the flow disruption but mostly to the addition of the catalyst itself and its activation via photocatalysis and other synergistic effects. These values were

obtained for the lowest flow rate of 2 L/min and with the catalyst at a distance of 5 mm from the end of the electrodes. While this was the best reported gas conversion, the reported efficiency increased with the flow rate and the distance of the catalyst tray from the electrodes to a value of around 29% at a flow rate of 7 L/min and a distance of 20 mm. This value is competitive when compared with the other NTP generating devices discussed previously. For comparison, thermal dissociation of CO_2 to CO at 2000 K has a modest conversion of about 1.5% with an efficiency of 4.4%. Thus, making GD reactors attractive for carbon conversion [53].

Although there is a lot of potential in GDs for nitrogen fixation and carbon conversion, they have some limitations and need to be further studied in order to get them industry-ready.

2.2 Boron Nitride Nanotubes as a Catalyst Carrier

Transition metals (TMs) are commonly used as catalysts in chemical reactions as they exhibit catalytic properties due to their ability to accept and give electrons from their d-orbitals [54]. These catalysts simply increase the rate of the reaction or selectivity towards a certain product without being used up in the process. In the previous subsections, we saw how a variety of metals and alloys have been used in conjunction with plasma sources for plasma catalysis, thus increasing the energy efficiency, conversion rate, or both. However, TM catalysts have limitations since a reaction can only be catalyzed on the surface where there is direct contact between the catalyst surface and gases [55]. Therefore, the reactions are limited, not by the amount of catalyst, but by the surface area or active sites where reactions can take place. To achieve high surface areas, TMs are usually supported by materials with

high porosity, such as Al_2O_3, TiO_2, MnO_2, or BEA-zeolites, to increase surface area [55]. When using an Al_2C_3 (alumina) support for ammonia synthesis, the TM weight percentage is usually in the range of 2 to 10%.

Other than a high porosity, the support material needs to be thermally and chemically inert or stable [55]. Boron Nitride Nanotubes (BNNTs), discovered in 1995, offer a suitable candidate [55]. BNNTs offer a catalyst support medium with a high surface area for TM impregnation. Moreover, they are electrically insulating and have a high thermal stability, making them ideal for use in extreme reactive conditions. Although structurally analogous to carbon nanotubes (CNTs), BNNTs have different physical properties that make them better suited for catalyst support applications [55]. Most notably, they are thermally stable, allowing them to be used at temperatures as high as 800°C [56]. They were also shown to be stable in NTPs [56]. Moreover, as opposed to CNTs which are reactive, BNNTs are said to be chemically inert. Even though they are inert, in 2019, Iannitto *et al.* [57] showed that NH_3 can bind with the surface of BNNT in a high energy NTP. This unique property may prove to have some synergistic effects on the catalysis reaction.

Despite the fact that we are aiming to study ammonia synthesis at atmospheric temperature and pressure, we need to ensure any catalyst support is able to withstand high temperatures. This is because, as seen in a paper published in 2021 by Burbach *et al.* [2], different TM catalysts perform better and achieve better activity at temperatures between 300 and 500 °C. Thus, there is an advantage to heating the catalyst to achieve catalytic activation. However, even though the catalyst needs to be kept at these elevated temperatures, and since only a small amount of catalyst is

used, the energy used to heat the catalyst does not compare to the energy needed to heat up the bulk gases as required for the Haber-Bosch process.

To summarize, BNNTs can prove extremely useful for the combined plasma catalysis process being studied as they provide a large surface area for metal deposition while being chemically and thermally stable. The heating required for the catalyst and BNNT support could likely be achieved solely by the plasma heating itself. However, the feasibility of such a claim needs to be and will be delved into later in this study.

It should be noted that in this study, the BNNTs were formed into sheets just a few μm thick or "buckypaper" (BNNT-BP) to be used as a catalyst carrier [56]. The BNNT-BP sheets were obtained from the National Research Council (NRC) of Canada with the exact method outlined in a paper by Kim *et al.* [58]. The BNNT-BP were then treated, prepared, and coated by Steven Walker from the Catalytic and Plasma Process Engineering (CPPE) lab at McGill University. The TMs themselves were deposited on the BNNT-BP using pulsed laser ablation of metal targets.

2.3 Computational Fluid Dynamics (CFD) Basics

In cases where some flow or thermal data cannot be directly measured, simulations could provide a good alternative. Computational Fluid Dynamics is a tool in fluid mechanics that uses a computer to numerically model, analyze, and simulate fluid flows, obtaining its physical properties, such as velocity, density, pressure, and temperature. The computer simultaneously solves a system of fundamental equations including the

continuity, momentum, and energy equations to simulate the free-stream fluid flow and its interactions with surfaces using user-defined boundary conditions.

The first of the three equations is the continuity equation [59]:

$$\frac{D\rho}{Dt} + \rho(\nabla \cdot \overrightarrow{v}) = 0 \tag{2.2}$$

where ρ is the density of the fluid, t is the time, $\overrightarrow{v}$ is the velocity, and ∇ is the gradient operator shown below [59].

$$\nabla = \overrightarrow{i}\frac{\partial}{\partial x} + \overrightarrow{j}\frac{\partial}{\partial y} + \overrightarrow{k}\frac{\partial}{\partial z} \tag{2.3}$$

If the fluid is assumed to be incompressible, the density is constant and consistent everywhere. Thus, the term $\frac{D\rho}{Dt}$ goes to zero and Equation 2.2 simplifies to [59]:

$$\nabla \cdot \overrightarrow{v} = \frac{\partial u}{\partial x} + \frac{\partial v}{\partial y} + \frac{\partial w}{\partial z} = 0 \tag{2.4}$$

Next, we have the momentum equation which describes the relationship between forces acting on a fluid and the resulting fluid motion. It is often referred to as the Navier-Stokes equation which is shown below [59].

$$\rho\left(\frac{\partial v}{\partial t} + v \cdot \nabla v\right) = -\nabla p + \mu\nabla^2 v + \rho g \tag{2.5}$$

where p is the pressure, μ is the viscosity coefficient, ∇^2 is the Laplacian operator (divergence of gradient), and g is the acceleration due to gravity. If the fluid is again

assumed to be incompressible and with a constant viscosity coefficient, Equation 2.5 simplifies to [59]:

$$\rho\frac{Dv}{Dt} = -\nabla p + \mu\nabla^2 v + \rho g \tag{2.6}$$

Finally, the energy equation or Newton's first law of thermodynamics is solved if information about temperature and heat transfer is desired. The equation is shown below [59].

$$\Delta U = Q - W \tag{2.7}$$

where ΔU is the change in internal energy, Q is the heat added to the system, and W is the work done by the system. This equation can be developed for fluid flows to obtain Equation 2.8 below [59].

$$\rho\left(\overbrace{\frac{\partial h}{\partial t}}^{\text{I}} + \overbrace{\nabla\cdot(hv)}^{\text{II}}\right) = \overbrace{-\frac{\partial p}{\partial t}}^{\text{III}} + \overbrace{\nabla\cdot(k\nabla T)}^{\text{IV}} + \overbrace{\phi}^{\text{V}} \tag{2.8}$$

where h is the enthalpy and k is the thermal conductivity. The rest of the terms are defined below.

I : Local change in time

II : Convective term

III : Pressure work

IV : Heat diffusion term

V : Source term

Now, to solve this system of equations, a software such as ANSYS Fluent or CFX (ANSYS, Inc) is used to discretize the volumes and obtain the results. Figure 2.13 shows the flow chart of the CFD process.

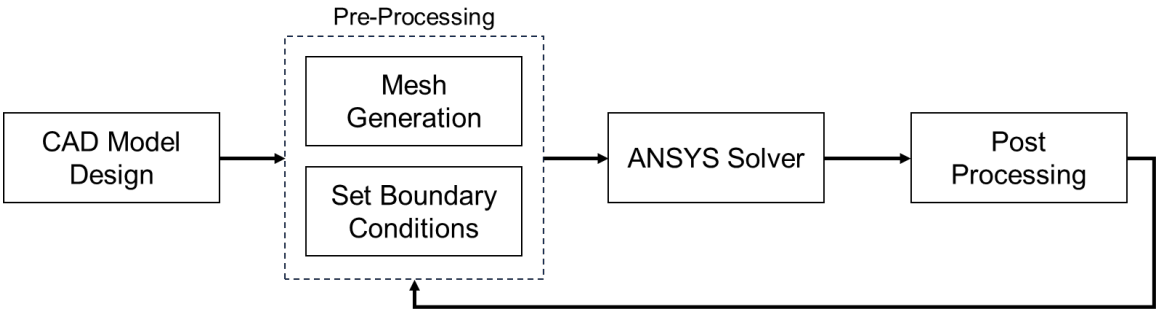

Figure. 2.13: The flowchart of a CFD process using ANSYS solvers. The process starts from the CAD design to pre-processing, solver, and finally, post-processing. The flowchart also shows the iterative nature of the process. (adapted from [60])

The process starts with designing a CAD model either using the built-in ANSYS function or using an external software such as SOLIDWORKS (SOLIDWORKS Corp.) or Fusion 360 (Autodesk, Inc). The model is then imported into the mesh generator which discretizes the domain into small cells or elements in order for the solver to apply the mathematical model to each element in the next step. Finer meshes with smaller elements usually result in better results and easier convergence of results. However, there are many other limitations and factors when it comes to producing the mesh. This is usually an iterative process where a mesh is generated and then its quality is assessed using a metric called skewness. For reliable results, the skewness, which ranges from 0 to 1, should be kept below 0.95. Thus, the mesh parameters and types are varied iteratively until a good quality mesh is achieved. An example of a mesh can be seen in Figure 2.14. To reduce the computation time and due to a limitation on the number of elements, the fluid domains are prioritized with

a finer mesh as opposed to solid domains. However, for conformity, element sizes of solids in contact with the fluid domain have a much finer mesh than the rest of the solid.

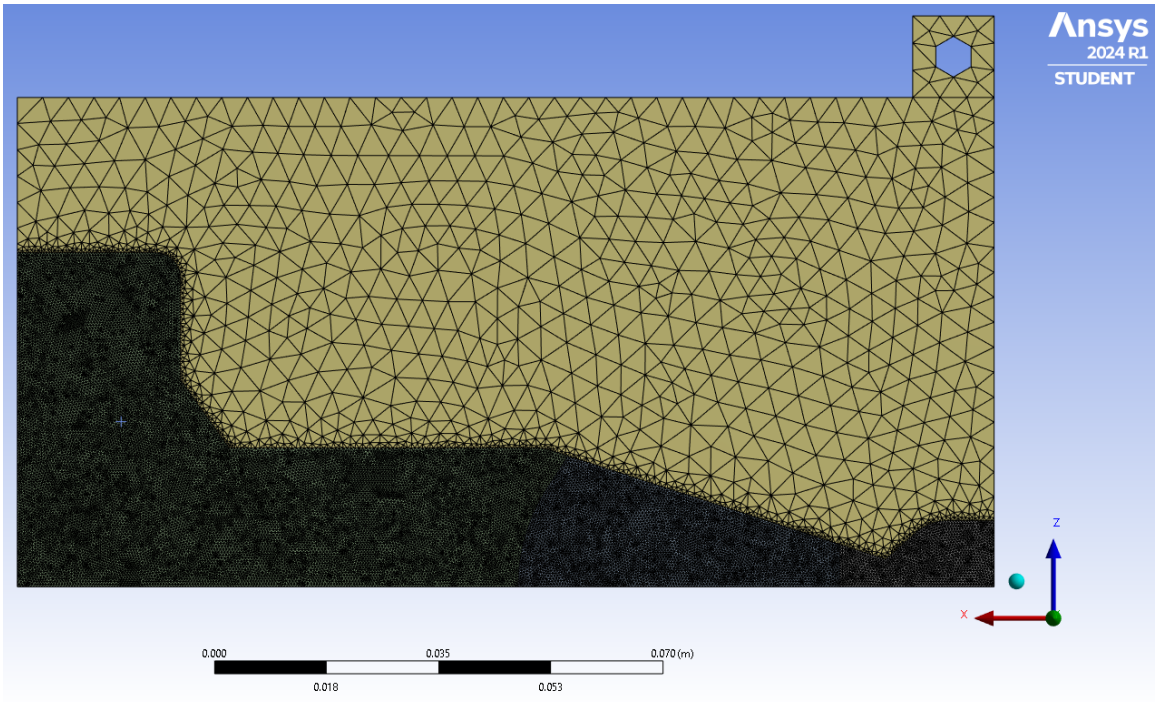

Figure. 2.14: A screen-grab of a CAD model imported into the ANSYS mesh generator. The body with the fine mesh is a fluid (nitrogen gas) while the body with the coarse mesh is a solid (brass electrode). The difference in mesh size is due to the complexity of the solution and its importance.

After the mesh is generated and evaluated, it is uploaded into the ANSYS solver (Fluent in this study) where the boundary conditions and domains are defined. Finally, the user sets the convergence tolerance and number of iterations and then runs the solver. The results are then uploaded into CFD-Post to generate reports and display the results as vectors, contours, and through other visual mediums.

In the ANSYS Fluent solver, one important thing to set is the turbulence mode of the flow. Fluent comes equipped with a range of modes, but the two most used modes are k-epsilon and k-omega SST. These two modes work for a wide range of applications with fully turbulent flows or transitional flows. However, for laminar flows, the laminar mode is better suited and much simpler. To determine which of these three modes to use, an estimation of the Reynolds number is required. For Reynolds number less than 2000, the flow is considered laminar. Thus, the laminar turbulence mode should be used. For values higher than 2000, other turbulence modes might be more suitable. The Reynolds number can be calculated using Equation 2.9.

$$Re = \frac{\rho v L}{\mu} \tag{2.9}$$

where Re is the Reynolds number, ρ is the density, v is the velocity of flow, L is the characteristic length, and μ is the dynamic viscosity.

2.4 Infrared Thermal Imaging

In this study, there is a need to measure temperatures and capture 2D temperature distribution. These measurements are used to validate the CFD model developed. Although thermocouples could provide some information about temperature and are great due to their wide operating range, ease of use, and low cost, they can only provide temperature readings at a certain point and are not suitable for use in a plasma environment. Moreover, there is a difficulty in achieving proper physical contact between the thermocouple and solid surfaces whose temperature is to be investigated. Thus, thermocouples would not be ideal in this case. Another way to

measure the temperature that would circumvent the issues stated earlier is infrared (IR) thermography or IR imaging.

IR imaging is a non-invasive method that uses IR radiation to generate an image where the pixels represent temperature values, giving us the temperature distribution or contour of the object imaged. Devices used to capture IR images are usually referred to as IR cameras. These IR cameras measure the spectral IR radiation emitted by a surface and relate that to the temperature using Planck's radiation law for blackbodies seen below in Equation 2.10.

$$I(\lambda, T) = \frac{2h{c_o}^2}{n^2\lambda^5} \frac{1}{e^{\frac{hc_o}{n\lambda k_B T}} - 1} \tag{2.10}$$

where $I(\lambda, T)$ is the spectral blackbody intensity, λ is the wavelength, T is the temperature in Kelvin, h is Planck's constant, c_o is the speed of light in vacuum, n is the refractive index ($n \approx 1$ for most gases), and k_B is the Boltzmann constant.

This equation is used for blackbodies, which are ideal bodies that are perfect absorbers and emitters; absorbing all incident radiation onto them and emitting the maximum radiation for a given temperature. However, real objects absorb and emit fractions of the radiation. This fraction is the emissivity, which is a value between 0 and 1 and is specific to the surface and material. A value of 1 is a blackbody as described previously, while a value of 0 is a perfect reflector (a perfect mirror). Objects in the real world have emissivity values between 0 and 1, and IR cameras take that into consideration to provide more accurate temperature readings. IR cameras usually allow a user to input a known or measured emissivity value.

Summary

The goal of this study and thesis is to help advance the efforts to electrify society (mainly industrial processes) through zero-carbon or carbon-neutral fuel production. Out of the different methods being examined, NTPs show great potential due to their compatibility with renewable energy sources and an improvement to the theoretical energy efficiency over traditional thermal catalysis processes. As seen in the literature presented, Gliding Discharge Plasma reactors combined with a physical catalyst deposited on BNNT BP sheets might result in a much-needed breakthrough in this field. However, there are gaps in the current research, especially when it comes to the optimization and characterization of the reactor. Thus, a GD reactor was designed, optimized, and tested. The design, setup, and results will presented and discussed throughout the course of this thesis.

Chapter 3

Reactor Design and Setup

3.1 Overview of Experimental Apparatus and Setup

This section provides an overview of the experimental setup, illustrated with a combined schematic-P&ID diagram that details the different components in the system used to run the reactor and acquire data. The subsequent subsections will delve deeper into the reactor design and the design of the different systems.

Figure 3.1 shows all the components in the setup, comprising three different systems working together: the reactor, gas delivery system, and power delivery system. The reactor itself is made of several components assembled to create a volume where a set of electrodes through which electrical power is delivered to the gas flow, ionizing it to create plasma. The gas is fed into the reactor by the gas delivery system, consisting of a gas tank (or more), a mass flow controller, and nylon tubing. The gas, nitrogen or air in this study, is supplied from the tanks through a pressure regulator into the mass flow controller, which varies the flow rate from 0 to 5 SLPM based

on the user input. The gas is then fed into the reactor where power is applied to it through the power delivery system. This second system consists of a signal generator, a high-voltage amplifier, an oscilloscope, a high voltage probe, and a current measuring transformer. In this system, an AC signal of frequencies between 5 and 12 kHz is generated by the signal generator and supplied to the high-voltage amplifier to amplify the voltage by a factor of 2000, achieving the required high breakdown voltages. The high-voltage amplifier then supplies the high voltage signal and sufficient power to one of the two electrodes while the other is grounded. Finally, the oscilloscope is used to capture, display, and record the voltage and current signal using a voltage probe and current transformer. Occasionally, a high-speed camera or an IR camera is pointed perpendicularly to the PGD reactor to obtain thermal profiles or high-speed images for analysis.

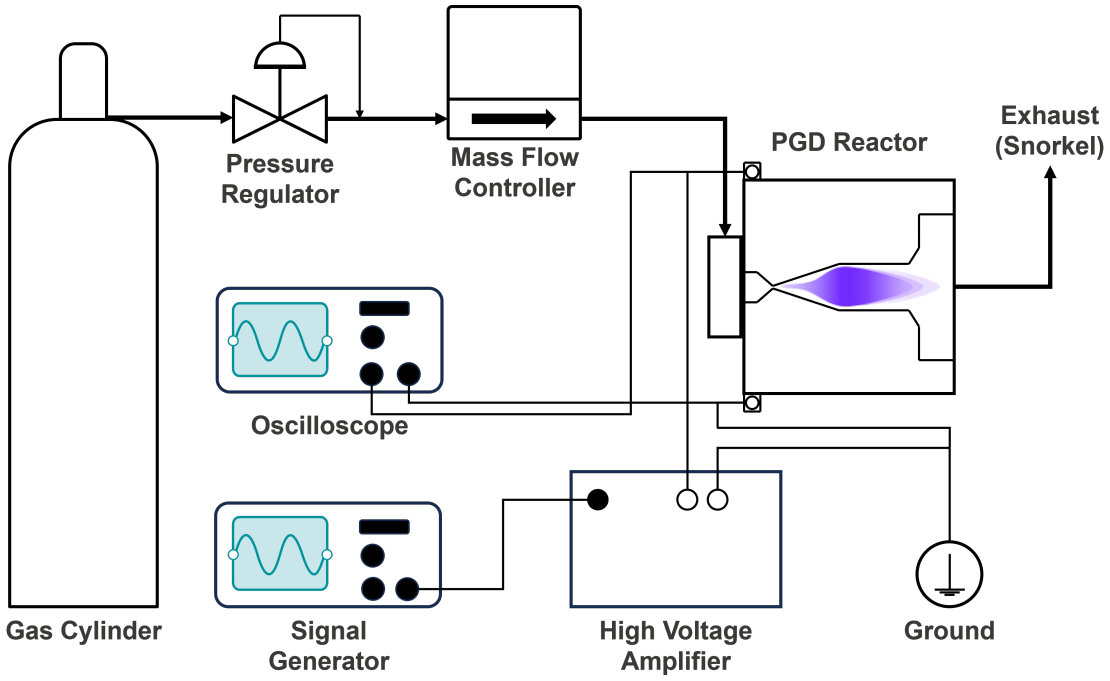

Figure. 3.1: Combined schematic and P&ID diagram for the experimental setup detailing the different components in the system and the connections between them. The thick arrows represent tube connections between components of the gas distribution section. The thin lines represent electrical connections between the electrical supply and measurement system.

3.2 Gliding Discharge Reactor Design

GD reactor designs in their most basic forms consist of a pair of diverging metal electrodes with a gas delivery system or pipe injecting gas along the inner edge of the electrodes. An example of such a system can be seen in Figure 3.2 below. This system is not confined with reactor walls which can make it not ideal for gas conversion reaction and diagnostics. Since there is no confined volume where the injected gas and generated plasma can flow, the exact flow rate and gas composition inside the reactor is difficult to ascertain. Moreover, the composition of the gases at the "outlet"

would not provide accurate information about the conversion rate. Finally, the plasma discharge might be subjected to a larger degree of quenching since it is exposed to the environment. This might have detrimental effects on the energy efficiency.

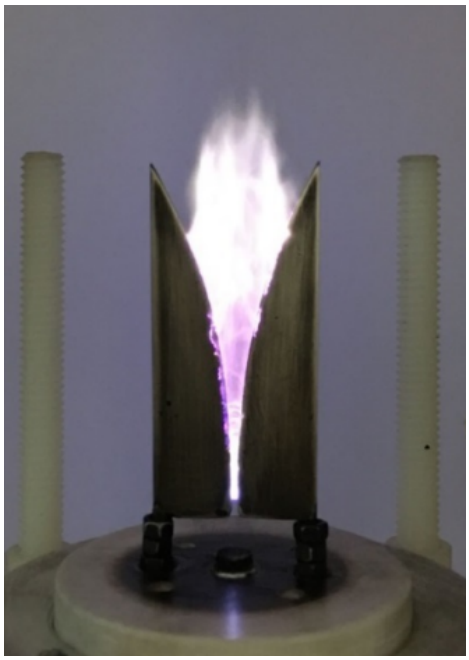

Figure. 3.2: An unconfined Planar Gliding Discharge generating device with two divergent electrodes and a gas inlet at the bottom. The figure shows the possible unpredictable behavior of the gliding discharge reactors. [61]

To circumvent this, GD reactors for gas conversion applications usually are contained inside a container. On of the simplest means to achieve containment is by sandwiching the two planar electrodes between two plates. Those two plates should be made of an electrical insulator, be able to withstand elevated temperatures, and completely enclose the reactor volume between the two electrode edges except for an inlet and outlet. Although there are a few ceramic options that would be great for this application, for the sake of diagnostics and the need to visually observe the discharge, a transparent option is best. Two square GE Type 124 Commercial Grade

Fused Quartz plates are used as the reactor walls in this case. The quartz sheets are produced by Technical Glass Products, Inc. with some important properties presented in Table 3.1 below. From the electrical resistivity and maximum temperature, we can see that quartz is indeed a good choice. The remaining properties will be more relevant in later chapters of this thesis.

Table 3.1: Properties of the quartz used to confine the reactor volume and act as its walls. [62]

Property	**Value**
Size	15.2 cm × 15.2 cm × 0.635 cm
Density	$2200\,\mathrm{kg\,m^{-3}}$
Thermal Conductivity	$1.4\,\mathrm{W\,m^{-1}\,{}^{\circ}C^{-1}}$
Maximum Temperature (Strain Point)	$1120\,^{\circ}\mathrm{C}$
Electrical Resistivity	$7 \times 10^{9}\,\Omega\,\mathrm{m^{-1}}$

To ensure the reactor is well confined, gaskets are inserted between the metal electrodes and the two quartz plates to ensure an airtight seal. The gaskets could also be used with any other solid-solid interfaces. A great option for the gaskets are PTFE or "Teflon" sheets. These sheets can withstand high temperatures, are chemically stable, and are compressible. The ability to withstand high temperature and reactive environment is ideal for use in plasma reactors and its compressibility makes is perfect for use as a gasket. For this study, a 30.5 cm x 30.5 cm PTFE gasket sheet 0.159 cm in thickness was acquired from McMaster-Carr.

To put the entire assembly together, a pair of Low-Profile C-Clamps were used on either side of the reactor. The clamps ensure the quartz plates and metal electrodes are locked in place by providing compressive forces on the top and bottom quartz plates. This stress forces the PTFE gasket to compress forcing it into any imperfections on the electrode surface and evacuates any air in the solid interfaces. Thus, the

clamps help ensure an airtight seal as well as keep everything together. The clamps, seen in Figure 3.3, are made of aluminum while the screw is made of steel. The clamp was obtained from McMaster-Carr and has a maximum reach of 3.81 cm.

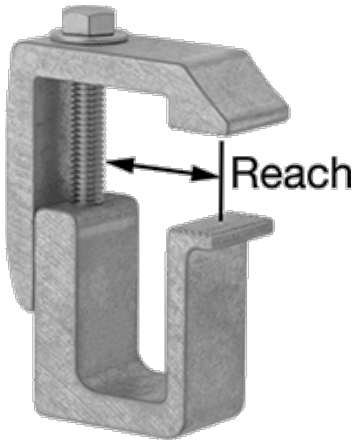

Figure. 3.3: Low-Profile C-Clamp with a reach of 3.81 cm used to put the reactor assembly together and ensure an airtight seal. [63]

3.2.1 Electrode Design

The main design parameters for the reactors to be determined are the dimensions, the electrode spacing and the shape of the gliding edge. The dimensions of the quartz plates can help us design the electrodes and obtain their dimensions. For ease of assembly, the electrodes should be designed to be flush with the four edges of the quartz plates. This would allow us to simply align the edges and ensure that all the other spacings and measurements automatically conform.

As for the electrode spacing or the shortest gap between the electrodes, this can be determined with the help of Paschen's Equation (2.1). In this study, 0.318 cm thick brass sheets are machined to produce the electrodes. In Equation 2.1, Brass's

secondary emission coefficient (γ) was set to 0.01 [2], V_b was subtracted from both sides, and the equation was rewritten as seen below in Equation 3.1.

$$\frac{Bpd}{ln(\frac{Apd}{ln(1+1/\gamma)})} - V_b = 0 \tag{3.1}$$

The values of constants A and B are shown Table 3.2 below for the gases likely to be used in this study. As for V_b or the voltage, it will likely be a variable in this experiment. Thus, for the equation above was solved using a MATLAB script to get appropriate electrode spacings for the different gases at a range of applied voltages. The results can be seen in Figure 3.4 below.

Table 3.2: Gas breakdown constant A and B to use in Paschen's equation to determine maximum electrode spacing for gas breakdown at a range of applied voltages. Constants provided for hydrogen, nitrogen, oxygen and carbon dioxide gases. [64]

Gas	A $(cm^{-1}Torr^{-1})$	B $(V/cm.Torr)$
H_2	4.8	136
N_2	11.8	342
O_2	6.5	190
CO_2	20.0	466
Ar	12.0	180
Air	15.0	365

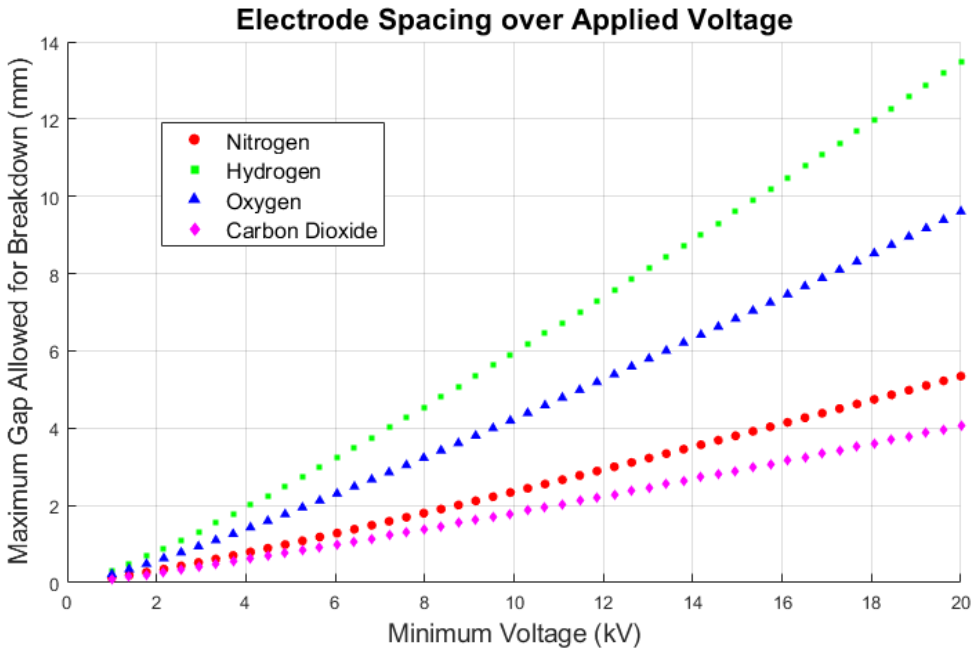

Figure. 3.4: Graph showing the maximum electrode spacings for different gases over a range of applied voltages at atmospheric pressure. The figure includes plots for nitrogen, hydrogen, oxygen, and carbon dioxide.

We can see that for gaps beyond 3 mm, the required breakdown voltages for CO_2 and N_2 is very high; around 16 kV and 12 kV, respectively. Therefore, we need to ensure that the design of the electrodes has a much smaller gap. A gap of around 2 or 1.5 mm should allow for breakdown at relatively lower voltages for all the gases.

The last step in the electrode design is to determine the shape of the inner electrode edge the discharge glides on. For that, a simple straight divergent electrode edge was chosen. This brings us to the first electrode design shown in Figure 3.5 with the complete reactor CAD design seen in Figure 3.6.

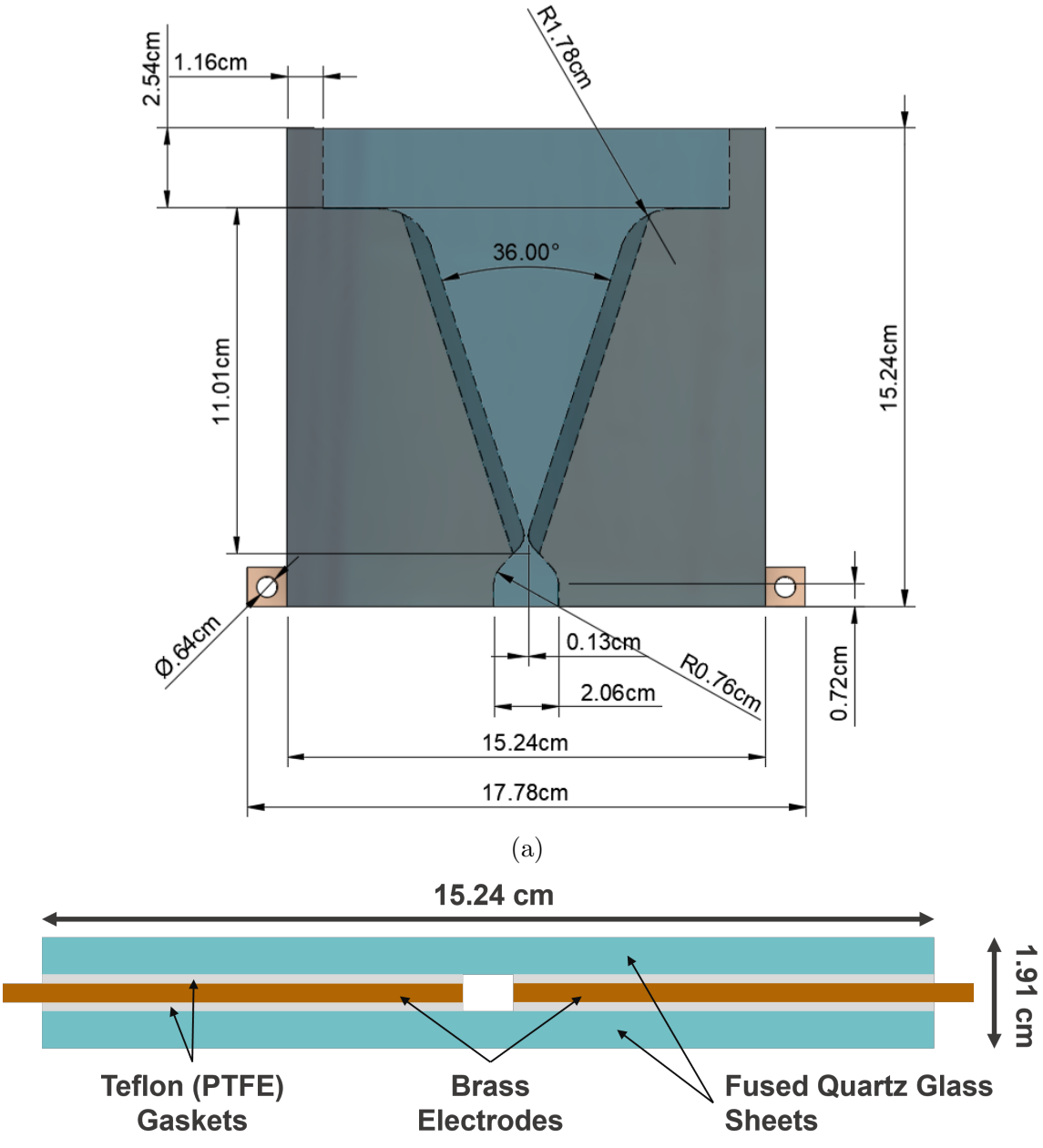

(a)

(b)

Figure. 3.5: Electrode Design 1 with a straight divergent gliding edge. (a) Top View of the PGD reactor CAD design with the appropriate dimensions in inches. (b) Cross Section of the PGD reactor design showing the different layers and how the electrodes are sandwiched between the quartz plates with PTFE gaskets at the solid interfaces. Appropriate dimensions are given.

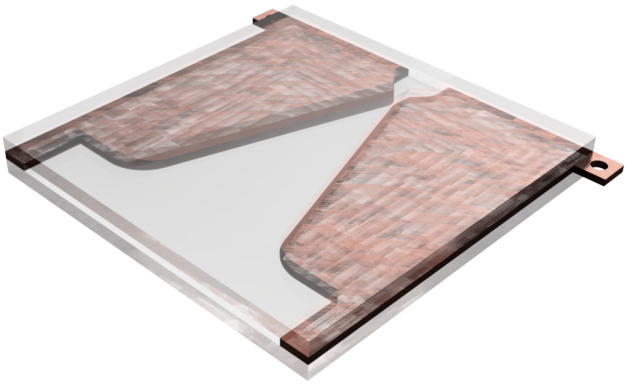

Figure. 3.6: Rendered Electrode Design 1 CAD image showing how the electrodes are sandwiched between two quartz plates.

In the figure above, you can see how each of the electrodes have three edges that align with 3 edges on both the top and bottom quartz plates. Again, this ensures the electrodes fit and their spacing (1.5 mm) are as designed. However, two protrusions on the side of each electrode can be seen. These allow easy electrical connection both to the power source and the ground using nuts and bolts.

Another feature of the design is the 45 degree chamfer applied to the gliding edge which allow us to restrict the gliding of the discharge to the very edge of the electrode. Thus making it more consistent and uniform. The final feature of the design is the rapid increase in the gap between the electrodes before the end of the quartz plates or the reactor volume. This ensures the discharge is confined in the plasma volume.

When this first electrode design was tested using a 2.5 SLPM flow of 99.999% pure nitrogen gas, the discharge was only able to glide about a quarter of the distance. This was determined using long exposure camera images. Due to the divergent nature of the electrode, the volume of treated gas does not increase linearly as the discharge

glides further. Figure 3.7 shows the volume of gas ignited or treated along the axial distance of the reactor.

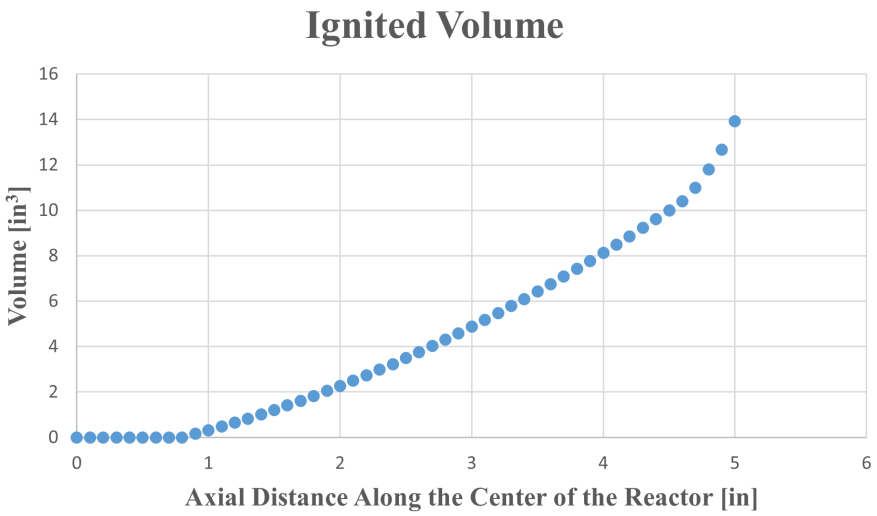

Figure. 3.7: Design 1 ignited or plasma treated volume as the discharge glides further along the reactor. The plot shows how the volume of treated gas does not increase linearly with the glided distance.

The ignited volume is shown to increase in an increasing manner with the gliding distance. Thus, ensuring the discharge glides further, would maximize the treated volume and would likely have positive effects on the conversion rate. Therefore, a less divergent electrode design was created. Design 2 is identical to Design 1 in every aspect except that it has a less divergent angle of 24° rather than 36°. Figure 3.8 shows the ignited volume scatter plot for Design 2.

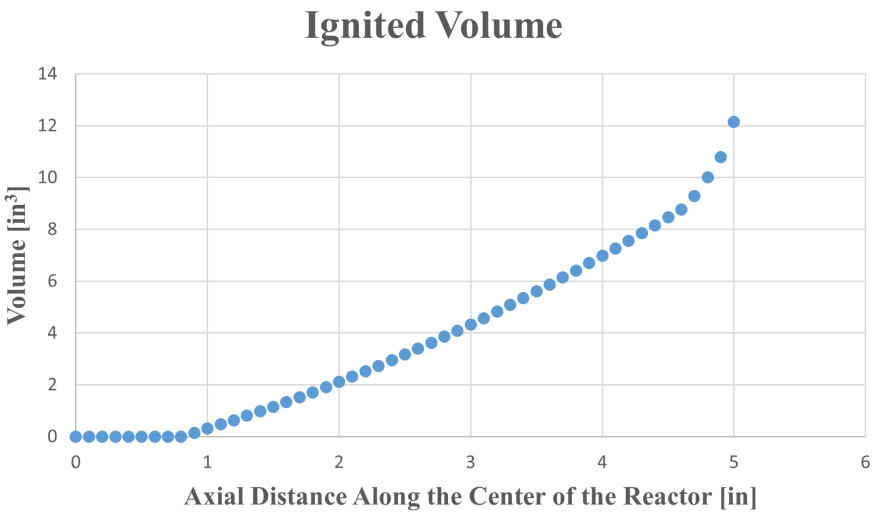

Figure. 3.8: Less divergent electrode Design 2 ignited or plasma treated volume as the discharge glides further along the reactor. The total volume at the same glided distance is reduced in Design 2. The less divergent nature allows the discharge to glide further.

The discharge in Design 1 glided around 1.5 inches corresponding to an ignited volume of around 3 in^3. On the other hand, the discharge in Design 2 glided around 2.5 inches at the same operating conditions corresponding to an ignited volume of around 6 in^3. This results in a percentage increase in treated volume of around 100%. However, this still only represents less than half the maximum possible ignited volume. Therefore, a third design was adopted. Simply decreasing the diverging angle would result in the discharge gliding further. However, this comes at the cost of the total reactor volume. Moreover, this would increase both the TP and NTP regions of the GD. A different electrode design might be able to achieve larger ignited volumes focusing more on maximizing the NTP regions as it is more desirable for gas conversion applications.

Design 3, seen in Figure 3.9, resulted from an analysis of a long exposure image of the gliding discharge in Design 2 to determine the point where the discharge terminates or where it reaches length 3L. If the electrode edge is straightened out before that point, the discharge could be forced to glide further without dissipating. This is likely to increase the volume of the reactor between L and 3L, or the NTP region.

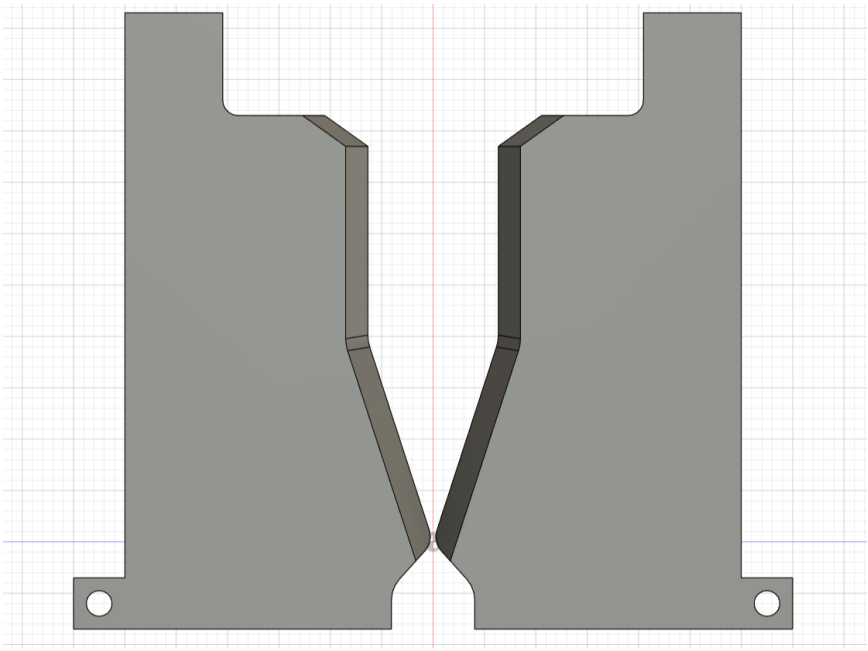

Figure. 3.9: Design 3 with a straightened out edged to allow the discharge to glide further increasing the ignited volume and NTP region. This is achieved by delaying the point at which the discharge reaches a length of 3L.

The figure below shows the approximate point where the discharge reaches a length L, the point where Design 2 reaches 3L, and where Design 3 reaches 3L.

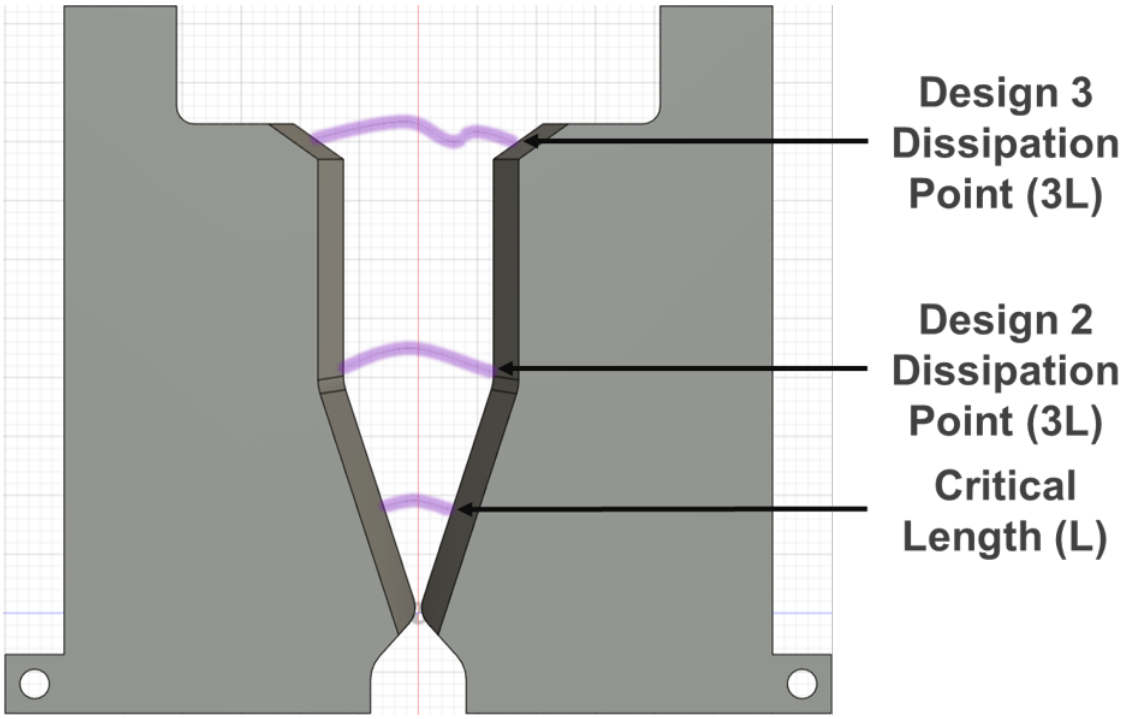

Figure. 3.10: The locations of L and 3L for both Design 2 and 3 for comparison. The point where the discharge reaches is moved further down from the ignition point in Design 3 as opposed to Design 2.

In Design 3, we theoretically increased the NTP region between L and 3L. However, this comes at the cost of the frequency of discharge re-strike, thus increasing the volume of untreated gas between each two consecutive glides. For Design 2, each glide takes on average $110.94\,\text{ms} \pm 1.53\%$ as opposed to $194.79\,\text{ms} \pm 1.50\%$. This corresponds to re-strike frequencies of $9.01\,\text{Hz} \pm 1.53\%$ and $5.13\,\text{Hz} \pm 1.50\%$, respectively. Thus, the re-strike frequency of Design 3 is $43.03\% \pm 1.96\%$ less than that of Design 2.

The effect of both parameter, NTP volume & re-strike frequency, is likely too complicated to ascertain without running experiments with reactive gases and measuring conversion rates and energy efficiencies whilst varying the operating conditions.

However, this brings us to the final electrode design. A picture of the actual machined pair of electrodes can be seen in Figure 3.11.

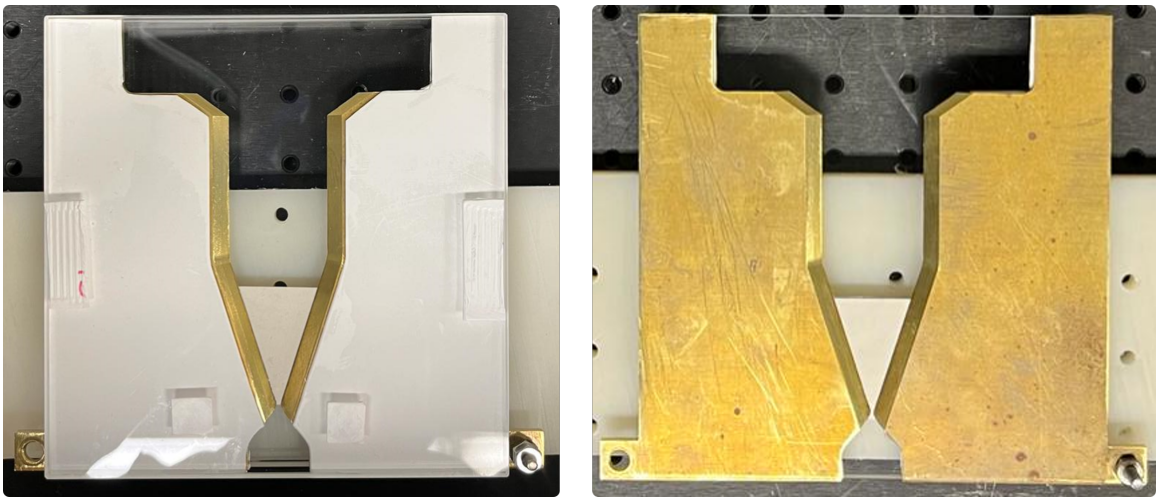

Figure. 3.11: Design 3. Brass machined electrodes assembled (left) and disassembled (right). The PTFE gasket can be seen covering the electrodes on the left apart from the gliding edge.

To better see the difference between each of the 3 different electrode designs, a CAD assembly of all three designs on top of each other can be seen in Figure 3.12.

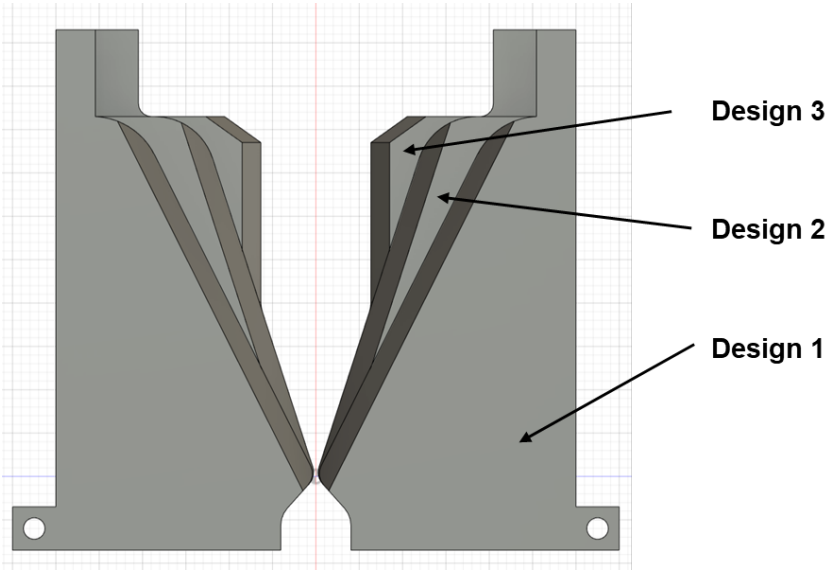

Figure. 3.12: Designs 1, 2, and 3 CAD forms overlaid for easy comparison. This shows the difference in the angle of the electrodes as well as the straight edge of Design 3.

3.3 Gas Delivery System

The first supporting system for the PGD reactor is the gas delivery system, which consists of a mass flow controller (Brooks Instruments, 5850s), shown in Figure 3.13, supplying pure N_2 (ALPHAGAZ 1, 99.999%) from a tank into the reactor through a gas injector. The gas is transported between the tank, MFC, and gas injector using 0.432 ID $\times$ 0.635 OD $\times$ 0.102 cm wall nylon 11 tubing. After it is injected into the reactor and ignited, it then exits through the open outlet and flows into the exhaust or lab snorkel. It should be noted that the outlet is kept open as the experiments are run at atmospheric pressure.

(a) (b)

Figure. 3.13: The MFC and it's electronic unit used to set the flow rate and display actual measured flow rate. (a) Brooks Instruments 5850s MFC. (b) MFC electronic control and display unit. [65]

The MFC rate is calibrated with nitrogen gas supplied at 60 psi. Therefore, if the low pressure gauge on the tank's gas regulator is set at 60 psig, there MFC controller should provide accurate flow rates between $0 - 5\,\mathrm{SLPM} \pm 0.5\%$. However, we do not expect the flow to be stable throughout the flow rate range. Thus, the actual tested flow rate range is likely more limited than what is possible using the MFC.

3.3.1 Gas Injector Design

The gas injector should interface with the nylon tubing and allow the injection of the gas in a relatively uniform manner in the region behind the electrode shortest gap. The injector should be an electrical insulator to prevent a short circuit across the electrodes. It should also be easily machinable and able to withstand elevated temperatures. These criteria eliminate a lot of options; metals for their excellent

electrical conductivity and plastics for their poor high temperature performance. A more viable option would be ceramics which meet all the criteria. After checking the McMaster-Carr website, a High-Temperature Easy-to-Machine Glass-Mica Ceramic Bar was acquired. The stock piece is 1.91 × 1.91 × 7.62 cm in size. The ceramic bar was then machined with a 0.797 cm diameter hole 4.19 cm down the center. The first 1.27 cm section of the hole is threaded to fit a Universal Thread for Air and Water male tube fitting for tube OD 0.635 cm. On one of the large faces of the piece, 7 equally spaced 0.127 cm holes are drilled perpendicularly to intersect the larger central hole. These holes allow the transported gas to be injected uniformly into the reactor. The CAD form of the gas injector can be seen in Figure 3.14.

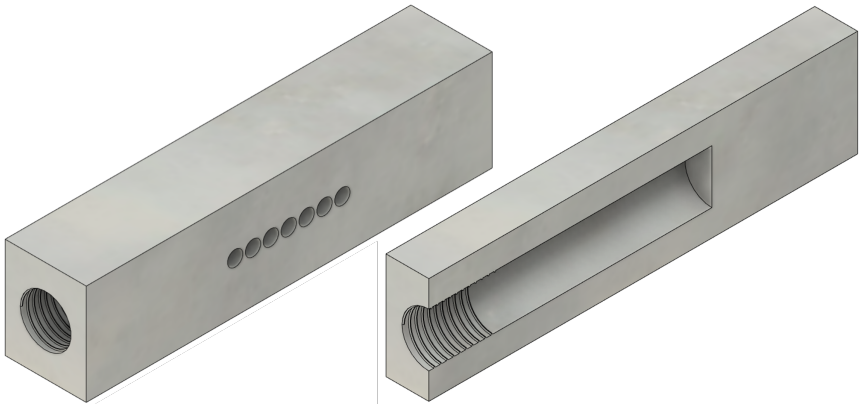

Figure. 3.14: Gas injector machined out of a 1.91 × 1.91 × 7.62 cm) glass-mica ceramic bar. The injector is an electrical insulator, capable of withstanding high temperatures, and inject gas uniformly. On the left is the CAD form while a section view is shown on the right. With the design cut down the middle, interior features can be observed.

To attach the gas injector to the rest of the assembly, a horizontal force needs to be applied to secure it in place. This could be achieved by using a three-way clamp, as depicted in Figure 3.15. The two opposite bolts are used to secure the clamp to the

top and bottom quartz surfaces, while the third perpendicular bolt is used to push the gas injector into the back of the reactor. The holes on the injector are aligned with the inlet of the reactor, and gas gaskets are used to ensure an airtight seal.

Figure. 3.15: Three-way C-clamp used to secure the gas injector to the rest of the reactor assembly. The two opposing heads on the clamp rest on the top and bottom quartz surface with pressure to secure the clamp. The remaining head pushed sideways on the gas injector to push it flush onto the reactor at the inlet. [66]

The gas injector makes up the last component of the PGD reactor. However, it might still not be clear how all the components go together. Figure 3.16 shows the assembled PGD reactor with electrode Design 2 (for illustrative purposes only). The image is labeled showing the electrodes, PTFE gasket, quartz glass sheets, clamps, and gas injector.

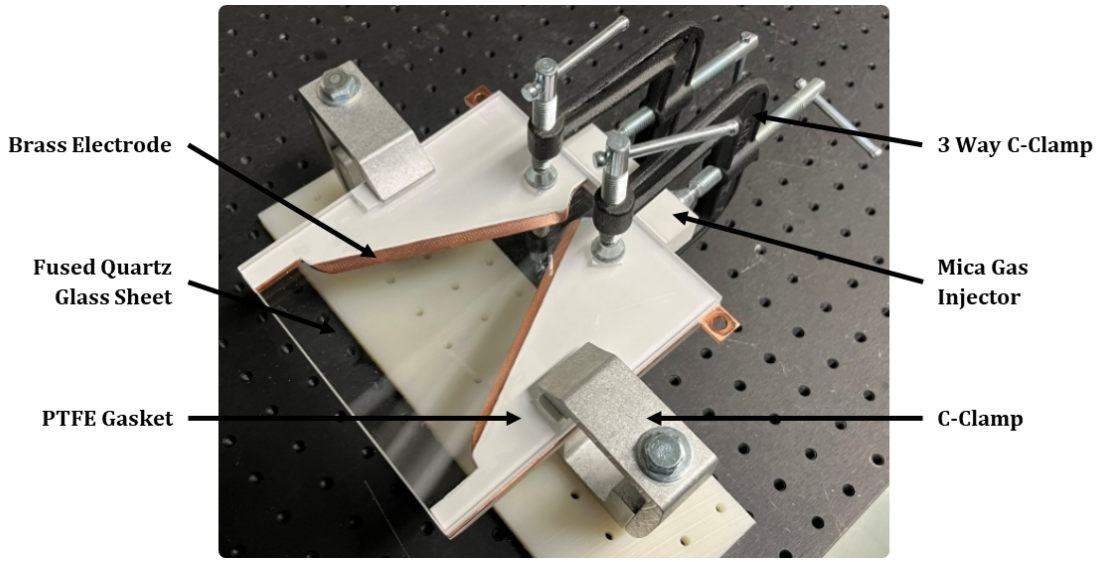

Figure. 3.16: Labeled image of the PGD reactor assembly with electrode Design 2. The figure shows the electrodes, PTFE gaskets, quartz glass sheets, clamps, and gas injector all secured together using four clamps.

3.4 Electrical Supply and Measurements

An AC current was used to power the PGD reactor in this project. The AC signal is supplied by signal generator (SIGLENT, SDG 1032X), shown in Figure 3.17, with a max output frequency of 30 MHz. However, we are unlikely to operate at such high frequencies which veer into the RF discharge regime. The actual operating frequency range would be determined based on the stability of the discharge at each tested flow rate. From the initial trial tests, the frequencies resulting in stable discharges are in the range of $4 - 12$ kHz.

Figure. 3.17: SIGLET signal generator. used to generate the AC signal to be amplified and used to drive the PGD reactor. The signal generator allows the amplitude and frequency of a sinusoidal signal to be set by a user. [67]

The signal generator used can only supply a signal with a voltage amplitude of ± 10 V and a maximum power output of 2 W [68]. As seen in Figure 3.4 for nitrogen at the design minimum electrode gap of 1.45 mm, a voltage of at least 5.5 kV is required for discharge ignition. Thus, a voltage amplifier (Trek, 20/20C), shown in figure 3.18, is used to amplify the voltage amplitude of the AC signal with a fixed gain of 2000 V/V and a maximum power of 400 W. The output of the signal generator is connected to the input port on the amplifier. The amplified signal from the high voltage output port is connected to one of the two electrodes on the reactor using a well insulated wire. The other electrode is connected to the lab ground connection using alligator clips. The amplifier itself is also grounded.

Figure. 3.18: Trek high-voltage amplifier labeled image showing the input port, high-voltage outlet, power cord, main connection, power switch, and high-voltage lock off. This device amplifies the AC signal generated by x2000. [69]

Finally, the current through and voltage across the reactor electrodes were measured and recorded for later analysis in Chapter 4. To record the electrical data, an oscilloscope (Tektronix, MSO2012) was used. The oscilloscope is connected to a high-voltage probe (Tektronix, P6015A) and a wide-band (1 Hz − 20 Mhz) current transformer (Pearson Electronics, Inc., Model 411). All the listed components can be seen in Figure 3.19. The high voltage probe measures the voltage applied to the electrode with a ground reference and a 1000X attenuation. The high voltage probe has a high bandwidth of around 75 MHz. Combined with the oscilloscope's bandwidth up to 100 MHz and the current transformer's wide-bandwidth, enables us to measure fast high voltage and current signals with sample rates up to 1 GS/s. The accuracy or uncertainties associated with the voltage measurements are presented below in Table 3.3.

(a)

(b)

(c)

Figure. 3.19: The components needed to measure and record the high-voltage and current through the PGD reactor. (a) Tektronix oscilloscope MSO 2012 to read, display, and record the data [70]. (b) High-voltage probe Tektronix P6015A to meaure the voltage [71]. (c) Current transformer Pearson Electronics model 411 to measure the current [72].

This concludes the main sub-systems and reactor design sections. A complete visualization of the entire setup can be seen in Figure 3.20. The figure is labeled to show the reactor assembly as well as all the apparatus in both supporting systems.

Table 3.3: The uncertainties associated with the voltage measurements taken using the oscilloscope and high voltage probe. Note: Terms in "div" are to be converted into volts by multiplying by the corresponding "volts/div" term.

Uncertainty	Value
DC Balance	± (1 mV + 0.1 div)
DC Gain Accuracy	± 3%
Offset Accuracy	± (0.01 × (offset − position) + DC Balance)

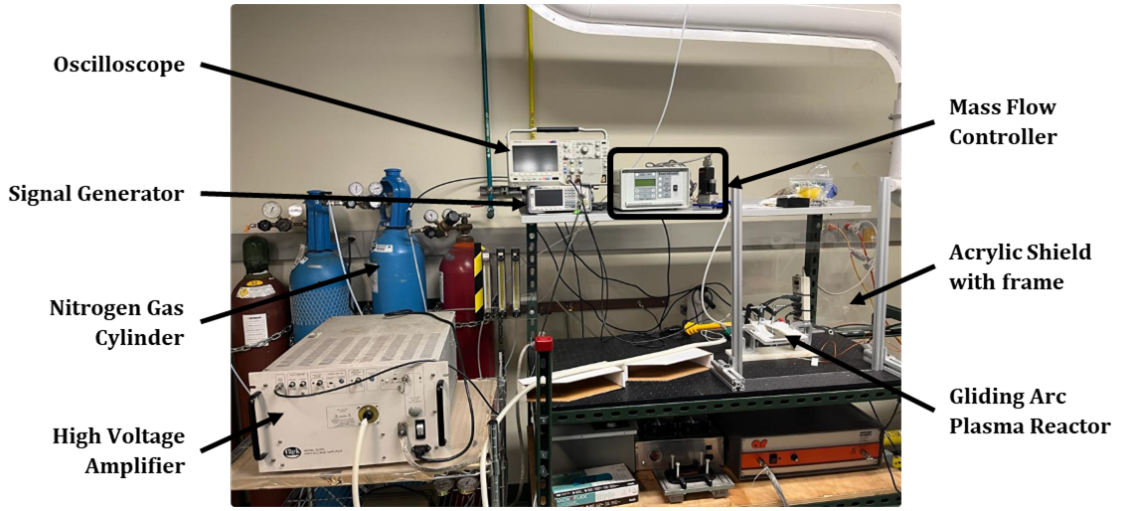

Figure. 3.20: The complete labeled experimental setup showing the PGD reactor, electrical system apparatus, and gas delivery system apparatus.

3.5 Temperature Distribution Measurements

For our purposes, there are two different IR cameras that can be used to measure the 2D temperature distribution of the reactor's top quartz surface as explained in 2.4. Table 3.4 shows the different specification for both the cameras. These different specifications will help narrow down the camera selection to determine the ideal one for our purposes.

Table 3.4: The technical specifications for the two available IR cameras are provided. The table presents the temperature range, spectral range, and IR resolution of the FLIR A500 and A6260 cameras.

	FLIR A500 [73]	FLIR A6260 [74]
Temperature Range	-20°C to 2000°C	400°C to 1200°C
Spectral Range	7500 – 14000 nm	900 – 1700 nm or 600 – 1700 nm
IR Resolution	464 × 348	640 × 512

It is difficult at this stage to have an idea of the surface temperatures expected. Thus, it is difficult to narrow the selection based on the temperature. However, we do not expect the bulk gas temperature or the temperature of the reactor to be excessively hot, making the FLIR A500 a more sensible choice. Moreover, and since we need to measure the outside temperature of the quartz surface, we need to examine the transmittance curve, shown in Figure 3.21, of the used material (Commercial Grade Fused Quartz Ingot) and compare it with the spectral ranges of both camera. This is to ensure that the quartz plate appears opaque to the cameras to enable us to measure its surface temperature distribution.

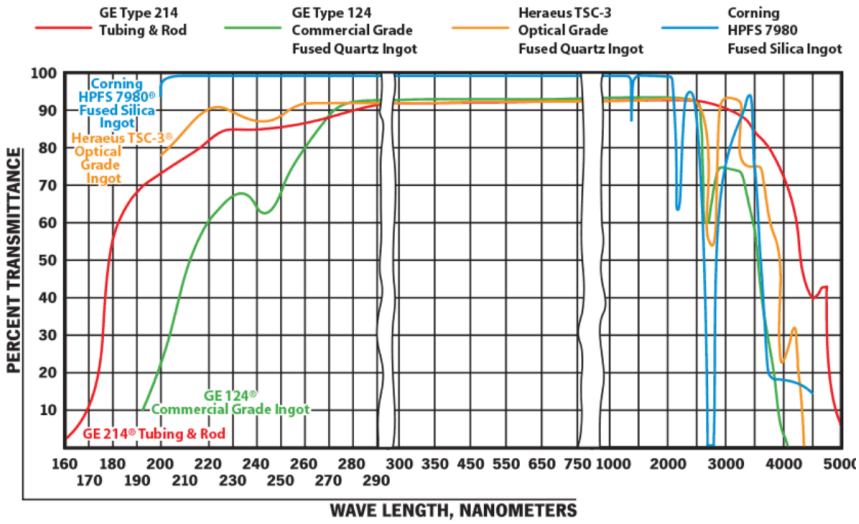

Figure. 3.21: The transmittance graph for different types of quartz sheets from Technical Glass Products. The quartz sheets used in this study are GE Type 124 Commercial Grade Fused Quartz Ingots shown in green. This type of quartz has a transmittance of around 93% between 280 and 2000 nm. [75]

The transmittance curve of the quartz sheets used in this study is shown in green on the graph. As can be seen, this quartz (GE Type 124) has the highest consistent transmittance between 280 and 2000 nm. This means that about 93% of radiation in this range will pass through while radiation outside this range will not, which is what we need. Looking back at the spectral range for each of the two cameras available, we can see that only the FLIR A500 operates outside the transmittance range of the quartz GE Type 124 plate. Therefore, it is the one most suitable for our purposes.

Figure 3.22 shows pictures of both cameras with the FLIR A500 on the left side.

(a) (b)

Figure. 3.22: The two IR cameras available for use in the Catalytic and Plasma Process Engineering Lab. (a) FLIR A500 for measuring temperatures between -20 and 2000°C [73]. (b) FLIR A6260 for measuring temperatures between 400 and 1200°C [74].

Chapter 4

Preliminary Characterisation of the PGD Reactor

A gap in the characterization of PGD reactors was previously identified. This gap is manly due to the simplicity of the PGD reactors and their potential use in gas conversion which invites researchers to jump directly into experimental work with minimal understanding of the reactor's working mechanism. In this chapter, we take a step back by running experiments for the purposes of characterizing the designed PDG reactor. The experimental procedure will be provided followed by an examination of the data collected. The preliminary characterization involves the examination of the general behavior of the gliding discharge using the voltage and current signals and the examination of localized behavior along the plasma treatment region.

4.1 Experimental Procedure and Conditions

This section outlines the assembly steps and experimental procedure including any steps needed to ensure the experimenter and any other personnel in the lab are safe. The high voltages and high temperature natures assosiated with the use of this reactor as well as the UV radiation emitted by the plasma are all potential hazards, and proper measures to mitigate their risks are essential.

Step 1: Assembly of PGD Reactor

First, the appropriate PPE including safety goggles, lab coat, long pants, closed-toed insulating shoes are worn. Next, four gaskets are cut out of a 0.159 cm thick PTFE (Teflon) gasket sheet. The gaskets need to cover the entire top and bottom surfaces of both electrodes excluding the cut "knife" edge of the electrodes. This can be done by printing drawings of the electrode CAD designs to scale and tracing the drawing onto the PTFE sheet. The electrodes are then sandwiched between the gaskets and subsequently placed onto one of the quartz plates with the cut edges facing each other. The external perimeter of the electrodes needs to be aligned with the outside edges of the quarts plates (refer to Figure 3.16). This ensures the shortest distance between the electrodes is 1.5 mm. Two c-clamps (Figure 3.3) are used on either side to ensure the assembly is secure and airtight. Finally, two three-way c-clamps are used to secure the gas injector to the inlet side of the reactor (refer to Figure 3.16).

Step 2: Electrical System Set Up

Once the reactor is assembled, the electrical and gas systems can be set up. First, the signal generator output is connected to the high-voltage amplifier input. Both

apparatus and everything should be off at this point and during the entire set up process. Next, the current transformer is connected to Channel 1 on the oscilloscope and the high-voltage probe is connected to Channel 2. Again, the oscilloscope should be off during this process. Next, a proper high voltage cable is connected to the output port of the high voltage amplifier and fed through the current transformer. The cable is then attached to one of the electrodes at the intended extrusion on the side of the electrode using a bolt, a pair of washers, and two nuts. Care is taken to ensure the cable does not lay on top of the metal workbench using insulating spacers (e.g., plastic or cardboard). The high voltage probe is connected to the same extrusion using an alligator clip cable. The other electrode is grounded using a second alligator clip cable. For safety, the metal clamps are also grounded using alligator clip cables. The grounding of the metal workbench is also inspected regularly.

Step 3: Gas Delivery System Set Up

For the gas system set up, the appropriate gas tank is inspected to ensure it is in working condition and has a pressure of at least 250 psi. Nylon tubing is then used to connect the tank to the mass flow controller which is in turn connected to the gas injector using the appropriate tube fittings. The gas tank's main valve must remain shut off up to this point. Finally, the main valve is turned on leaving the outlet valve to the flow controller closed. The working pressure can the be adjusted to required pressure by the flow controller or 60 psi.

Step 4: System Initialization and Operation

Upon completing the set up process, some steps are required to initialize the system prior to running the experiment. First, the lab snorkel or exhaust is positioned

close to the outlet of the reactor to capture the outlet gases. This is necessary as some ozone might be formed and it is considered to be a pollutant at ground level and can be harmful. Next, all the apparatus, valves, and recording devices are inspected to ensure everything is off. At this point, the gas delivery valve on the gas tank regulator can be gently turned on. The mass flow controller is then switched on and set to the desired flow rate (e.g, 60% = 3 SLPM). Next, the signal generator and oscilloscope are switched on. The signal generator is set to the required frequency using the appropriate dial leaving the peak-to-peak voltage at 1 V and the output off. The oscilloscope is set to display both the current and voltage data on the screen factoring the appropriate scaling factors presented in the previous chapter.

At this point, the high voltage amplifier is switched on, the output button on the signal generator is pushed, and the high-voltage lock off button is pushed. The peak-to-peak voltage can then be turned up using the appropriate dial until breakdown or the desired voltage is achieved. The set up is inspected for any sparks or faulty connections. The flow rate, frequency, and voltage settings are adjusted as needed. The experiment is observed from behind an acrylic shield to protect from UV radiation as seen in Figure 3.20.

Step 5: Data Collection

The current and voltage waveforms from the oscilloscope are recorded on a flash drive for analysis. The recorded data is saved as an Excel file onto the flash drive. The file consists of the oscilloscope settings as well as the electrical data of around 3 or 4 different glides of the discharge depending on the re-strike frequency (and gas flow rate).

The FLIR camera presented previously is utilized during the course of the experiment to track the peak temperature of the top quartz plate surface of the reactor to determine when the reactor reaches steady-state. Once the temperature plot over time flattens, snapshots of the top quartz plate surface are saved as radiometric JPEG images with temperature values for each pixel. The maximum temperature, mean temperature, and any other required data is saved for each run.

Step 6: Shutdown Procedure

After the experiment is concluded, the following steps are performed in the order in which they are listed to shutdown the system.

1. The amplifier is turned off by pushing the lock off button and then switching the power off.
2. The output from the signal generator is turned off, the voltage is brought down to the minimum, and then signal generator is switched off.
3. The oscilloscope is switched off.
4. The gas cylinder main valve is turned off while leaving the mass flow controller running to drain the line. Once the flow rate reduces to 0%, the mass flow controller is switched off, the pressure delivery valve is gently turned off, and finally the main valve is turned off.
5. The once live electrode and other metal parts of the reactor assembly are grounded using an alligator clip cable.

In case of emergency: The same steps as above are followed but ensuring the high-voltage lock off button (refer to Figure 3.18 on the amplifier) is pushed first and foremost.

4.2 Electrical Data Characterization

4.2.1 General Observations

In initial trials of the PGD reactor, it was seen that the discharge is stable over a certain range of gas flow rates and electrical signal frequencies. The lowest stable flow rate was found to be around 2.5 SLPM or the 50% flow rate setting on the mass flow rate controller utilized in this study. Furthermore, through trial and error, it was observed that as the flow rate increases, the signal frequencies range where the discharge is stable expands. For example, at the lowest stable flow rate of 2.5 SLPM, the discharge is only stable at frequencies between 5 kHz and 11 kHz. On the other hand, for a flow rate of 5 SLPM, the discharge is stable up to a frequency of 20 kHz. For the sake of this experiment, within the scope of this thesis, we only need to get a general understanding of the workings of the PGD reactor. Due to the small difference between the maximum and minimum possible frequencies, the characteristic of the discharge are not expected to change. There could possibly be changes to conversion rates or efficiencies but it is outside the scope of this thesis. Thus, for the results presented, the frequency was kept constant at 5 kHz while the flow rate was varied from the lowest to the highest stable values (2.5 and 5 SLPM). The frequency was varied only to allow us to study the flow characteristics in the reactor. This data is presented and discussed in the next chapter.

As the discharge glides along the electrodes, the voltage it draws from the power source increases with the gap between the electrode edges. While we can use Figure 3.4 and the design minimum gap length to calculate a theoretical plasma ignition voltage around 5 kV, we can not obtain a theoretical maximum voltage. Thus, to set the voltage on the signal generator, the data from test runs were analyzed. It was seen that the voltage required by the discharge never surpassed 8 kV peak to peak. This corresponds to 4 V peak to peak signal from the signal generator. The signal generator was, therefore, set at 4.5 V peak to peak which is then amplified by the high-voltage amplifier to 9 kV peak to peak. The table below summarises the variable or settings for each of the main runs conducted for the purposes of this chapter.

Table 4.1: Variables and setting for the first four runs of the PGD reactor running nitrogen gas for the initial characterization.

Run Number	Gas	Voltage [kV]	Frequency [kHz]	Flow Rate [SLPM]
1	N_2	9	5	2.5
2	N_2	9	5	3.5
3	N_2	9	5	4.5
4	N_2	9	5	5.0

The settings and observations above are for nitrogen gas which was the main gas used for the characterization. However, compressed dry air and argon were also tested and analyzed. Some of these results are presented in this thesis. Any data, figures, or images of the aforementioned gases will be clearly labeled for clearness.

Nitrogen gas was fed into the reactor at a rate of 2.5 SLPM and a 5 kHz signal was applied to one of the electrodes. This resulted in a purplish pink discharge being formed at the shortest distance. The discharge then glided in a stable manner along the edge of the electrodes until the termination point starting the cycle all over again.

Figure 4.1 below is a sequence of images showing the stages of the discharge during one glide.

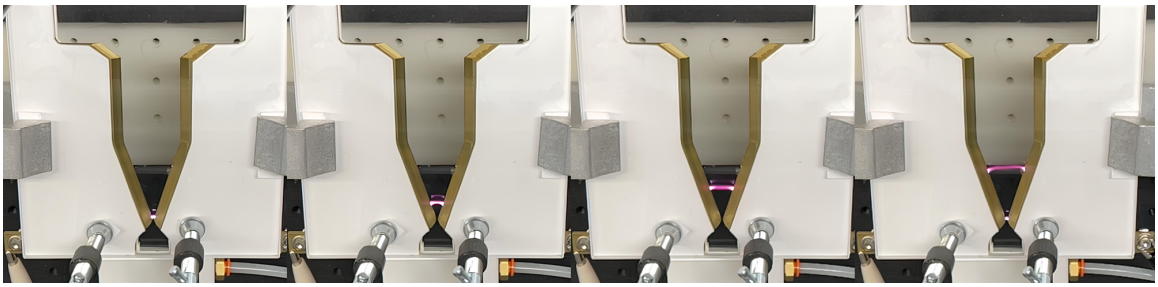

Figure. 4.1: Sequence of images displaying the stages of the discharge from ignition to termination over one glide. Nitrogen gas at 2.5 SLPM was used in this run and a voltage of 9 kV (peak to peak) at a frequency of 5 kHz was applied across the electrodes.

The discharge produced is highly stable and consistent from one glide to the next, this behavior is highly important for characterization. The stability of the glide was observed both visually be the experimenter and using the electrical data, mainly the voltage, recorded or continuously displayed on the oscilloscope during the course of the experiment. An example of the voltage data recorded can be seen below in Figure 4.2. This raw data was read and plotted using a MATLAB script. The figure shows three distinct triangular or trapezoidal shapes each of which represents one glide of the discharge. These shapes are very consistent signalling the stability of the discharge. Another observation was the symmetrical nature of the discharge. Unlike with a DC power supply, where cathode spots form and anchor the discharge, hindering its movement, this AC driven PGD reactor does not experience cathode spots. This leads to uniform erosion of the electrode edges.

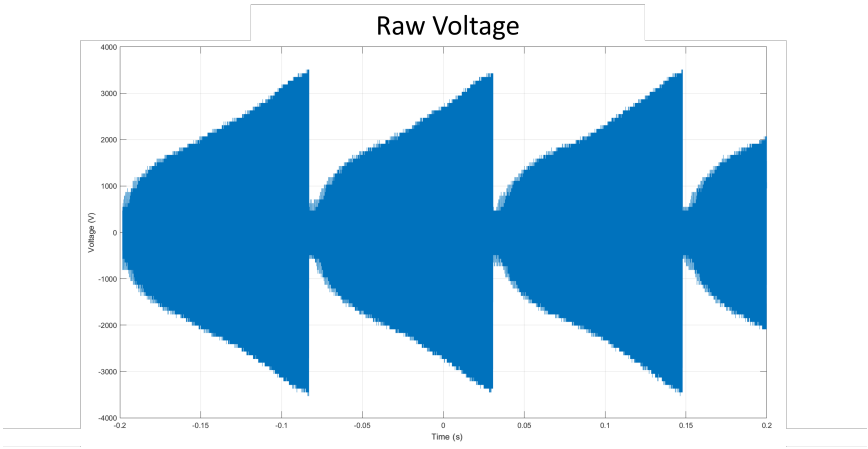

Figure. 4.2: Recorded raw voltage as a function of time for the first run using electrode Design 3 with nitrogen gas at 2.5 SLPM. The plot shows the repetitive nature of the discharge with three similar triangular voltage profiles corresponding to one glide each.

It should be noted that, again, an AC signal at 5 kHz was used for this run. This fact is not clearly seen when looking at the signal for such a large time scale from -0.2 to 0.2s. This is because each AC cycle only takes about 0.0002s. Thus, it is necessary to reduce the range on the x-axis to view the AC signal behavior. Later on in this section, it will be necessary to do just that.

4.2.2 Recorded Electrical Data

It was explained previously that the voltage requirement of the discharge grows linearly with the distance between the electrode edges or the inner electrode spacing. A more accurate statement is that it grows with the length of the discharge which in turn grows with inner electrode spacing. However, the electrode length is usually larger than the inner electrode spacing due to the discharge's freedom to arc or

bulge in any of the three dimensional axes. This behavior of the discharge is better displayed in Figure 4.3.

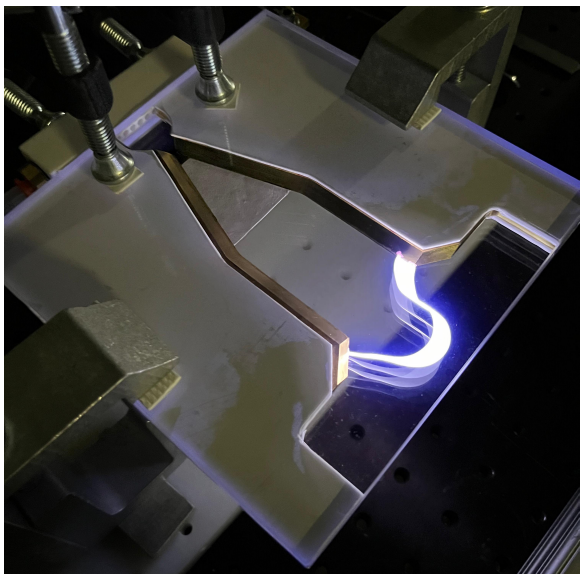

Figure. 4.3: PDG reactor with electrode Design 3 running dry air at 3 SLPM with an applied voltage of 9 kV (peak to peak) at a frequency of 7 kHz. The discharge can be seen glowing a bright blue/purple having glided to the end of the electrode edge as per design bulging as it does so due to drag forces (discussed further in Chapter 5)

Comparing Figures 4.1 and 4.3, one can notice how the air plasma discharge is able to glide all the way to the end, unlike the nitrogen discharge. Looking back at Figure 3.4, specifically at the plot for nitrogen and oxygen, it can be seen that at the same voltage, oxygen gas can undergo breakdown at a higher spacing; it is easier to ionize. This may explain the observed phenomenon where the air plasma is able to lengthen more before termination. This is because air is essentially nitrogen diluted with some oxygen at a ratio of around 4:1, respectively. However, the observed phenomena might also be explained by the higher rate of cooling experienced by the discharge with N_2. This higher degree of cooling can force the discharge to reach the

point where the heat dissipated equals the power supplied to the plasma ($\dot{Q}_{out} = \mathrm{P}_{in}$) at a shorter length. This might be due to the fact that N_2 radiates more than air. A sample of the voltage over time data obtained for the PGD reactor running air at can be seen in Figure 4.4 below.

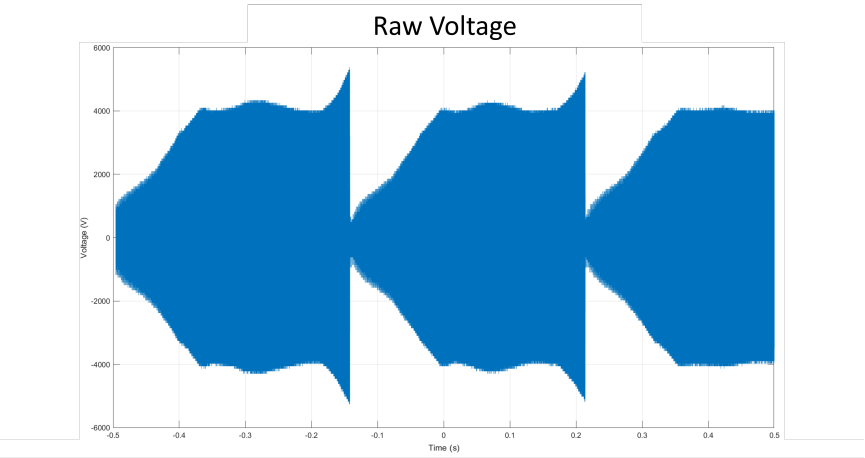

Figure. 4.4: Recorded raw voltage as a function of time for the first run with dry air using electrode Design 3 at 3 SLPM with an applied voltage of 9 kV (peak to peak) at a frequency of 7 kHz. The voltage profile of each of the glides again suggests consistency. The profiles also seem to follow the shape of the electrode gliding edges.

From the figure above, one can see three consecutive glides. The shape of the voltage signal in this case looks different as the discharge was able to glide all the way to the end of the electrode edge. The relatively linear voltage rise observed with the voltage signal with N_2 is followed by a relatively flat voltage section with air. Infact, the shape of this voltage signal follows the shape of the entire inter-electrode gap. This is better illustrated with Figure 4.5 shown below. Using this figure, one could study the waveform at different points in time and use it to draw conclusions on the discharge behavior at the approximate corresponding locations on this figure and,

ultimately, on the actual electrode edges. The figure also suggests that the electric field is quite constant between the electrodes.

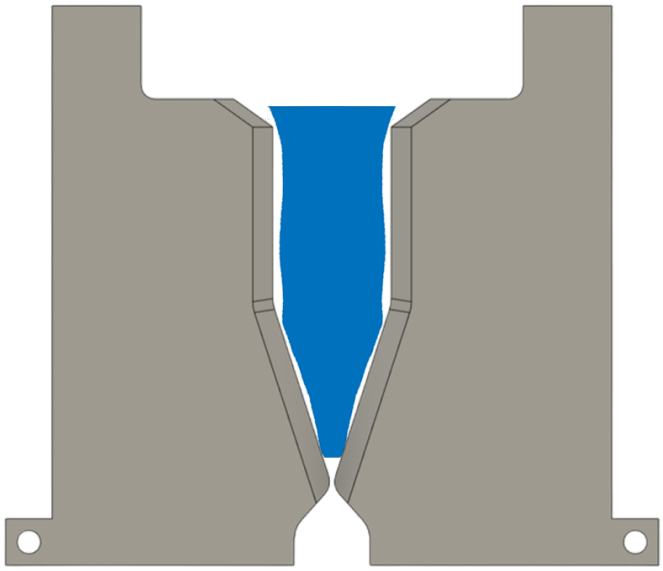

Figure. 4.5: Overlapping the voltage signal corresponding to one glide of the air plasma discharge over a CAD drawing of the top view of the PGD reactor's electrodes. This allows for observations to be made and related to positions or approximate locations on the electrode edges.

At this point, we can look closely at different slices of the waveform by adjusting the x-axis range. A few cycles of the voltage and current signals of one glides near the ignition point is presented in 4.6 (a). Although the signals are quite noisy, it can be seen that when examining the voltage plot in blue, a general repeating behavior can be seen; a spike followed by a drop and then a smaller spike. This behavior is consistent with that of AC driven arcs whose behavior can be seen in Figure 4.7. This behavior is again seen in sub-figures (b) and (c) with the two peaks moving closer together as we move further along the electrodes (i.e., more time elapsing). This behavior seems to change in the last two sub-figures with the voltage plots looking more like simple

sinusoidal signals. This behavior is more consistent with that of an AC driven glow discharge. In fact, this behavior remains consistent in all other slices taken within the range of data corresponding to the straight edged of the electrodes. Thus, we can show how the straight edge of the electrodes which keeps the discharge at the maximum possible length for an extended period of time could potentially increase the time the discharge remains in the "cold" plasma region or the NTP region.

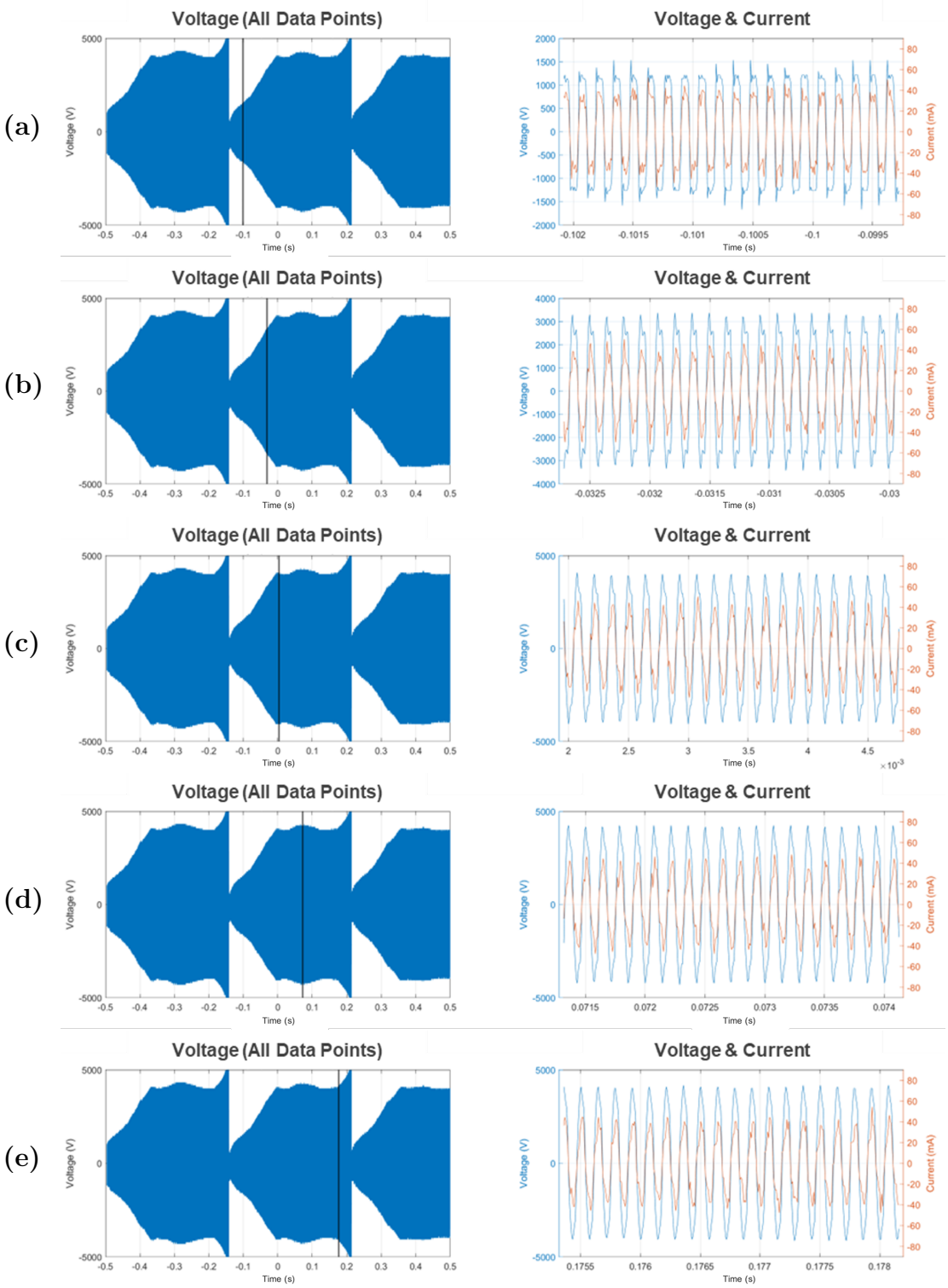

Figure. 4.6: A view of a few AC cycles of the voltage and current plots as a function of time for a sample run with dry air. The right side of each of the figures shows the location of the viewed cycles on the full range of the recorded data. The different sub-figures shown are taken sequentially from the ignition to the termination of the discharge with (a) being at or near ignition, and (e) being at or near termination.

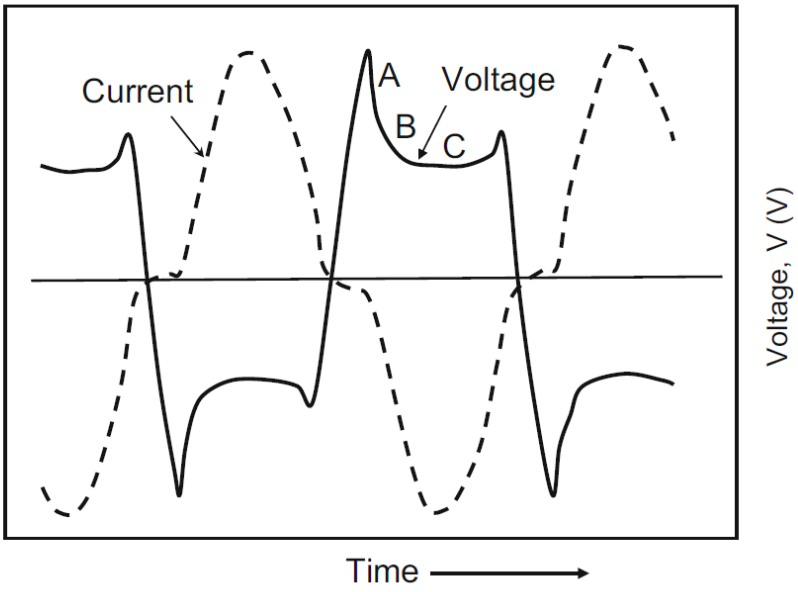

Figure. 4.7: A typical voltage over time plot for an AC arc showing how the voltage peaks at the beginning of each half cycle followed by a dip and a second smaller peak before the next half cycle. [76]

All the data processing and figures of the recorded data presented thus far have been done using a computer script written with MATLAB. This same code was also used to analyse the data from the four runs with nitrogen. Only a sample will be shown below.

Again, looking at the slices taken along the voltage and current waveforms for one complete glide, the same trend where the discharge starts out behaving as an arc and gradually changes to a glow discharge was observed. This behavior aligns with the literature and follows the transition presented in Figure 2.12. Figure 4.8 below shows the sequential slices taken as well as a few AC cycles of the voltage and current signals at the respective locations. Examining the last sub-figure taken closest to the termination point, we can see that the discharge terminates just as the voltage

signal starts behaving as a sinusoidal signal. Thus, we can say that it terminates as it transitions to the glow discharge NTP state, which is more ideal for gas conversion as was discussed in the literature review. This is unlike the air discharge which takes full advantage and displays the benefits of the electrode Design 3 with the straight edge. This with the drawback of a reduction in re-strike frequency leading to more gas passing through the reactor untreated between every two consecutive glides. In later sections, this drawback will be further discussed with potential solutions offered. Nevertheless, the lower re-strike frequency offers another advantage over higher frequencies: it allows for treating the gas for a longer period of time. This can itself be beneficial for gas conversion or it can enable the excited species to interact with a larger area of a potential catalyst layer.

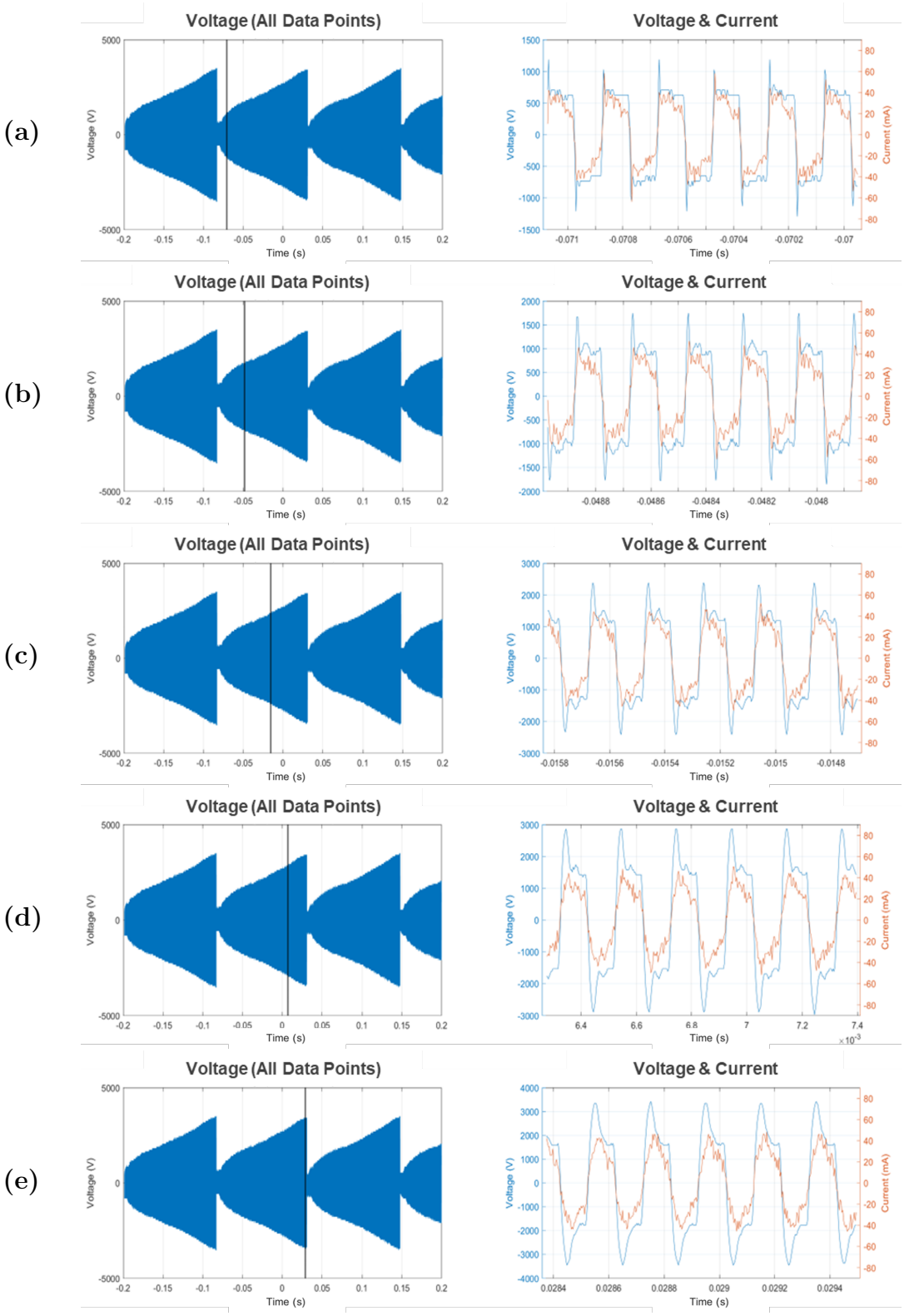

Figure. 4.8: A view of a few AC cycles of the voltage and current plots as a function of time for Run 1 with nitrogen gas. The right side of each of the figures shows the location of the viewed cycles on the full range of the recorded data. The different sub-figures shown are taken sequentially from the ignition to the termination of the discharge with (a) being at or near ignition, and (e) being at or near termination.

Another method to determine if the PGD reactor operates in the region most suitable for the chemical gas conversion of N_2 and CO_2 is to obtain an estimate of the reduced electric field along the reactor. Using the electric data recorded and presented in this chapter and some data obtained from the CFD model discussed in the next chapter, a plot of the reduced electric field along the electrode edge was generated and can be seen in Figure 4.9 below. The plot shows that the average reduced electric field along the electrode length is always within the optimal range between 5 and 100 Td.

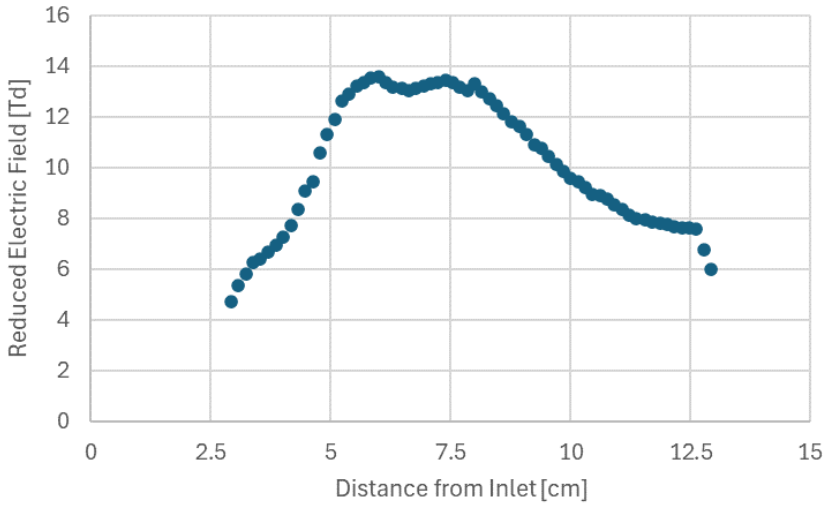

Figure. 4.9: The reduced electric field values at 100 different intervals along the length of the PGD reactor from the igniting point (2.9 cm) to the termination point (12.9 cm) with N_2 at 2.5 SLPM during run 1. The plot shows how for most of the glide, the approximate reduced electric field is within the range ideal for dissociation through vibrational excitation.

Using the recorded current and voltage signals, the instantaneous discharge power can be calculated at each point in time over the same range using Equation 4.1. This discretized power data was then plotted as a function of time and shown in Figure 4.10.

$$P = IV \tag{4.1}$$

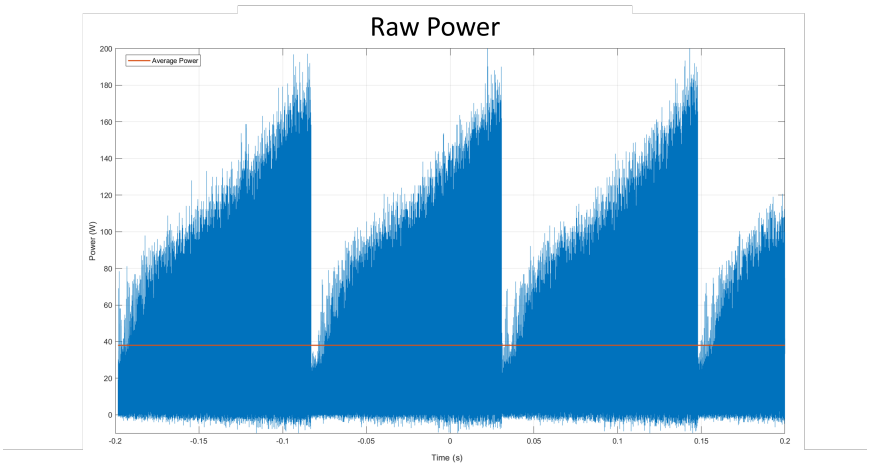

Figure. 4.10: Plot of the calculated raw power as a function of time for the run 1 with N_2. The orange horizontal line shows the the average power level at around 39 W.

The orange horizontal line represents the average power at around 39 W. However, the signal appears to be very noisy making any assessment on the peak power consumption difficult. Therefore, a Butterworth band pass filter was applied to filter out some of the noise. A Fast Fourier Transform (FFT) was produced for the data before and after filtering. Figure 4.11 shows both the FFTs before and after applying the filter to the current data collected from Run 1 with N_2. On both FFTs, there are three visible peaks. The first, and the most significant, is the peak at 5 kHz. The second and third represent the odd harmonics of the signal at 15 kHz and 25 kHz skipping over 10 kHz and 20 kHz. This is simply due to either the electrical signal generation or amplification processes as suggested by the literature [68]. When comparing both plots, it can be seen that the same three peaks remain relatively

unchanged in terms of amplitude after filtering. Thus, we can safely assume that the important features of the data remain unaffected. Moreover, when designing the filter, care was taken to ensure the cut-off frequencies were far enough from the signal of the voltage applied to the reactor.

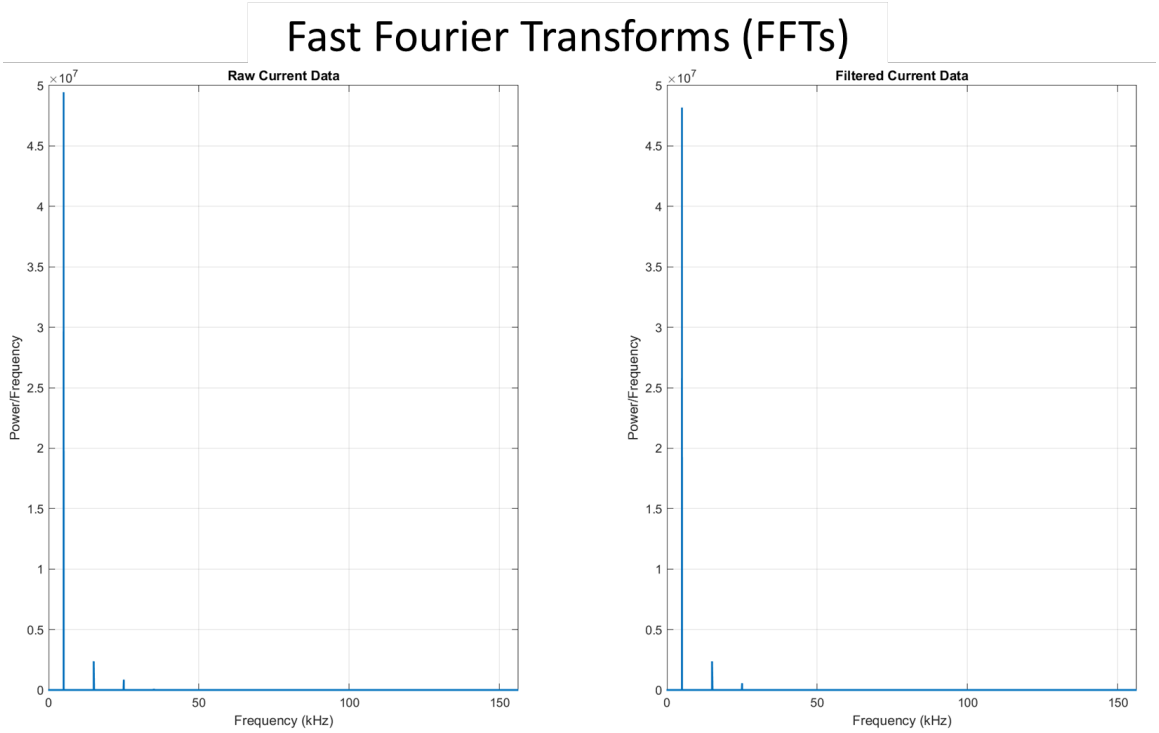

Figure. 4.11: FFT plots for the current data before and after a filter is applied. The peak at 5 kHz and its odd harmonics (15 kHz and 25 kHz) are almost unaffected by the filter.

Figure 4.12 below shows the power as a function of time from Figure 4.10 but after the filter was applied. The plotted data is a lot more clear at this point while leaving the average power relatively unchanged at around 39 W. We can now also see that the power peaks at around 135 W. These values, more precisely, the average power will be useful in the next section for the CFD model. It could provide us with

vital information about the power input into the plasma. However, care must be taken into consideration since not all this power goes to the plasma for conversion reactions. Some of the power is consumed by the electrodes or is lost as light gets emitted from the plasma.

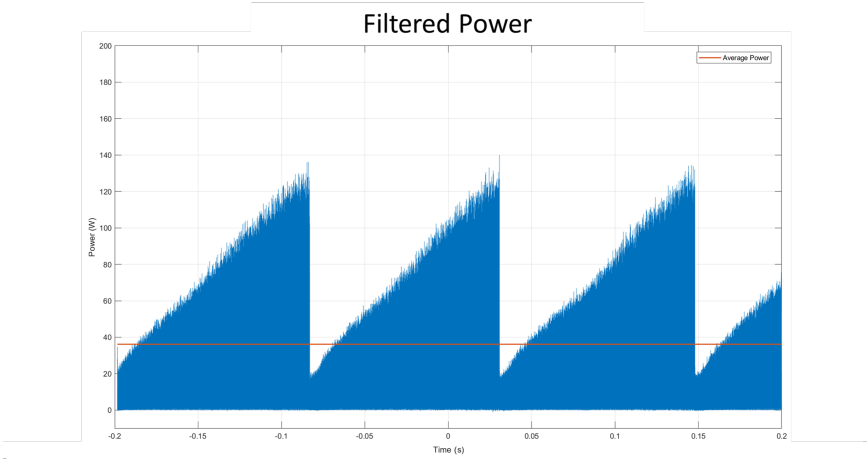

Figure. 4.12: Plot of the calculated filtered power as a function of time for the first run with N_2. The horizontal line shows the the average power level remains unchanged at around 39 W.

Table 4.2: Summary of the important findings extracted from the included recorded electrical data for all the runs with N_2. Peak voltage, current, and power obtained from the filtered data sets are reported. The table also reports the average power for each of the runs vital for the next step.

	Run 1	Run 2	Run 3	Run 4
Peak Voltage [kV]	3.67	3.90	3.70	3.62
Peak Current [mA]	54.56	49.96	49.64	49.33
Peak Power [W]	140.11	146.36	136.63	132.97
Average Power [W]	38.43	39.62	39.93	40.27

Chapter 5

Thermal and CFD Analysis

While it is easy to measure and record the voltage and current across the PGD reactor during operation without any disruptions, flow data and other physical quantities are harder to collect reliably without disruptions. However, for the purposes of characterization, obtaining more information about flow and internal temperature distributions will be useful. Thus, there arises a need to measure and record flow and temperature data for use to validate a CFD and heat transfer model. Using the CFD and heat transfer models, we can assess fine temperature and flow data that enhance our ability to optimize the design and operation of the PGD reactor. Such a model was developed using ANSYS Fluent. The meshing process, assumptions, and boundary conditions will be presented in the coming sections. Next, the results will be represented visually and discussed with the help of distributions, vectors, and streamlines. Finally, some of the data is corroborated using real life temperature distributions captured using the FLIR camera discussed in Section 3.5.

5.1 Computational Fluid Dynamics (CFD) Analysis

In Chapter 2, an ideal temperature for the catalysts impregnated BNNT sheet was discussed and found to be 300 °C at the minimum. Therefore, figuring out the BNNT sheet temperature at different locations inside the PGD reactor could be useful. To measure the actual temperature profile of the catalyst sheet through the quartz plates, the FLIR A6260 camera is a good option since it allows for temperature measurements through the quartz plate. However, since the lower bound of the temperature range on the A6260 camera is 400 °C, it is not be ideal for this task. Thus, a different method of measuring or estimating the temperature or temperature distribution of the catalyst sheet is needed. This is where the CFD model comes in handy allowing us to obtain estimates of BNNT sheet temperatures inside the reactor. The model will also provide us with valuable insight about the flow inside the reactor. However, setting up the model properly is vital in order to achieve or produce reliable data. In this subsection, the mesh generation and optimization, boundary conditions, cell zone conditions, materials, and assumptions will be clearly defined.

5.1.1 Mesh Generation and Optimization

After a geometric model of the PGD reactor was created to scale on Fusion 360, it was exported as an stl file which can be imported into the geometry component in ANSYS. This component of the ANSYS simulation project can be seen on the far left of Figure 5.1. The figure itself shows all the components needed to run the CFD analysis or the Project Schematic.

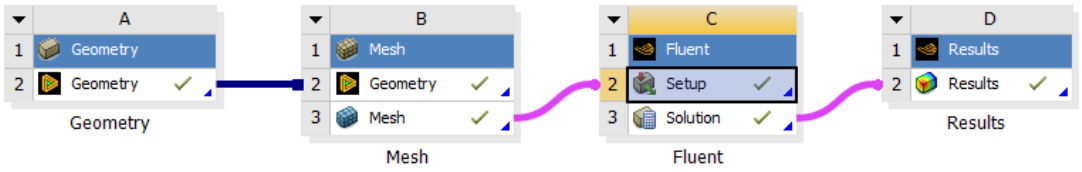

Figure. 5.1: The ANSYS final project schematic for the simulation. The schematic shows the sequence of ANSYS components needed to import the CAD design, generate the mesh, find the solution using Fluent, and finally represent the results visually.

As can be seen from the Project Schematic, after importing the model into ANSYS, it is then transferred to the meshing component where the model is divided into small elements or cells. As previously discussed, the smaller the elements the better the chances that the solution will converge and that better results will be obtained. However, the Educational ANSYS licence being used has a limit of 512,000 on the number of elements that could be processed. To achieve the best results possible without surpassing the set limit, a non-uniform mesh was used. This means that bodies or faces where more accuracy is needed will be comprised of a higher number of cells as compared with low priority or low complexity bodies and faces. Moreover, because of the symmetric nature of the PGD design, only half of the geometry needs to be simulated, and it is then simply reflected about the symmetry plane in post-processing. Table 5.1 below summarizes the important variables necessary to create or replicate the mesh.

Table 5.1: A summary of the options used when defining the mesh of the CAD design to be imported into Fluent. These meshing options are applied to the entire model.

Meshing Options	
Physics Preference	CFD
Solver Preference	Fluent
Element Size [m]	4.0×10^{-3}
Adaptive Sizing	No
Growth Rate	1.9
Maximum Size [m]	5.0×10^{-2}

A Body Sizing mesh was also applied to the fluid "bodies" in the model in order to achieve a finer mesh. This was done to ensure accurate flow results due to the higher degree of complexity. Table 5.2 summarizes the important variables applied to the Body Sizing mesh.

Table 5.2: A summary of the options used when defining the body sizing mesh of the fluid bodies in the CAD design. These options allow for a finer mesh in the fluid bodies due to the higher degree of complexity and to obtain accurate results.

Body Sizing Options	
Element Size [m]	6.0×10^{-4}
Behazior	Hard
Capture Curvature	No
Capture Proximity	No

After applying the mesh and body sizing options detailed in the tables above, the meshing was done, and the quality and total number of cells were checked. The resulting mesh had a maximum skewness of around 0.93 which is lower than the maximum acceptable value of 0.95. Moreover, when examined further, it is seen that only a very small percentage of cells have skewness values in the 0.90s giving us a good mesh overall. It should be noted that arriving at the mesh options presented

was a trial and error process where different combinations of the above variables were applied at which point the quality of the mesh and total number of elements were assessed.

5.1.2 Fluent Set Up, Boundary Conditions, and Assumptions

Set Up

After meshing the geometric model successfully, the mesh is imported into ANSYS Fluent where the boundary conditions, cell zone conditions, materials, and calculation parameters have to be clearly defined. First, the Fluent component in ANSYS is launched, the screen in Figure 5.2 can be seen. This main window is where one can navigate to the different tabs in order to set up the simulation and define how the calculations will be carried out.

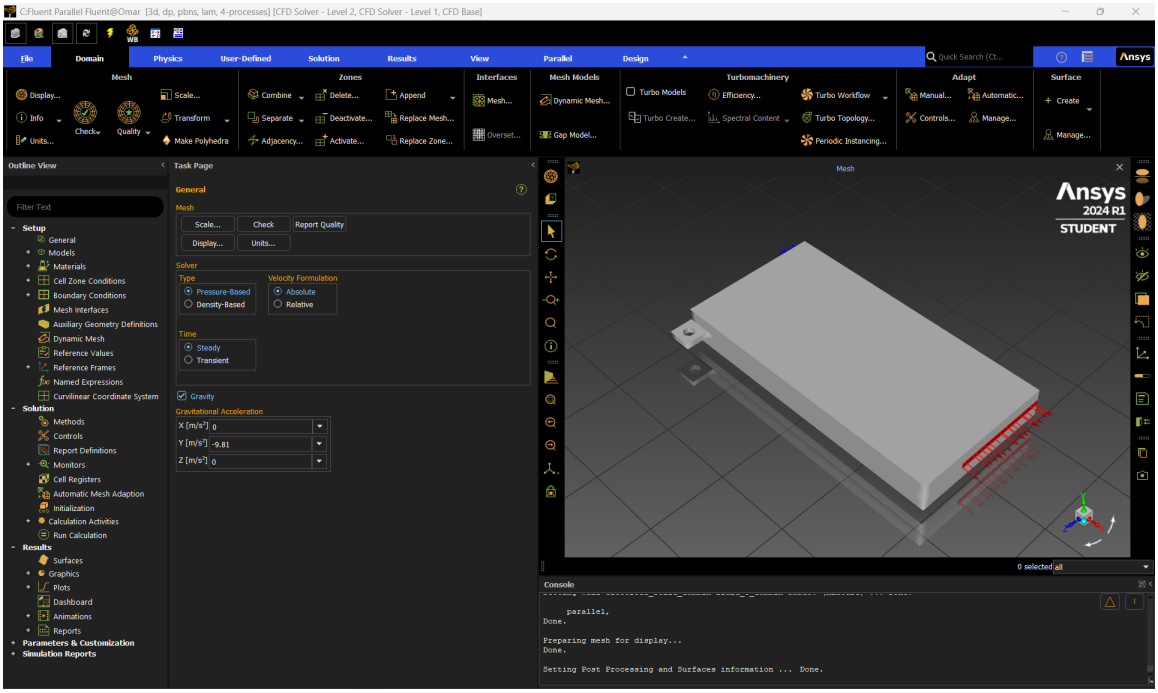

Figure. 5.2: Main window seen when the ANSYS Fluent component is launched. The window shows all the different tabs used for the set up, solution, and calculations.

First, in the General tab, the simulation is defined as pressure based and steady state with an absolute velocity formulation. The acceleration due to gravity is also set as 9.81 m/s^2 in the negative Y direction. The axis of the model can be seen at the bottom right corner of the model display in Figure 5.2. Next, the model tab is opened. The tab options can be seen in Figure 5.3. All the models should be kept off except the Energy model which is responsible for solving the energy equation in the solid and fluid domains. As for the Viscous model, the Reynolds number was calculated using Equation 2.9 for the different flow rates at different points along the flow of the gas in the PGD reactor. It was found that the Reynolds number never exceeds 2000, thus, the Laminar viscous model is used.

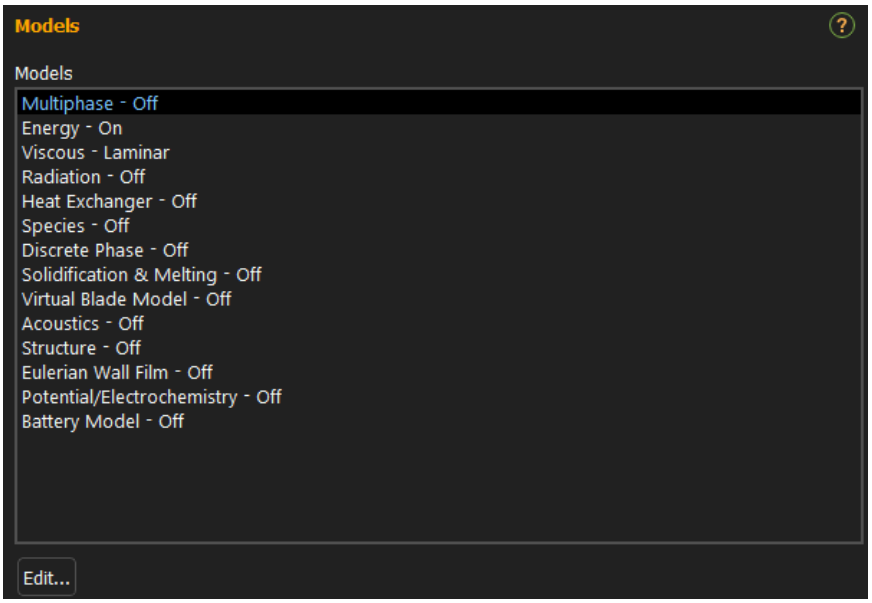

Figure. 5.3: Different solution models used in ANSYS Fluent. For this study, the viscous model is set to Laminar and the Energy model is turned on.

The next tab in the set up process allows the definition of the different materials in the model. In our model, there are four different solid materials and one fluid. The solid materials are brass for the electrodes, fused quartz for the glass, PTFE for the gaskets, and BNNT for the catalyst layer. While most of the solid materials were not found in the existing Fluent database and had to be created, nitrogen, the working fluid, was predefined in the database. Table 5.3 below summarizes the different material properties for the solid materials and working fluid in the simulation as well as the sources used to obtain the quantities.

Table 5.3: Summary of the different material properties used in the simulation. The table provides the destiny thermal conductivity, and specific heat for each of the bodies in the simulation. For the fluid body, the viscosity was also defined.

Material	Density ($\mathrm{kg\,m^{-3}}$)	Thermal Conductivity ($\mathrm{W\,m^{-1}\,^{\circ}C^{-1}}$)	Specific Heat (Cp) ($\mathrm{J\,kg^{-1}\,^{\circ}C}$)	Viscosity ($\mathrm{kg\,m^{-1}\,s^{-1}}$)	Sources
Fused Quartz	2200	1.4	670	-	[77]
Brass	8978	387.6	381	-	ANSYS Library
PTFE	2025	0.2630	1030	-	[78], [79]
BNNT	0.25	2.5	650	-	[80]–[82]
Nitrogen	1.138	0.0242	Piecewise Polynomial	1.66×10^{-5}	ANSYS Library

Next, three different fluid regions are defined. First, we have the region of nitrogen gas before the plasma is ignited. Next, we have the plasma fluid region between the point of ignition and termination. Finally, we have the nitrogen gas region after the plasma. These regions are identified using long exposure images and the MATLAB code. A long exposure image taken from directly overhead of the reactor is uploaded into MATLAB. A screenshot of the top view of the PGD reactor's top view is also uploaded. The code then prompts the user to pick out the four corners of the reactor on both the image and screenshot in a clockwise fashion. The image is then morphed to fit the CAD design screenshot. Finally, the ignition and termination points are selected on the morphed image to obtain the dimensions or the length of the plasma regions. These dimensions are then used to define the different fluid regions for the simulation. Figure 5.4 shows a sample of the what the three different fluid regions look like.

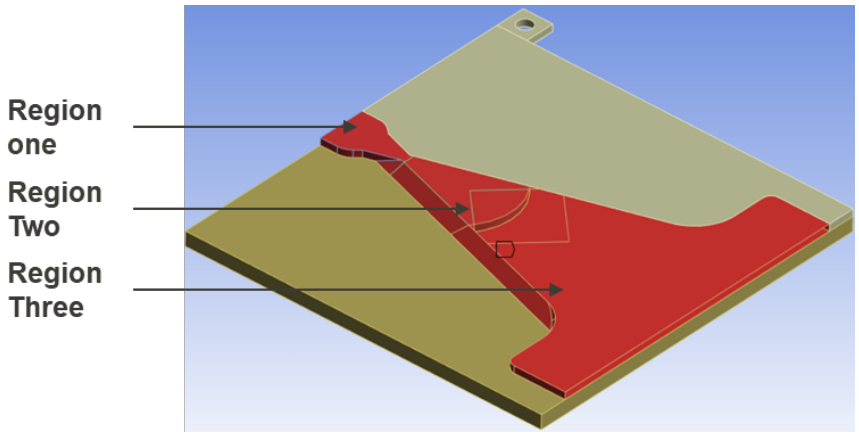

Figure. 5.4: Three different fluid regions or bodies in the simulation. Region one and three are simply deigned as nitrogen gas. Region two is defined as nitrogen gas with volumetric heat generation to simulate the plasma. This figure is only for illustrative purposes and shows the regions on Design 2. The simulation was carried out on the Design 3 geometry

For regions 1 and 3, nothing needs to be defined other than the working gas (nitrogen). However, for region three, a source term needs to be defined. This source term is an energy term that is applied to account for the energy that goes into the plasma to heat up the gas. This term is defined as a volumetric power generation. Initially, the average power value obtained at the end of the last chapter is used along with the volume of region 2 to obtain the volumetric power generation. However, as discussed previously, some of the power is lost as radiation. For the purposes of this set up, assuming 100% of the power consumed by the PGD reactor goes into the heating up the gas volume is acceptable. In later sections of this chapter, a better approximation of the volumetric power generation will be obtained and utilized.

Boundary Conditions

At this point, the boundary conditions are to be set in the appropriate tab. Table 5.4 summarizes the boundary conditions used for one of the runs.

Table 5.4: Summary of the boundary conditions set in Fluent to find the solution. The inlet velocity of 0.78 m/s corresponding to a flow rate of 2.5 SLPM to simulate Run 1

Boundary	Conditions
Velocity Inlet	V = 0.78 $\mathrm{m\,s^{-1}}$ T = 23 °C
Pressure Outlet	Zero Gauge Pressure
Fluid Walls	No Slip - Stationary Wall Thermally Coupled
Outside Walls	Free Convection Free Stream Temperature = 23 °C Top Wall h = 22 $\mathrm{W\,m^{-1}\,°C^2}$ Side Wall h = 7 $\mathrm{W\,m^{-1}\,°C^2}$ Bottom Wall h = 11 $\mathrm{W\,m^{-1}\,°C^2}$
Solid Interface Walls	0.159 cm Thick PTFE Condition Applied

The inlet is set as a velocity inlet with the appropriate velocities calculated using Equation 5.1 and the applied flow rates using the MFC.

$$Q = VA \tag{5.1}$$

where Q is the volumetric flow rate in $\mathrm{m^3/s}$, V is the inlet velocity in m/s and A is the cross-sectional area of the inlet in $\mathrm{m^2}$.

The outlet is set as a pressure outlet at zero gauge pressure. The fluid walls, shown in Figure 5.5, are defined as stationary walls with no slip and are thermally

coupled. The outside walls of the reactor shown in Figure 5.6 are set up to experience free convection with a free stream temperature of 23°C. The appropriate heat transfer coefficients are shown in the table above. These numbers are calculated using the Equations 5.2, 5.3, 5.4, and 5.5 solved sequentially.

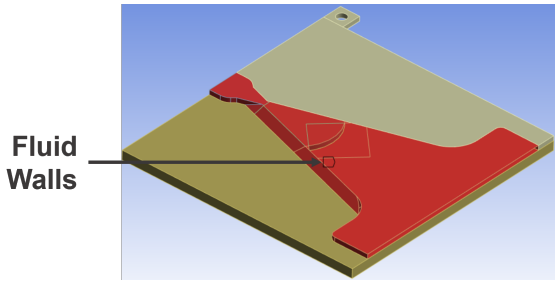

Figure. 5.5: Fluid walls encompassing the three different fluid regions. The walls are set as stationary walls with no slip and are thermally coupled.

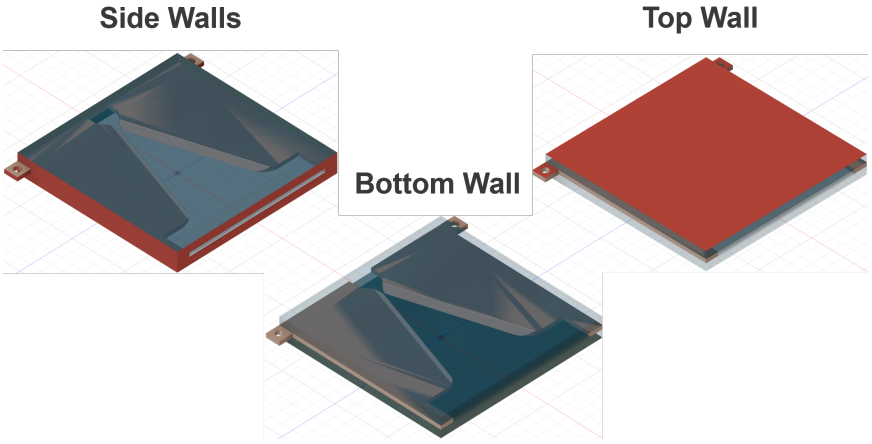

Figure. 5.6: Outside top, bottom, and side walls of the reactor set to experience natural convection with coefficients of 22, 11, and 7 W/m.°C, respectively. The figure shows Design 2 but is only for illustrative purposes.

$$Ra = \frac{g\beta(T_s - T_\infty)L^3}{\nu\alpha} \tag{5.2}$$

where Ra is the dimensionless Rayleigh number, g is the acceleration due to gravity, β is the coefficient of thermal expansion, T_s is the surface temperature, T_∞ is the ambient temperature, L is the characteristic length, ν is the kinematic viscosity, and α is thermal diffusivity.

$$Pr = \frac{\nu}{\alpha} \tag{5.3}$$

where Pr is the dimensionless Prandtl number.

$$Nu = 0.68 + \frac{0.67Ra^{1/4}}{[1 + (0.492/Pr)^{9/16}]^{4/9}} \tag{5.4}$$

where Nu is the dimensionless Nusselt number.

$$h = \frac{Nu \cdot k}{L} \tag{5.5}$$

finally, Nu is used to calculate the free convection coefficient (h) where k is the thermal conductivity of the fluid.

Assumptions

Aside from the assumptions built into the CFD software itself, a few additional assumptions and simplifications were made for the set up. The system is said to have reached steady-state for both the CFD simulation and actual runs. The flow is assumed to be laminar and the gases ideal. The ambient temperature and pressure are assumed to be constant at 23 °C and 101.325 kPa, respectively. The material properties listed in Table 5.3 are constant and not temperature dependent. However,

the heat capacity of nitrogen is an exception and is assumed to be a function of temperature and is given by a piece-wise polynomial. This is because the nitrogen gas is expected to see a large temperature change as compared with other components in the model. Finally, due to the presence of a thermal insulator (PTFE) at solid interfaces, the contact resistance is assumed to be negligible.

As for the plasma region, it is assumed to be a region of uniform heat generation between the discharge ignition and extinction points, as communicated previously. This assumption holds due to the high frequency with which the discharge glides (re-strike frequency). A more accurate representation is not required for the purposes of this thesis and cannot be achieved using ANSYS. A more dedicated software to conduct the complex analysis. The radiation effects from the plasma are assumed to be negligible. Thus, the radiation option in Fluent is kept off. However, since the plasma clearly emits a substantial amount of radiation, this was factored in and will be shown later in this chapter. This is because the actual discharge volume gets much hotter than the bulk gas temperature obtained by applying volumetric heat generation to the plasma region in the model. Therefore, simply turning on the radiation option in Fluent is not accurate.

5.2 IR Imaging and Temperature contours

In section 3.5, it was seen that the FLIR A500 camera was more suitable for capturing 2D temperature distribution of the reactor during operation. In this section, the set up process for the camera and results obtained are presented and discussed.

One of the most important steps of the set up process was to define the appropriate emissivity value for the top quartz plate. Initially, the emissivity value was obtained from literature and found to be around 0.93 [75]. However, this value was provided for the quartz at 20°C. Thus, a more accurate value was sought. To arrive at the more accurate figure, a test was conducted using the FLIR camera and three thermocouples. First, the three thermocouples were attached to different points on the top quartz plate surface using some thermal grease to reduce contact resistance. Next, the camera was mounted directly above the reactor with a clear view of the top quartz plate surface and the thermocouple contact points. The reactor was then initialized and operated until the temperatures stabilized to a steady state. Finally, the FLIR camera was used to measure the temperature at the three thermocouple contact points using the initial emissivity value. These values are compared with the corresponding thermocouple readings and the emissivity adjusted until the FLIR camera and thermocouple readings were in agreement. Table 5.5 below shows the FLIR camera temperature readings for the first point at each emissivity interval compared with the thermocouple readings.

Table 5.5: The FLIR camera temperature reading at point one compared to the thermocouple readings as the emissivity is iteratively adjusted. The percentage difference slowly decreases as the emissivity was adjusted.

Emissivity	FLIR [°C]	Thermocouple [°C]	Percentage Difference [%]
0.93	100.76	96.34	4.5
0.95	98.40	96.12	2.3
0.98	96.10	95.94	0.4

The table shows how as the emissivity value is adjusted from 0.93 to 0.95 and then 0.98, the temperature values get closer with the percentage difference dropping.

This same trend can be seen for the second and the third points whose data can be found in Tables A.1 and A.2.

After obtaining a better estimate for the emissivity, the FLIR camera was then used to capture 2D temperature distributions of the top quartz plate surface for all the runs. Using these distributions, the maximum temperature and mean temperature of the surface were obtained for each run. The collected data can be seen below in Table 5.7.

Table 5.6: FLIR camera reading of the maximum, minimum and mean temperature of the top quartz plate surface after for each of the runs after reaching steady-state.

Run	Flow Rate [SLPM]	Maximum [°C]	Minimum [°C]	Mean [°C]
1	2.5	95.01	23.50	41.27
2	3.5	94.44	24.32	41.18
3	4.5	91.25	24.66	41.61
4	5.0	88.29	24.95	42.00

It can be seen that as the flow rate increases, the maximum temperature recorded decreases, the minimum temperature increases, and the mean temperature remains relatively constant. A better understanding of these results could be obtained by examining the actual images captured by the FLIR camera. These can be seen in Figure 5.7.

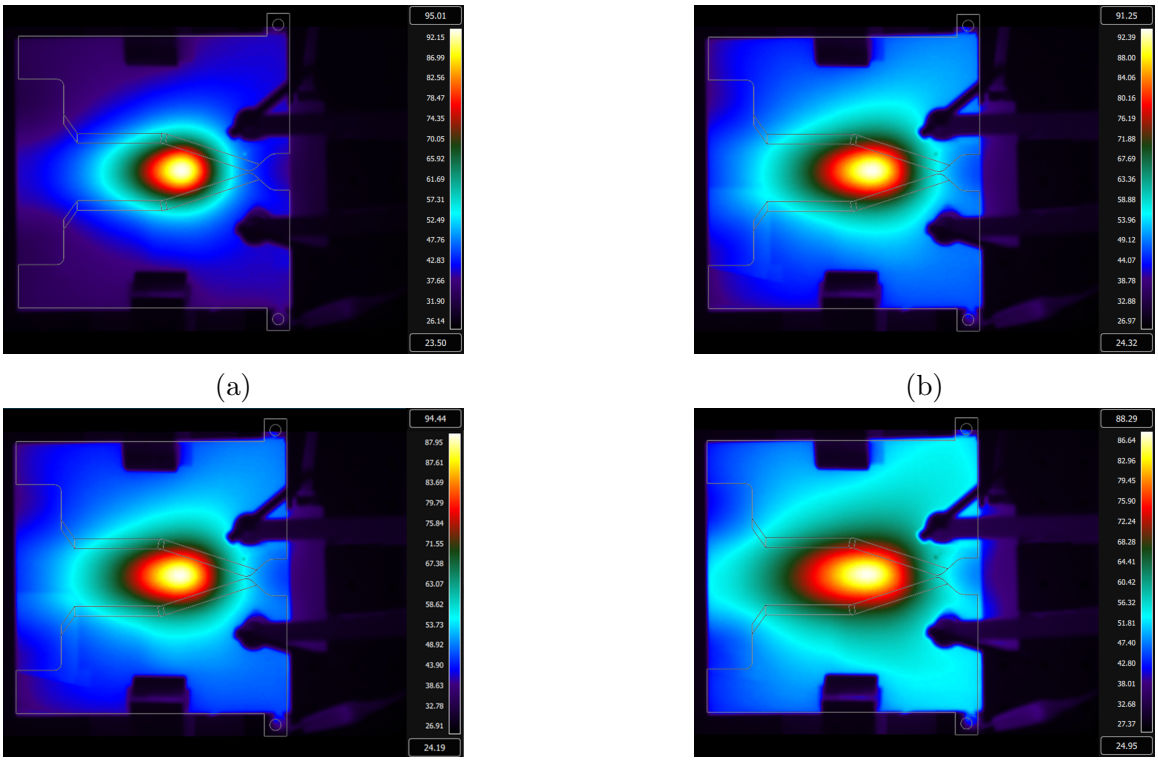

Figure. 5.7: FLIR camera temperature profiles of the top quartz plate surface for each of the runs. At the top right corner, the maximum temperature can be seen. (a) Run one at 2.5 SLPM. (b) Run two at 3.5 SLPM. (c) Run three at 4.5 SLPM. (d) Run four at 5.0 SLPM

Looking at the sub-figures in Figure 5.7, it can be seen that as the flow rate increases, the temperature profile is increasingly stretched. This is simply due to the faster rate of fluid flow inside the reactor. This causes a reduction in the maximum temperature and an increase in minimum temperature as the heat is more spatially dispersed by the faster moving fluid flow. However, since the power input into the plasma remains the same regardless of the flow rate, the mean temperature remains relatively constant.

- It should be noted that these distributions and data were only recorded after the reactor has reached steady state. This was determined by plotting the maximum temperature of the top quartz plate surface against time and allowing it to flatten out. An example of such a plot can be seen below in Figure 5.8.

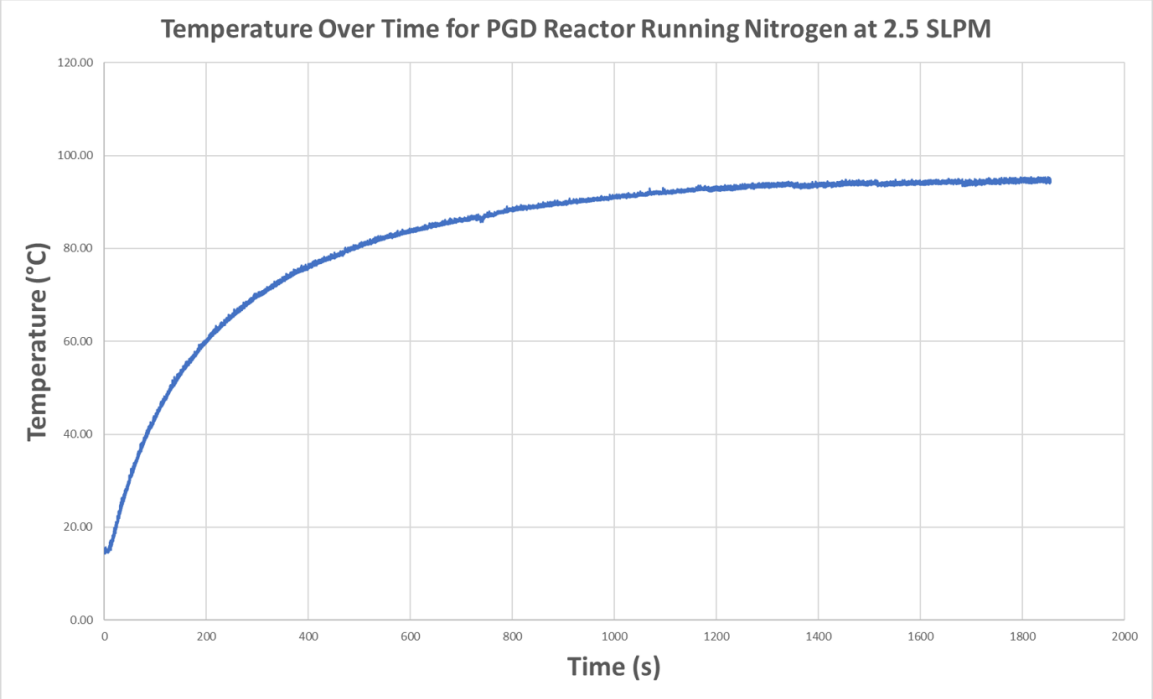

Figure. 5.8: FLIR camera measured maximum temperature of the top quartz plate surface as 2.5 SLPM as a function of time. The temperature reaches a maximum and plateaus around 95°C.

The distribution and recorded data from the FLIR camera presented in this section will be used in the next section to corroborate the CFD model developed.

5.3 Analysis and Discussion of the Temperature Data

A significant percentage of the power consumed by the PGD reactor is emitted as radiation. Using trail and error, an estimate of the percentage loss was found to be around 35%. This figure was achieved by using the average power calculated from the electrical data to calculate the volumetric heat generation if 100% of the power goes into heating the volume. The simulation was then ran and the maximum, minimum, and mean temperatures of the simulated top quartz plate surface are compared with the experimental data obtained using the FLIR camera. The percentage was then incrementally dropped until a close match was achieved at around 65% of the power. Figure 5.9 shows an example of the temperature distribution of the simulated top quartz plate surface.

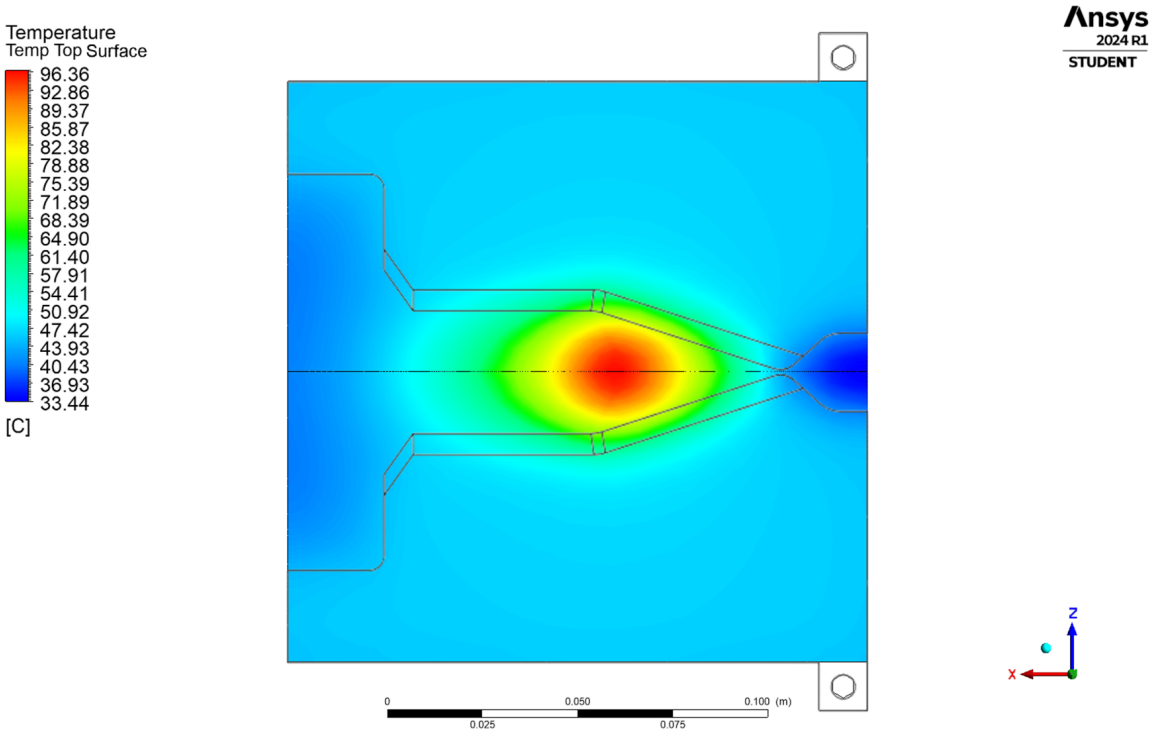

Figure. 5.9: Temperature distribution of the simulated top quartz plate surface of the reactor. A hot spot forms with a maximum temperature of around 96°C.

Table 5.7 below compares the simulated maximum temperatures with the corresponding experimental values.

Table 5.7: The FLIR camera maximum temperature reading for each run compared with the values obtained from the ANSYS Fluent simulation.

Run	Simulated [°C]	Experimental [°C]	Percentage Error [%]
1	96.36	95.01	1.42
2	93.24	94.44	1.27
3	90.12	91.25	1.24
4	87.79	88.29	0.57

At this point, we could use the simulation to obtain more information about the flow and conditions inside the PGD reactor. One of the most important pieces of

information has to do with the temperature of the BNNT catalyst layer. Previously, it was discussed how a temperature of at least 300 °C was necessary for catalytic activation. Figure 5.10 shows the simulated temperature of a BNNT catalyst layer covering the entire bottom of the inside of the PGD reactor.

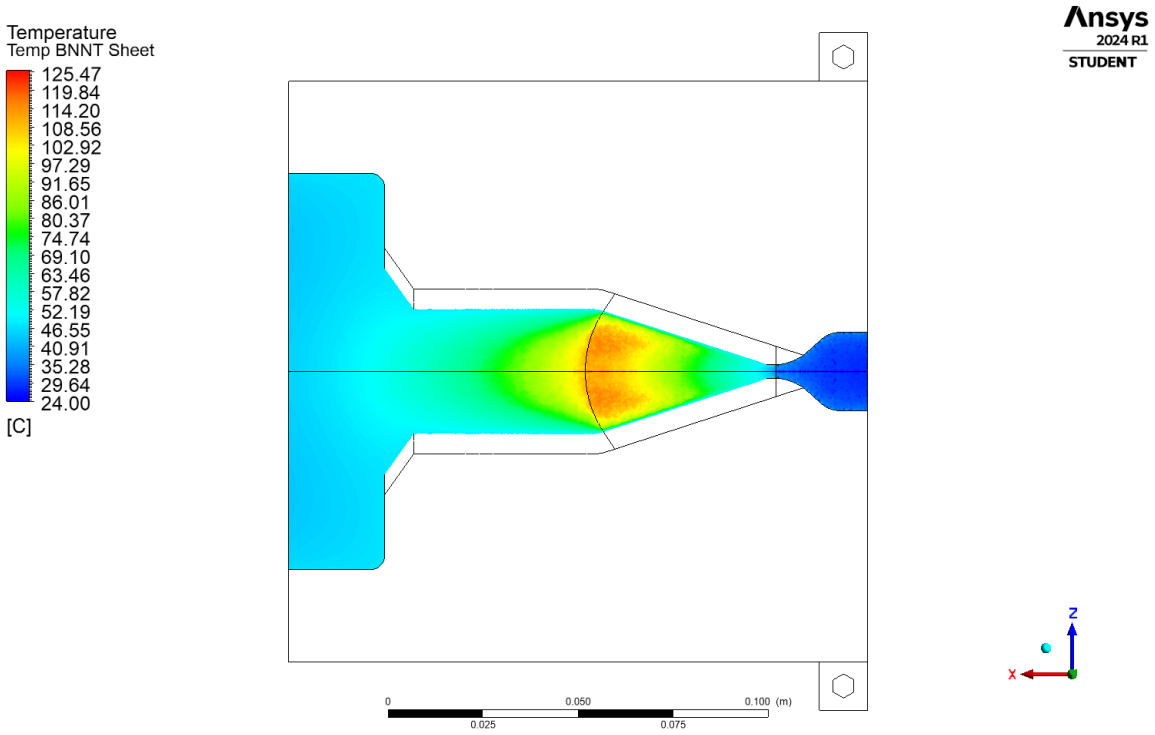

Figure. 5.10: Temperature distribution of the simulated BNNT catalyst areas on the bottom plate of the reactor. The hottest parts can be seen to have temperatures of around 125 °C falling short of the 300 °C requirement.

It can be seen that the temperature reaches a maximum of around 126 °C some distance from the shortest gap. Thus, we are short of the required activation temperature. A simple fix is to input more power into the PGD reactor. However, one key point to consider is that, for our PGD reactor, quartz plate were used with the absences of thermal insulation in order to allow for visual observation of the plasma.

In a real world application, the reactor will be insulated to allow for maximum retention of thermal energy. Thus, it will likely reach much higher temperatures at steady state. To test this theory and simulate a situation with thermal insulation, the simulation was repeated with surfaces experiencing free convective cooling on the outside of the reactor (Fig. 5.6), set to have half of their respective heat transfer coefficients from Table 5.4. The resulting BNNT catalyst layer temperature distribution can be seen in Figure 5.11.

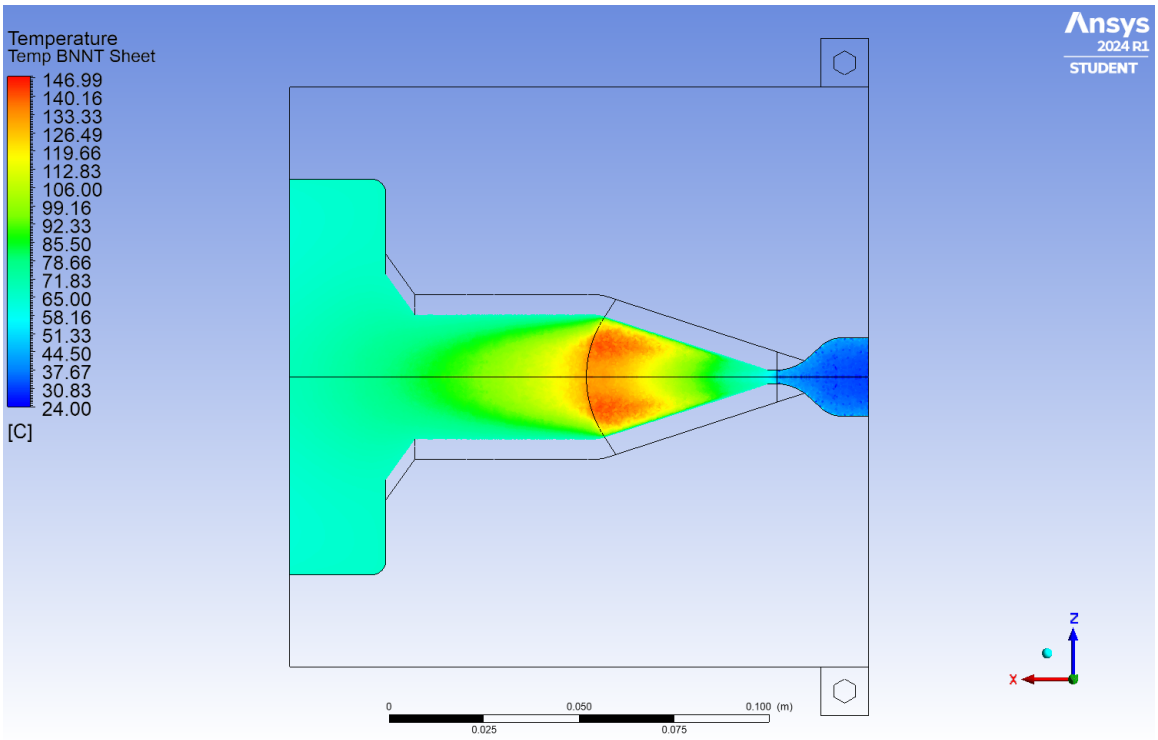

Figure. 5.11: Temperature distribution of the simulated BNNT catalyst layer on the bottom plate of the reactor with half of the heat transfer coefficient values (h/2). The hottest areas can be seen to have temperatures of around 147 °C still falling short of the 300 °C requirement.

One can observe that even with half the heat transfer coefficients, the BNNT catalyst layer's maximum temperature does not reach the required activation tem-

perature. Finally, we tested the extreme case where the PGD reactor is completely insulated and only allowing the heat to get dissipated by the action of the gas flow inside the reactor. The resulting BNNT catalyst layer maximum temperature can be seen in Figure 5.12.

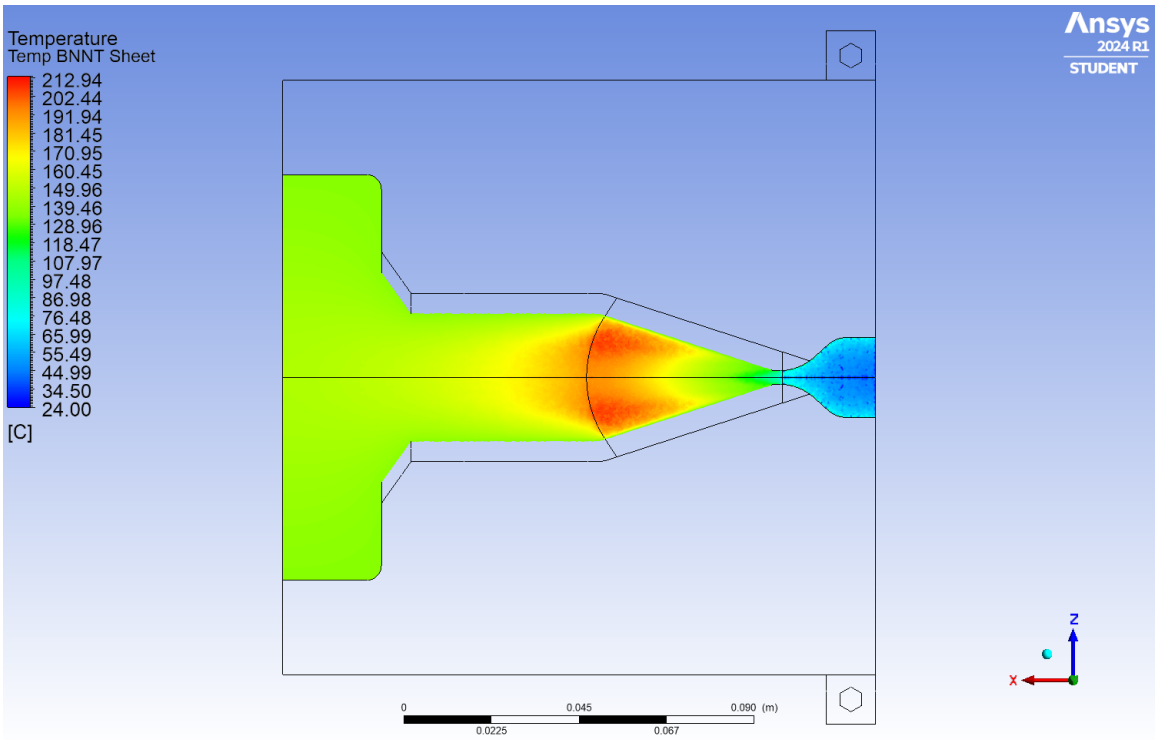

Figure. 5.12: Temperature distribution of the simulated BNNT catalyst layer on the bottom plate of the reactor with no convection on the top and bottom (h = 0). The hottest areas can be seen to have temperatures of around 212 °C, again, still falling short of the required temperature.

Even in this case where the heat is only dissipated through the flowing N_2 gas inside the reactor, the catalyst layer only reached a maximum temperature of 212 °C. This is still short of the required activation temperature of 300 °C. Therefore, we can conclude that the current power input of around 39 W is not sufficient to allow the BNNT catalyst layer to reach the activation temperature. Using trial and error, the

power value at which the BNNT sheet finally achieves the required temperature was obtained. A volumetric heat generation value of around 1.9×10^{7} W/m^3 was input into Fluent, resulting in the distribution shown in Figure 5.13. Using the volume of the plasma region obtained from the geometry (1.75×10^{-6} m^3), the power in the plasma was calculated to be around 33 W. However, if we assume that this only represents 65% of the electrical energy input, then the required electrical energy input for the BNNT sheet to reach the desired temperature is around 51 W.

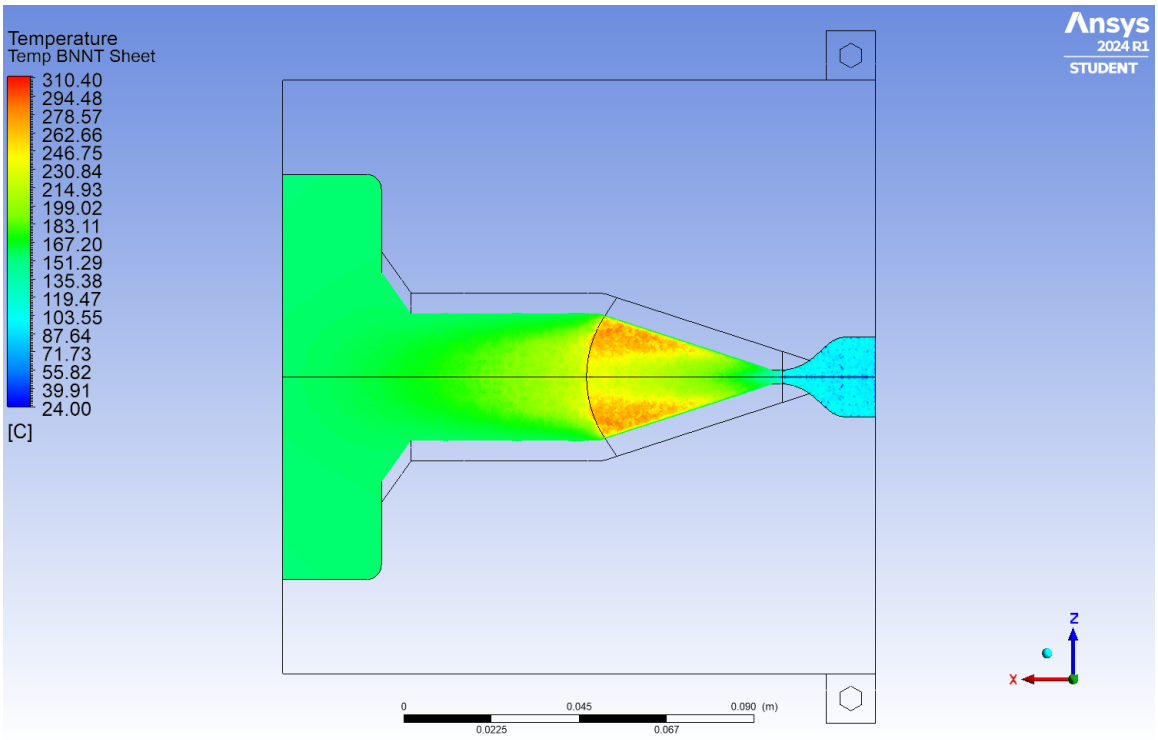

Figure. 5.13: Temperature distribution of the simulated BNNT catalyst layer on the bottom plate of the reactor with a volumetric heat generation value of 19000000 W/m^3 and h/2. Some areas of the layer have reached the required temperature. However these areas with temperatures greater than 300 °C are limited affecting the performance of the reactor.

Looking at the figure above, one can see that the BNNT sheet only reaches 300 °C or more in a limited area while in most other areas, the temperature is in the 100s. This makes it economically wise to only place the catalyst layers in those areas. However, this significantly limits the PGD reactor and does not allow it to take full advantage of Design 3 with the expanded NTP region. An alternative would be to increase the power further to allow more of the BNNT catalyst layer to reach the desired temperature.

Next, we had a look at the velocity vector of the flow at a horizontal slice directly at the center of the PGD reactor which can be seen in Figure 5.14.

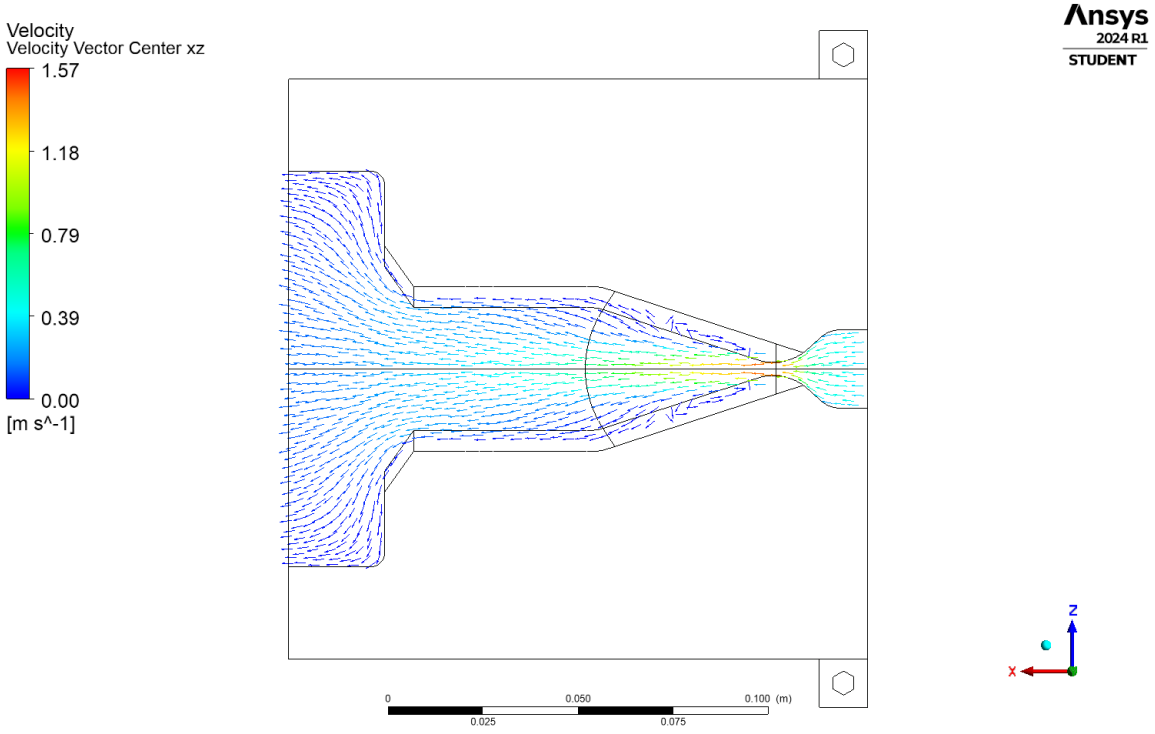

Figure. 5.14: A visual representation of the flow inside the reactor using velocity vectors. The vectors shown are of the flow at a horizontal layer in the middle of the flow. Vortices can be seen on either side of the main flow down the center.

In the figure above, it can be seen that most of the flow is down the middle of the reactor. However, two vortices are observed to either side of the main flow right after is passes the shortest gap. These are called recirculation cells caused by the separation of the flow due to the divergence of the electrodes beyond a critical value. Thus, a smaller angle could eliminate the vortices if they are deemed not desirable. However, looking at the magnitude of the velocity of the vortices we can see that they are very small. Thus, they are unlikely to have any effect and may not result in sufficient mixing of the reactive species inside the reactor. However, more or stronger vortices could possibly be induced. Another thing to note is that there is very limited flow in the areas where the BNNT catalyst layer reached the desired temperature. This further shows how more power is required to heat up the catalyst layer in the regions where more of the gases flow.

To better visualize the vortices, a streamline representing simulated paths that gas particles follow as they move through the reactor. The generated streamline can be seen in Figure 5.15.

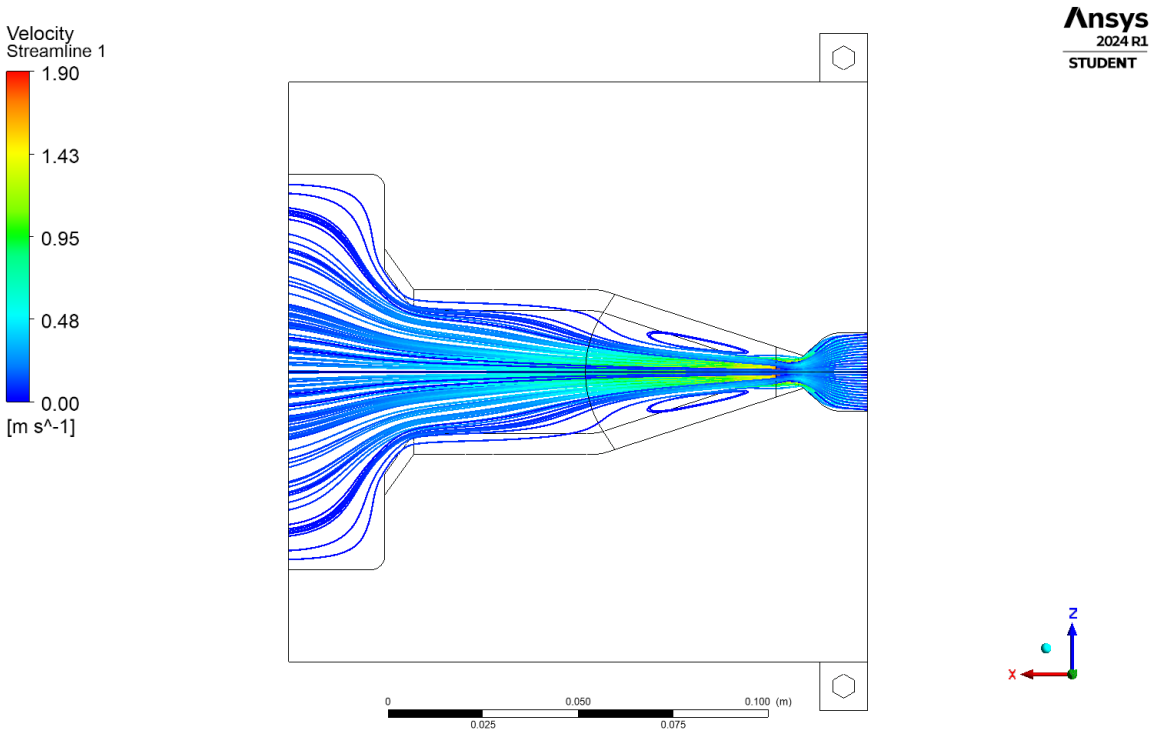

Figure. 5.15: A visual representation of the paths of N_2 particles moving through the reactor at a flow rate of 2.5 SLPM. The streamlines illustrate the flow direction, pattern, and speed, and also highlight vortices, such as those observed on both sides of the main flow.

Chapter 6

Conclusion and Future Works

6.1 Conclusions

This work aimed to further study the use of NTPs for gas conversion of waste products such as CO_2 and N_2 from the atmosphere to produce carbon-neutral or zero-carbon fuels. Throughout this thesis, various methods of producing and sustaining NTPs were examined, with planar gliding discharge reactors showing great potential for this purpose. A PGD reactor was designed and tested with N_2 gas and compressed air, yielding valuable electrical and thermal data. These findings pave the way for future work to develop this reactor into a viable option for producing zero-carbon and carbon-neutral fuels, aiding the electrification efforts for heavy industrial processes.

The first objective was to design and build a PGD reactor to characterize the discharge. The reactor needed to generate a stable and repetitive discharge, be easily assembled and disassembled, and allow for a catalyst layer to be introduced inside. The reactor design was meticulously documented through an iterative process to

meet these objectives and additional design constraints. Using quartz plates as the reactor walls allowed for visual observation to ensure a stable and repetitive discharge. The layered design, assembled with clamps and no binding agents, facilitated easy assembly and disassembly, allowing for future catalyst layer introduction.

The second objective was to optimize the PGD reactor design. In a PGD reactor, the discharge transitions from a thermal discharge to a non-thermal discharge as it lengthens and cools. The NTP region can be more efficient for gas conversion applications due to the cooler temperatures while maintaining the reactive environment. The electrode design was iteratively improved over three different iterations to maximize the NTP region compared to the TP region by straightening out the inner electrode edge or keeping the gap constant at the end of the discharge. This, however, resulted in lower re-strike frequencies and more gas passing untreated between consecutive glides. For Design 2, each glide took about $110.94\,\mathrm{ms} \pm 1.53\%$, while for Design 3, each glide took around $194.79\,\mathrm{ms} \pm 1.5\%$, representing a percentage increase of around $75.58\,\% \pm 2.88\%$. On the other hand, since the discharge time for each glide is longer, the gas is treated for longer, which could be beneficial for our purposes.

The final objective was to characterize the produced discharge by collecting and examining electrical, thermal, and flow data. Using a voltage probe, current transformer, and an oscilloscope, the electrical data were collected. The voltage signal followed the inner electrode gap, allowing us to draw conclusions between the electrical data and certain points along the inner electrode edge. This phenomenon was used to test the hypothesis that the straight section of the electrode allows the reactor to maintain an NTP for a longer time. A more sinusoidal voltage signal was observed for the straight section of Design 3, as opposed to the two-peak signal characteristic of

thermal arcs in the divergent section of the discharge. The reduced electric field was also calculated for a run with N_2 gas at 2.5 SLPM and found to be in the optimum region for efficient dissociation of N_2 molecules through vibration excitation. Finally, the average power for all the runs with N_2 gas was between 38.43 W and 40.27 W.

The thermal data obtained in this study were for verifying the simulated data from the CFD analysis. The FLIR camera used (FLIR A500) in this study is unable to capture temperature distributions inside the reactor to examine the maximum temperature for the catalyst layer and ensure the required maximum temperature of 300 °C is achieved. Only the temperature profile of the top quartz plate was captured for the different runs after reaching steady state. The power input in the CFD simulation was then adjusted until the simulated temperature distribution of the top quartz plate matched the FLIR captured distributions. At that point, the temperature distribution of the simulated BNNT catalyst layer could be obtained. At the calculated free convection heat transfer coefficients, the BNNT catalyst sheet only reached a maximum temperature of around 125 °C. At half the coefficient values to simulate an insulated reactor, the maximum temperature only reached around 146.99 °C. Finally, with no heat transfer through convection, the temperature still fell short at 212.94 °C. The power input in the CFD software was then adjusted until the BNNT layer reached the desired temperature. It was found that an average power of around 51 W could be enough for the BNNT catalyst layer to reach 300 °C.

The CFD software was also used to examine the gas flow through the reactor. Examining the velocity vectors and streamlines for the different flow rates, vortices were observed on either side of the main flow down the center of the reactor. However, the magnitude of these vortices is not sufficient to have major effects on the operation

of the reactor. Stronger vortices could be induced through different means to help circulate reactive species in the reactor, increasing the residence time.

In conclusion, this thesis has successfully documented the design, optimization, and characterization of a PGD reactor for the purpose of gas conversion using NTPs. The electrical signals and thermal data collected provide valuable insights into the operation of the reactor. The CFD simulations conducted offer a deeper understanding of the temperature and flow dynamics within the reactor. The collected data and findings help expand and deepen our understanding of PGD reactors. Moreover, this study lays the foundation for future work aimed at improving the current PGD reactor design and exploring its potential in the production of zero-carbon and carbon-neutral fuels. By advancing the understanding of NTP-based gas conversion, this study contributes to the broader goal of electrifying heavy industrial processes and reducing their greenhouse gas emissions, thus supporting global efforts to combat climate change and energy transition efforts.

6.2 Future Works

Although electrode Design 3 successfully prolongs the treatment time and the NTP region, it reduces the total volume of gas treated. In the future, various methods can be used to mitigate this disadvantage. One method suggested earlier involves studying the effect of structures that induce vortices. This could be done quantitatively by using an FTIR or other means to analyze output gases for different products and calculating conversion rates and energy efficiencies. Another method is to use a constant or variable magnetic field applied to the discharge to alter the way it glides. For example, a magnetic field applied perpendicularly to the direction of the flow

could either slow down or speed up the discharge. Interestingly, with an alternating current, the force exerted by the magnetic field on the discharge is constantly changing direction, switching back and forth, forcing the discharge to essentially wiggle. This, in theory, can allow the discharge to treat a larger volume of gas while still remaining in the NTP region.

Another future direction would be to work on the scalability of the reactor. This could be achieved by using a larger, more powerful reactor. However, there is a limitation on the size of PGD reactors. Another way to achieve larger-scale production would be to number up and use multiple systems in series. This approach would allow more freedom in the production magnitude per the required application. Moreover, having multiple smaller systems in series would enable a facility to run at lower capacities depending on the amount of excess energy available.

References

[1] K. Ollegott, P. Wirth, C. Oberste-Beulmann, P. Awakowicz, and M. Muhler, "Fundamental properties and applications of dielectric barrier discharges in plasma-catalytic processes at atmospheric pressure," *Chemie Ingenieur Technik*, vol. 92, no. 10, pp. 1542–1558, 2020. DOI: 10.1002/cite.202000075.

[2] D. Nagassou, S. Mohsenian, S. Bhatta, R. Elahi, and J. P. Trelles, "Solar–gliding arc plasma reactor for carbon dioxide decomposition: Design and characterization," *Solar Energy*, vol. 180, no. October 2018, pp. 678–689, 2019, ISSN: 0038092X. DOI: 10.1016/j.solener.2019.01.070. [Online]. Available: https://doi.org/10.1016/j.solener.2019.01.070.

[3] L. Babich and T. V. Loĭko, "Generalized paschen's law for overvoltage conditions," *IEEE Transactions on Plasma Science*, vol. 44, no. 12, pp. 3243–3248, 2016. DOI: 10.1109/TPS.2016.2629022.

[4] A. Fridman, A. Gutsol, S. Gangoli, Y. Ju, and T. Ombrello, "Characteristics of gliding arc and its application in combustion enhancement," *Journal of Propulsion and Power*, vol. 24, no. 6, pp. 1216–1228, 2008, ISSN: 15333876. DOI: 10.2514/1.24795.

[5] C. Roth, "Nanoscale plasma surface modification of powders," Ph.D. dissertation, Jan. 2012. DOI: 10.3929/ethz-a-007618071.

[6] Maciej Serda, F. G. Becker, M. Cleary, *et al.*, "Synteza i aktywność biologiczna nowych analogów tiosemikarbazonowych chelatorów żelaza," *Uniwersytet ślaski*, vol. 7, no. 1, G. Balint, B. Antala, C. Carty, J.-M. A. Mabieme, I. B. Amar, and A. Kaplanova, Eds., pp. 343–354, 2013, ISSN: 1868-7075. DOI: 10.2/JQUERY.MIN.JS. arXiv: arXiv:1011.1669v3. [Online]. Available: https://desytamara.blogspot.com/2017/11/sistem-pelayanan-perpustakaan-

dan-jenis.html%20https://lambeturah.id/pengertian-website-secara-umum-dan-menurut-para-ahli/%20https://www.researchgate.net/publication/269107473_What_is_governance/link/548173090cf22525dcb.

[7] T. Nitsche, C. Unger, and E. Weidner, "Plasma Catalytical Reactors for Atmospheric Gas Conversions," *Chemie-Ingenieur-Technik*, vol. 90, no. 10, pp. 1453–1464, 2018, ISSN: 15222640. DOI: 10.1002/cite.201800024.

[8] J. C. Whitehead, "Plasma–catalysis: the known knowns, the known unknowns and the unknown unknowns," *Journal of Physics D: Applied Physics*, vol. 49, no. 24, p. 243 001, May 2016, ISSN: 0022-3727. DOI: 10.1088/0022-3727/49/24/243001. [Online]. Available: https://iopscience.iop.org/article/10.1088/0022-3727/49/24/243001%20https://iopscience.iop.org/article/10.1088/0022-3727/49/24/243001/meta.

[9] E. C. Neyts, K. Ostrikov, M. K. Sunkara, and A. Bogaerts, "Plasma Catalysis: Synergistic Effects at the Nanoscale," 2015. DOI: 10.1021/acs.chemrev.5b00362. [Online]. Available: https://pubs.acs.org/sharingguidelines.

[10] "Fundamental Properties and Applications of Dielectric Barrier Discharges in Plasma-Catalytic Processes at Atmospheric Pressure," *Chemie-Ingenieur-Technik*, vol. 92, no. 10, pp. 1542–1558, 2020, ISSN: 15222640.

[11] H. Zhang, F. Zhu, X. Tu, Z. Bo, K. Cen, and X. Li, "Characteristics of atmospheric pressure rotating gliding arc plasmas," *Plasma Science and Technology*, vol. 18, no. 5, pp. 473–477, 2016. DOI: 10.1088/1009-0630/18/5/05.

[12] X. Tu and J. C. Whitehead, "Plasma dry reforming of methane in an atmospheric pressure ac gliding arc discharge: Co-generation of syngas and carbon nanomaterials," *International Journal of Hydrogen Energy*, vol. 39, no. 18, pp. 9658–9669, 2014. DOI: 10.1016/j.ijhydene.2014.04.073.

[13] Z. A. Allah and J. C. Whitehead, "Plasma-catalytic dry reforming of methane in an atmospheric pressure ac gliding arc discharge," *Catalysis Today*, vol. 256, pp. 76–79, 2015. DOI: 10.1016/j.cattod.2015.03.040.

[14] S. Ghavam, M. Vahdati, I. A. Wilson, and P. Styring, "Sustainable Ammonia Production Processes," *Frontiers in Energy Research*, vol. 9, no. March, pp. 1–19, 2021, ISSN: 2296598X. DOI: 10.3389/fenrg.2021.580808.

[15] R. J. Pattabathula Venkat, "Introduction to Ammonia Production — AIChE," *CEP Magazine*, no. 2, pp. 69–75, 2016. [Online]. Available: https://www.aiche.org/resources/publications/cep/2016/september/introduction-ammonia-production.

[16] J. Humphreys, R. Lan, and S. Tao, "Development and Recent Progress on Ammonia Synthesis Catalysts for Haber–Bosch Process," *Advanced Energy and Sustainability Research*, vol. 2, no. 1, p. 2 000 043, 2021, ISSN: 2699-9412. DOI: 10.1002/aesr.202000043.

[17] F. Bird, A. Clarke, P. Davies, and E. Surkovic, *Ammonia : fuel and energy store*. 2020, pp. 1–40, ISBN: 9781782524489. [Online]. Available: https://royalsociety.org/-/media/policy/projects/green-ammonia/green-ammonia-policy-briefing.pdf.

[18] The Royal Society, *Ammonia : zero-carbon fertiliser, fuel and energy store. Policy Briefing.* 2020, p. 39, ISBN: 9781782524489. [Online]. Available: royalsociety.org/green-ammonia.

[19] A. Bogaerts, X. Tu, J. C. Whitehead, *et al.*, *The 2020 plasma catalysis roadmap*, 2020. DOI: 10.1088/1361-6463/ab9048. [Online]. Available: https://doi.org/10.1088/1361-6463/ab9048.

[20] S. Li, J. Jimenez, V. Hessel, and F. Gallucci, "Recent progress of plasma-assisted nitrogen fixation research: A review," *Processes*, vol. 6, p. 248, Dec. 2018. DOI: 10.3390/pr6120248.

[21] *Climate Change - REACT*. [Online]. Available: https://www.re-act.org.uk/climate-change/?gad_source=1&gclid=EAIaIQobChMI9qy6pfrOhAMVEevjBx3kfgkiEAAYAyAAEgL8_D_BwE (visited on 02/28/2024).

[22] B. Wang, X. Li, X. Wang, and B. Zhang, "Effect of filling materials on CO2 conversion with a dielectric barrier discharge reactor," *Journal of Environmental Chemical Engineering*, vol. 9, no. 6, p. 106 370, Dec. 2021, ISSN: 2213-3437. DOI: 10.1016/J.JECE.2021.106370.

[23] R. S. Abiev, D. A. Sladkovskiy, K. V. Semikin, D. Y. Murzin, and E. V. Rebrov, "Non-thermal plasma for process and energy intensification in dry reforming of methane," *Catalysts*, vol. 10, no. 11, pp. 1–41, 2020, ISSN: 20734344. DOI: 10.3390/catal10111358.

[24] R. Jaffe, "Vibrational and Rotational Excitation and Dissociation of CO2 Reexamined," American Institute of Aeronautics and Astronautics (AIAA), Jan. 2011. DOI: 10.2514/6.2011-447. [Online]. Available: https://www.researchgate.net/publication/268565407_Vibrational_and_Rotational_Excitation_and_Dissociation_of_CO2_Reexamined.

[25] VacCoat, *Glow Discharge Plasma Cleaning And Applications — 8 Vac Coat Plasma Cleaners*. [Online]. Available: https://vaccoat.com/blog/glow-discharge-plasma-cleaning/ (visited on 02/29/2024).

[26] Plasma Universe, *Electric glow discharge — Plasma-Universe.com*. [Online]. Available: https://www.plasma-universe.com/electric-glow-discharge/ (visited on 02/29/2024).

[27] G. Trenchev, A. Nikiforov, W. Wang, S. Kolev, and A. Bogaerts, "Atmospheric pressure glow discharge for CO2 conversion: Model-based exploration of the optimum reactor configuration," *Chemical Engineering Journal*, vol. 362, pp. 830–841, Apr. 2019, ISSN: 13858947. DOI: 10.1016/j.cej.2019.01.091.

[28] D. Staack, B. Farouk, A. Gutsol, and A. Fridman, "Characterization of a dc atmospheric pressure normal glow discharge," *Plasma Sources Sci. Technol*, vol. 14, pp. 700–711, Nov. 2005. DOI: 10.1088/0963-0252/14/4/009.

[29] J. Y. Wang, G. G. Xia, A. Huang, S. L. Suib, Y. Hayashi, and H. Matsumoto, "CO2 Decomposition Using Glow Discharge Plasmas," *Journal of Catalysis*, vol. 185, no. 1, pp. 152–159, Jul. 1999, ISSN: 0021-9517. DOI: 10.1006/JCAT.1999.2499.

[30] M. L. Carreon, "Plasma catalytic ammonia synthesis: State of the art and future directions," vol. 52, no. 48, 2019. DOI: 10.1088/1361-6463/ab3b2c.

[31] M. Touvelle, J. L. Licea, and M. Venugopalan, "Plasma chemical synthesis. II. Effect of wall surface on the synthesis of ammonia," *Plasma Chemistry and Plasma Processing*, vol. 7, no. 1, pp. 101–108, Mar. 1987, ISSN: 02724324. DOI: 10.1007/BF01016001/METRICS. [Online]. Available: https://link.springer.com/article/10.1007/BF01016001.

[32] K. S. Yin and M. Venugopalan, "Plasma chemical synthesis. I. Effect of electrode material on the synthesis of ammonia," *Plasma Chemistry and Plasma Processing*, vol. 3, no. 3, pp. 343–350, Sep. 1983, ISSN: 02724324. DOI: 10.1007/BF00564632/METRICS. [Online]. Available: https://link.springer.com/article/10.1007/BF00564632.

[33] R. Spielman, A. Hill, and S. Wilson, *Apparatus for highly efficient cold-plasma ozone production*, Nov. 2013. [Online]. Available: https://patents.google.com/patent/US9067788B1/en.

[34] Relyon Plasma, *Dielectric barrier discharge · for plasma generation.* [Online]. Available: https://www.relyon-plasma.com/glossary/dielectric-barrier-discharge/?lang=en (visited on 03/28/2024).

[35] B. Wang, X. Li, X. Wang, and B. Zhang, "Effect of filling materials on CO2 conversion with a dielectric barrier discharge reactor," *Journal of Environmental Chemical Engineering*, vol. 9, no. 6, p. 106 370, Dec. 2021, ISSN: 2213-3437. DOI: 10.1016/J.JECE.2021.106370.

[36] T. Wang, H. Liu, X. Xiong, and X. Feng, "Conversion of carbon dioxide to carbon monoxide by pulse dielectric barrier discharge plasma," *IOP Conference Series: Earth and Environmental Science*, vol. 52, no. 1, p. 012 100, Jan. 2017, ISSN: 1755-1315. DOI: 10.1088/1742-6596/52/1/012100. [Online]. Available: https://iopscience.iop.org/article/10.1088/1742-6596/52/1/012100%20https://iopscience.iop.org/article/10.1088/1742-6596/52/1/012100/meta.

[37] S. Paulussen, B. Verheyde, X. Tu, *et al.*, "Conversion of carbon dioxide to value-added chemicals in atmospheric pressure dielectric barrier discharges," *Plasma Sources Science and Technology*, vol. 19, no. 3, p. 034 015, May 2010, ISSN: 0963-0252. DOI: 10.1088/0963-0252/19/3/034015. [Online]. Available: https://iopscience.iop.org/article/10.1088/0963-0252/19/3/034015%20https://iopscience.iop.org/article/10.1088/0963-0252/19/3/034015/meta.

[38] J. A. Andersen, M. C. Holm, K. van 't Veer, *et al.*, "Plasma-catalytic ammonia synthesis in a dielectric barrier discharge reactor: A combined experimental study and kinetic modeling," *Chemical Engineering Journal*, vol. 457, p. 141 294, Feb. 2023, ISSN: 1385-8947. DOI: 10.1016/J.CEJ.2023.141294.

[39] M. Bai, X. Bai, Z. Zhang, and M. Bai, "Synthesis of ammonia in a strong electric field discharge at ambient pressure," *Plasma Chemistry and Plasma Processing*, vol. 20, no. 4, pp. 511–520, 2000, ISSN: 02724324. DOI: 10.1023/A:1007031906589/METRICS. [Online]. Available: https://link.springer.com/article/10.1023/A:1007031906589.

[40] H. H. Kim, Y. Teramoto, A. Ogata, H. Takagi, and T. Nanba, "Atmospheric-pressure non-thermal plasma synthesis of ammonia over ruthenium catalysts," *Plasma Processes and Polymers*, vol. 14, no. 6, p. 1 600 157, Jun. 2017, ISSN: 1612-8869. DOI: 10.1002/PPAP.201600157. [Online]. Available: https://onlinelibrary.wiley.com/doi/full/10.1002/ppap.201600157%20https://onlinelibrary.wiley.com/doi/abs/10.1002/ppap.201600157%20https://onlinelibrary.wiley.com/doi/10.1002/ppap.201600157.

[41] F. A. D'Isa, E. A. Carbone, A. Hecimovic, and U. Fantz, "Performance analysis of a 2.45 GHz microwave plasma torch for CO2decomposition in gas swirl configuration," *Plasma Sources Science and Technology*, vol. 29, no. 10, p. 105 009, Oct. 2020, ISSN: 13616595. DOI: 10.1088/1361-6595/abaa84. arXiv: 1912.11414. [Online]. Available: https://iopscience.iop.org/article/10.1088/1361-6595/abaa84%20https://iopscience.iop.org/article/10.1088/1361-6595/abaa84/meta.

[42] T. Silva, N. Britun, T. Godfroid, and R. Snyders, "Optical characterization of a microwave pulsed discharge used for dissociation of CO2," *Plasma Sources Science and Technology*, vol. 23, no. 2, p. 025 009, Mar. 2014, ISSN: 0963-0252. DOI: 10.1088/0963-0252/23/2/025009. [Online]. Available: https://iopscience.iop.org/article/10.1088/0963-0252/23/2/025009%20https://iopscience.iop.org/article/10.1088/0963-0252/23/2/025009/meta.

[43] S. Paulussen, B. Verheyde, X. Tu, *et al.*, "Conversion of carbon dioxide to value-added chemicals in atmospheric pressure dielectric barrier discharges," *Plasma Sources Science and Technology*, vol. 19, no. 3, p. 034 015, May 2010, ISSN: 0963-0252. DOI: 10.1088/0963-0252/19/3/034015. [Online]. Available: https://iopscience.iop.org/article/10.1088/0963-0252/19/3/034015%20https://iopscience.iop.org/article/10.1088/0963-0252/19/3/034015/meta.

[44] G. Chen, N. Britun, T. Godfroid, V. Georgieva, R. Snyders, and M. P. Delplancke-Ogletree, "An overview of CO2 conversion in a microwave discharge: the role of plasma-catalysis," *Journal of Physics D: Applied Physics*, vol. 50, no. 8, p. 084 001, Jan. 2017, ISSN: 0022-3727. DOI: 10.1088/1361-6463/AA5616. [Online]. Available: https://iopscience.iop.org/

article/10.1088/1361-6463/aa5616%20https://iopscience.iop.org/article/10.1088/1361-6463/aa5616/meta.

[45] H. Uyama and O. Matsumoto, "Synthesis of ammonia in high-frequency discharges," *Plasma Chemistry and Plasma Processing*, vol. 9, no. 1, pp. 13–24, Mar. 1989, ISSN: 02724324. DOI: 10.1007/BF01015824/METRICS. [Online]. Available: https://link.springer.com/article/10.1007/BF01015824.

[46] UyamaHaruo, UchikuraTakeshi, NiijimaHideaki, and MatsumotoOsamu, "Synthesis of Ammonia with RF Discharge. Adsorption of Products on Zeolite," *https://doi.org/10.1246/cl.1987.555*, vol. 16, no. 4, pp. 555–558, Mar. 2006, ISSN: 0366-7022. DOI: 10.1246/CL.1987.555. [Online]. Available: https://www.journal.csj.jp/doi/10.1246/cl.1987.555.

[47] J. Shah, T. Wu, J. Lucero, M. A. Carreon, and M. L. Carreon, "Nonthermal Plasma Synthesis of Ammonia over Ni-MOF-74," *ACS Sustainable Chemistry and Engineering*, vol. 7, no. 1, pp. 377–383, Jan. 2019, ISSN: 21680485. DOI: 10.1021/ACSSUSCHEMENG.8B03705/SUPPL_FILE/SC8B03705_SI_001.PDF. [Online]. Available: https://pubs.acs.org/doi/abs/10.1021/acssuschemeng.8b03705.

[48] X. Bai, S. Tiwari, B. Robinson, C. Killmer, L. Li, and J. Hu, "Microwave catalytic synthesis of ammonia from methane and nitrogen," *Catalysis Science Technology*, vol. 8, no. 24, pp. 6302–6305, Dec. 2018, ISSN: 2044-4761. DOI: 10.1039/C8CY01355A. [Online]. Available: https://pubs.rsc.org/en/content/articlehtml/2018/cy/c8cy01355a%20https://pubs.rsc.org/en/content/articlelanding/2018/cy/c8cy01355a.

[49] B. Sudhakar Patil, "Plasma (Catalyst)-Assisted Nitrogen Fixation: Reactor Development for Nitric Oxide and Ammonia Production O N O O N," Ph.D. dissertation, Eindhoven University of Technology, 2017. [Online]. Available: https://pure.tue.nl/ws/files/64000562/20170510_Patil.pdf.

[50] K. Stanimir, B. Annemie-, S. Kolev, and A. Bogaerts, "Similarities and differences between gliding glow and gliding arc discharges," DOI: 10.1088/0963-0252/24/6/065023. [Online]. Available: http://dx.doi.org/doi:10.1088/0963-0252/24/6/065023.

[51] B. S. Patil, "Plasma (catalyst) - assisted nitrogen fixation: Reactor development for nitric oxide and ammonia production," PhD Thesis, Technische Universiteit Eindhoven, Eindhoven,

Netherlands, 2017. [Online]. Available: https://pure.tue.nl/ws/files/64000562/20170510_Patil.pdf.

[52] X. Tu and J. C. Whitehead, "Plasma dry reforming of methane in an atmospheric pressure AC gliding arc discharge: Co-generation of syngas and carbon nanomaterials," *International Journal of Hydrogen Energy*, vol. 39, no. 18, pp. 9658–9669, Jun. 2014, ISSN: 0360-3199. DOI: 10.1016/J.IJHYDENE.2014.04.073.

[53] H. Zhang, L. Li, R. Xu, *et al.*, "Plasma-enhanced catalytic activation of CO2 in a modified gliding arc reactor," *Waste Disposal and Sustainable Energy*, vol. 2, no. 2, pp. 139–150, 2020, ISSN: 25247891. DOI: 10.1007/s42768-020-00034-z.

[54] N. Notman, *Transition metal catalysts — Feature — RSC Education*. [Online]. Available: https://edu.rsc.org/feature/transition-metal-catalysts/4013803.article (visited on 06/06/2023).

[55] C. H. Lee, S. Bhandari, B. Tiwari, N. Yapici, D. Zhang, and Y. K. Yap, "Boron Nitride Nanotubes: Recent Advances in Their Synthesis, Functionalization, and Applications," *Molecules (Basel, Switzerland)*, vol. 21, no. 7, Jul. 2016, ISSN: 1420-3049. DOI: 10.3390/MOLECULES21070922. [Online]. Available: https://pubmed.ncbi.nlm.nih.gov/27428947/.

[56] S. Walker, G. Price, E. Pajootan, and S. Coulombe, "Viability of Boron Nitride Nanotubes as a Support Structure for Metal Nanoparticle Catalysts for the Plasma-Catalytic Synthesis of Ammonia," *2021 IEEE 16th Nanotechnology Materials and Devices Conference, NMDC 2021*, 2021. DOI: 10.1109/NMDC50713.2021.9677529.

[57] H. H. Kim, Y. Teramoto, A. Ogata, H. Takagi, and T. Nanba, "Atmospheric-pressure nonthermal plasma synthesis of ammonia over ruthenium catalysts," *Plasma Processes and Polymers*, vol. 14, no. 6, p. 1 600 157, Jun. 2017, ISSN: 1612-8869. DOI: 10.1002/PPAP.201600157. [Online]. Available: https://onlinelibrary.wiley.com/doi/full/10.1002/ppap.201600157%20https://onlinelibrary.wiley.com/doi/abs/10.1002/ppap.201600157%20https://onlinelibrary.wiley.com/doi/10.1002/ppap.201600157.

[58] K. S. Kim, M. B. Jakubinek, Y. Martinez-Rubi, *et al.*, "Polymer nanocomposites from free-standing, macroscopic boron nitride nanotube assemblies," *RSC Advances*, vol. 5, no. 51, pp. 41 186–41 192, May 2015, ISSN: 2046-2069. DOI: 10.1039/C5RA02988K. [Online]. Available:

https://pubs.rsc.org/en/content/articlehtml/2015/ra/c5ra02988k%20https://pubs.rsc.org/en/content/articlelanding/2015/ra/c5ra02988k.

[59] SIMSCALE, *Computational Fluid Dynamics (CFD) - Ultimate Guide — SimScale*. [Online]. Available: https://www.simscale.com/docs/simwiki/cfd-computational-fluid-dynamics/what-is-cfd-computational-fluid-dynamics/ (visited on 03/29/2024).

[60] Fastway Engineering, *Ansys Fluent Day 1, Intro*. [Online]. Available: https://fastwayengineering.com/student/ansys-fluent-overview/ansys-fluent-day-1-intro/ (visited on 03/29/2024).

[61] W. Wang, D. Mei, X. Tu, and A. Bogaerts, "Gliding arc plasma for CO 2 conversion: better insights by a combined experimental and modelling approach,"

[62] I. Technical Class Products, *Technical Glass Products: Properties of Fused Quartz*, 2022. [Online]. Available: https://technicalglass.com/technical-properties/%20https://technicalglass.com/technical_properties/ (visited on 04/04/2024).

[63] McMaster-Carr, *Low Profile C-Clamp*. [Online]. Available: https://www.mcmaster.com/products/clamps/clamps-1$%5Csim$/low-profile-c-clamps/ (visited on 09/13/2024).

[64] M. A. Lieberman and A. J. Lichtenberg, "Principles of Plasma Discharges and Materials Processing: Second Edition," *Principles of Plasma Discharges and Materials Processing: Second Edition*, pp. 1–757, Jan. 2005. DOI: 10.1002/0471724254. [Online]. Available: https://onlinelibrary.wiley.com/doi/book/10.1002/0471724254.

[65] Brooks Instruments, *5850E Series Thermal Mass Flow Controllers Meters*, 2023. [Online]. Available: https://www.brooksinstrument.com/en/products/mass-flow-controllers/thermal-elastomer-sealed/5850-e-i-series (visited on 09/13/2024).

[66] McMaster-Carr, *Three-Way C-Clamp*. [Online]. Available: https://www.mcmaster.com/products/clamps/clamps-1$%5Csim$/three-way-c-clamps/ (visited on 09/13/2024).

[67] *SDG1032X Arbitrary Waveform Generator — Siglent*. [Online]. Available: https://siglentna.com/product/sdg1032x/ (visited on 09/13/2024).

[68] W. Generator, "Waveform Generator SDG1000X Series,"

[69] *Trek 20/20C Series — Non-Inverting High Voltage Amplifier, Output Voltage 0 to ±20 kV DC or Peak AC — Advanced Energy*. [Online]. Available: https://www.advancedenergy.com/

en-us/products/high-voltage-amplifiers/systems-greater-than-5-kv/400w/trek-20-20c/ (visited on 09/13/2024).

[70] *MSO2012 Tektronix — Mouser*. [Online]. Available: https://www.mouser.com/ProductDetail/Tektronix/MSO2012?qs=HJSulGd0C6xNjvXGytyWqQ%3D%3D&srsltid=AfmBOorGKnk7H9iF6yDwf0W3mfOCMRdr8PFOIFPw (visited on 09/13/2024).

[71] *P6015A — Tektronix*. [Online]. Available: https://www.mouser.ca/ProductDetail/Tektronix/P6015A?qs=HJSulGd0C6wJK9z%252BZ6Zk0w%3D%3D&mgh=1&utm_id=17633666059&gad_source=1&gclid=CjwKCAjwxY-3BhAuEiwAu7Y6s6B5smQYgU3zUbpeDaWYHofRsltQq6j8GMu4mjKh3n9RirpJpXeeFhoBwE%20https://in.tek.com/high-voltage-probe-manual/p6015a (visited on 09/13/2024).

[72] *Pearson Electronics Model 411 Clamp On Current Monitors*. [Online]. Available: https://tmetrix.com/product/pearson-electronics-model-411-current-monitors/%20https://www.pearsonelectronics.com/products/wideband-current-monitors (visited on 09/13/2024).

[73] T. FLIR, *A400-A700 Science Kits*. [Online]. Available: https://www.flir.ca/products/a400-a700-science-kits/?vertical=rd+science&segment=solutions (visited on 09/07/2023).

[74] A. Flir, "Flir A6260 ™," pp. 0–1, [Online]. Available: https://flir.netx.net/file/asset/10276/original.

[75] Technical Glass Products, *Fused Quartz Transmittance Curves*. [Online]. Available: https://technicalglass.com/fused-quartz-transmission/ (visited on 09/07/2023).

[76] M. I. Boulos, P. L. Fauchais, and E. Pfender, "Basic Concepts of Plasma Generation," in *Handbook of Thermal Plasmas*, M. I. Boulos, P. L. Fauchais, and E. Pfender, Eds. Cham: Springer International Publishing, 2023, pp. 473–506, ISBN: 978-3-030-84936-8. DOI: 10.1007/978-3-030-84936-8_11. [Online]. Available: https://doi.org/10.1007/978-3-030-84936-8_11.

[77] *Properties of fused quartz*, https://technicalglass.com/technical-properties/, Accessed: Dec. 18, 2023.

[78] D. Manufacturing, "Material properties of teflon - polytetrafluoroethylene (ptfe)," *Dielectric Manufacturing*, Feb. 2019. [Online]. Available: https://dielectricmfg.com/resources/knowledge-base/teflon/.

[79] *Matweb - the online materials information resource*. [Online]. Available: https://www.matweb.com/search/DataSheet.aspx?MatGUID=4d14eac958e5401a8fd152e1261b6843&ckck=1.

[80] *Bnnt refined mat*. [Online]. Available: https://www.bnnt.com/nanotubes/mat.

[81] M. B. Jakubinek, Y. Martinez-Rubi, K. S. Kim, M. Daroszewska, and S. Walker, "Development and characterization of commercial boron nitride nanotube product forms," NRC Publications Canada, Tech. Rep., 2017, Accessed: Dec.18,2023. [Online]. Available: https://nrc-publications.canada.ca/eng/view/ft/?id=5d7c4bbd-4bfc-4d49-a308-90ebb9063024.

[82] H.E.Misak, J.L.Rutledge, E.D.Swenson, and S.Mall, "Thermal transport properties of dry spun carbon nanotube sheets," *Hindawi*, Mar. 2016. [Online]. Available: https://www.hindawi.com/journals/jnm/2016/9174085/.

Appendix A

FLIR Camera and Thermocouple Temperature Value Comparison

Table A.1: The FLIR camera temperature reading at point two compared to the thermocouple readings as the emissivity is iteratively adjusted. The percentage difference slowly decreases as the emissivity was adjusted.

Emissivity	FLIR [°C]	Thermocouple [°C]	Percentage Difference [%]
0.93	91.66	89.53	2.4
0.95	90.99	90.12	1.0
0.98	89.12	89.76	0.7

Table A.2: The FLIR camera temperature reading at point three compared to the thermocouple readings as the emissivity is iteratively adjusted. The percentage difference slowly decreases as the emissivity was adjusted.

Emissivity	FLIR [°C]	Thermocouple [°C]	Percentage Difference [%]
0.93	96.73	94.03	2.8
0.95	95.10	93.86	1.3
0.98	94.47	94.15	0.3